COMING TOGETHER: INDIVIDUALS AT DIFFERENT SCALES WORKING FOR A COMMON GOAL

A Dissertation
Presented to
The Academic Faculty

by

Andrea J. Welsh

In Partial Fulfillment
of the Requirements for the Degree
Doctor of Philosophy in the
School of Physics

Georgia Institute of Technology
December 2019

COMING TOGETHER:
INDIVIDUALS AT DIFFERENT SCALES
WORKING FOR A COMMON GOAL

Approved by:

Prof. Flavio H. Fenton, Advisor
School of Physics
Georgia Institute of Technology

Prof. Kurt Wiesenfeld
School of Physics
Georgia Institute of Technology

Prof. Michael Schatz
School of Physics
Georgia Institute of Technology

Prof. Peter Yunker
School of Physics
Georgia Institute of Technology

Prof. Timothy Atherton
Department of Physics and Astronomy
Tufts University

Date Approved: July 22, 2019

"Sing in me, Muse, and through me tell the story
of that [wo]man skilled in all ways of contending,
the wanderer, harried for years on end,
after [s]he plundered the stronghold
on the proud height of Troy.
She saw the townlands
and learned the minds of many distant men,
and weathered many bitter nights and days
in [her] deep heart at sea, while [s]he fought only
to save [her] life, to bring [her] shipmates home.
But not by will nor valor could [s]he save them,
for their own recklessness destroyed them all
children and fools, they killed and feasted on
the cattle of Lord Helios, the Sun,
and he who moves all day through the heaven
took from their eyes the dawn of their return..."

Homer, The Odyssey, Book 1

To all those who

Have lost the light leading them from the darkness

And felt like they couldn't continue:

Don't stop looking.

ACKNOWLEDGEMENTS

It takes a village to raise a Ph.D. and there are many people that I want to acknowledge specifically for their support during this process.

First and foremost, I would like to thank my advisor, Dr. Flavio Fenton, for his mentorship and support over the years. The choice to work with him when I first started in 2012 was likely one of my better decisions and I am not sure I would be defending my Ph.D. if I had not worked with you over these last seven years, especially due to your understanding and patience of external stressors that may have been affected my work or mental presence at times.

I would also like to thank my all my committee members, Dr. Kurt Wiesenfield, Dr. Mike Schatz, Dr. Peter Yunker, and Dr. Timothy Atherton. I wish I was confident enough to seek your advice, but I have valued all of your support and thoughts throughout the years, not matter how small it may have seemed. I truly felt conversations with all of you were thoughtful and improved me as a scientists, even if I never got to investigate further in some of the suggested directions. I also believe your feedback on this dissertation will be important and valuable.

I would like to give thanks to my CHAOS Lab office mates and friends, Dr. Claire Ji, Dr. Diana Chen, Conner Herndon, and Hector Velasco who have supported me both in and out of research over the years and the chaos that is our lab.

I would like to give gratitude to Dr. Abouzar Kaboudian and Elly Konjkav-Kaboudian for their help and support over the last four years, checking on me frequently and providing kind and supportive ears.

I want to give my appreciation to the various students who have worked with me during my Ph.D. and helped me learn how to be a better mentor: Casey Trimble, Krishma Singal, Madeline Lazar, Mary Elizabeth Lee, Zoha Naqawe, Michael Barnhill, Divya Velivela, Ellie Finch, and Sophia Wiesenfeld.

I would also like to give my deepest gratitude for the therapists and psychiatrists that worked with me during my time at grad school: first, Dr. Rome Lester who really opened up the world of therapy for me, laid a lot of the groundwork for my healing and growth, and helped me to really open up, especially during the first two years of the Ph.D. program; Dr. Eleanor McMahan for her individual work with me starting some of the deep work needed on long term issues; Lindsey Coltaine, LAMFT, who continued working with me through some core issues during one of the hardest points in my life; Dr. Kristin Weinschenk who started me on my path though anti-depressants and validated my experiences and pain; Dr. Shannon Croft, who took over as my psychiatrist and helped me through this last year in particular; and Dr. Andy Smith who has met with me on multiple occasions through out different parts of my PhD including these last few weeks. Also worthy of note are Dr. Krystal Mayers, Dr. Drew Alderman, and Adrian Kunemund, MS all who have helped me through group therapy with their valuable insight and support.

I would like to give my thanks to the director and coordinators of the Georgia Tech LGBTQIA Resource Center, Dr. Aby Parson and Camilla Brewster, both who gave a lot of time and effort to make campus a safe place for people like me to be myself and for making it so that I was more comfortable to be out.

There are many physics friends from online communities, some of which became in person friends, that I would like to thank for their support and encouragement throughout the years: Samantha Burtwistle, Nicole Replogle, Jay Brett, Dennis Foren, Tangerine Claribold, Kay Bros, Ryan Levy, Robin Bjorkquist, Brenda Knauber, Rachael Mansbach, Rachel Bennett, Tia Martineau, Josh Einstein, Adam Iaizzi, and Andrew McAllister to name a few.

I also want to give my appreciation to the women professors who have served as mentors over the years and have given their time to talk with me and offer me advice: Dr. Deirdre Shoemaker, Dr. Jennifer Curtis, Dr. Elisabetta Matsumoto, Dr. Kate

Fu, Dr. Jennifer Glass, Dr. Kim Cobb, and Dr. Karen Daniels.

There are also other graduate students in the Georgia Institute of Technology, School of Physics who worked through the degree with me, particularly Elaine Rhoades, Emily Alicea-Muñoz, Lorena Magaña-Zertuche Kimberly Short, and Jing Wang.

I am also lucky to have had a wonderful cohort of women physicists I graduated from Boston University with and who have all been supportive and caring as we have each pursued our next steps in physics over the last eight years: Dr. Chelsea Bartram, Dr. Elim Cheung, Julie Moreau, CMD, and Dr. Ashley Rubenstein.

Also, I must thank my closest friends, Tiffany Campbell, Jenifer Harris, Victoria Sheridan, and Latiqua Williams, who have supported me and reminded me that I could do it through out this whole process, even when I wasn't sure anymore.

I would like to give my greatest thanks to my spouse Mike Dimitriyev for many things, too numerous to list here. Of particular note, is your suggestion in 2010 to move in together so that we can put our combine our math and physics books, some of which were used as references in this dissertation. From the first week of freshman physics until now, and all of our future physics achievements, I know you will always be supporting me along the way.

Finally, I will like to thank Fermi and Millie, the best cats in the world, who slept next to me these last few weeks as I stayed up late working on this dissertation laying on every single page of this document at some point. All graduate school stress seems insignificant when there are cats purring on you.

Contents

List of Tables

List of Figures

SUMMARY

Coming Together:

Individuals at Different Scales

Working for A Common Goal Andrea J. Welsh Advisor: Dr. Flavio H. Fenton Patterns in biology, chemistry, physics and mathematics can occur from self-organization and the interaction of constituents. In this thesis defense, I will explore patterns in two very different systems: (i) chimera states in a biologically-relevant model of excitable tissue, namely a modified version of the FitzHugh-Nagumo model, and (ii) collective motion of living many-agent systems such as swarms of brine shrimp.

The FitzHugh-Nagumo model is a simple dynamical system that adequately describes many phenomena in excitable biological systems, such as firing neurons. The excitability is modeled via cubic terms added to the otherwise linear differential equations that describe the time evolution of two dependent variables that characterize the state of a cell. When many of these cells are then coupled in space, the model results in either a stable fixed point or a stable limit cycle which describes synchronized oscillating cells. However, chimera states in which stable fixed-point and limit-cycle regions coexist are not described within this model, even though they are observed in the heart and the brain. By adding a 5th order term in the membrane potential to this 3rd order system, we can recover chimeras, dependent on only initial conditions of the cells. Chimeras have previously been shown in systems with non-local coupling. Interestingly, however, they appear in this new system with purely local coupling. We study the dynamics of these chimeras in a few situations: in 1-dimensional cables and rings with two different simultaneous dynamics and in 2-dimensional grids representing tissues.

Switching gears, I then discuss the patterns that occur in swarming, a self-organization phenomenon exhibited in many biological systems such as flocks of bird and insect, schools of fish, and collections of bacteria. This sort of behavior emerges spontaneously, arising without any sort of centralized control or leadership. Many crustaceans such as brine shrimp produce swarms, in which individuals cluster together rather than spread out uniformly in their environment. The size and distribution of these swarms are governed by local interactions between individuals. We will discuss the three-dimensional patterns that can be observed in brine shrimp swarms, specifically of the Great Salt Lake strain of Artemia franciscana, at high concentration. These patterns can be easily observed with simple tabletop experiments. We experimentally test the effects of certain environmental conditions on the dynamics of the individuals and on the development of these swarms.

Chapter I

INTRODUCTION

There are many systems in biology that can be studied on the constituent level, but the interaction between constituents can give rise to a global organization or pattern. This is seen on the cellular level all the way up to the formation of galaxies. While many of the mechanism behind the development of this sort of organization are different, they can be studied using many of the same tools.

Of one area of research is the study of couple oscillator systems which can produce dynamics much richer than that of the individual oscillators. Coupled oscillator systems have been of particular interest during to their applications in nature and technology. Models involving coupled oscillators have been used to describe firing of neurons [1], cardiac cells activations [2, 3], Josephson junctions [4], Human circadian rhythm and sleep-wake cycles [5, 6], firefly flashing [7], individual walkers on the Millennium Bridge [8], and more [9]. Coupling adds a degree of complexity in the system as oscillators may become in phase or out of phase dependent on the type of coupling used. These coupled oscillators form a network where local interactions can have global properties, like those of synchronization, traveling waves, or even formation of patterns.

Synchronization, or the emergence of spontaneous order, occur in many systems where is desirable such as the desirable synchronized contractions of the heart or not desirable such as in the case of our brain which when synchronized can trigger epileptic seizures [10] or the London Millennium Footbridge where a positive feedback phenomena that occurs when large groups of people cross the bridge caused their steps to be synchronous and could harm the structure [11].

Many systems in nature exhibit the formation of patterns. Patterns can appear on the largest scale such as organization of galaxies [12] or sand dune ripples [13] to smaller scale such as the growth of snowflakes [14]. For patterns to develop, there must be driving force pushing a system out of equilibrium and a dissipation force attempting to restore the system in equilibrium [15].

Of particular interest are Turing patterns [16], complicated patterns like spots or stripes which can arise due to instability from a uniform state. In his seminal work, Turing studied the simplest reaction-diffusion system that can form such patterns which led to multiple insights. The first was that two interacting chemicals were needed for a pattern to form. The second was that diffusion, normally thought to be something that smooths out spatial variations, can act as a destabilizing mechanism that causes instability for patterns to form. These instabilities can occur at different wavelengths and provide structure to the system. However, also concluded was that for a chemical system, the diffusion coefficients of at least two reagents much differ substantial. This work led to the study and understand of many sorts of patterns that have been observed in nature.

Also of interest are how constitutes may move in space and coordinate themselves through interactions. This is seen in the field of active matter. Active matter describes particles which absorb energy from their surrounds or from a fuel tank in order to move. Examples of such systems are suspensions of swimming bacteria, active colloids, collections of cytroskeletal filaments, or collections of large organisms such as fish and birds. These systems are in non-equilibrium and can consist of a large complexity of dynamics. In these systems, interactions and packing of individuals can lead to coordinated motion. Overall structure can form from these interactions leading to the emergence of patterns.

This thesis discusses a few problems that can be described by these mechanism.

Chapter II

CHIMERA STATES IN A QUINTIC FITZHUGH-NAGUMO MODEL

She was of divine stock, not of men, in the fore part a lion, in the hinder a serpent, and in the midst a goat, breathing forth in terrible wise the might of blazing fire.

—Homer, The Iliad, Book 6, lines 180-185

[1]

2.1 Introduction: The FitzHugh-Nagumo Model

This first section reviews a two-variable model called the FitzHugh-Nagumo (FHN) model [17, 18] including some of the main dynamics that have been previously observed in a single cell [19] as well as in space via diffusive coupling of neighboring cells [18], and how coupling affects those dynamics. We present an extension to this model that includes a higher order correction term that we have added to the model. We discuss some of the new dynamics with the addition of this term in one and two dimensions and why this is interesting. Finally, we discuss some potential applications of our new model and open problems that can still be studied.

The original model was developed by Richard FitzHugh in 1961 while continuing the analysis of the Hodgkin-Huxley equations for nerve membrane and exploring this simplified model of spike generation in axons and nerve cells [17]. FitzHugh used the Bonhoeffer-van der Pol idea of a "relaxation oscillator," which captures the qualitative properties of a wide class of oscillators, to develop a model which displays stable state and threshold phenomena as well as stable limit cycle oscillations. As

[1] English Translation by A.T. Murray, Ph.D. in two volumes. Cambridge, MA., Harvard University Press; London, William Heinemann, Ltd. 1924.

opposed to the Hodgkin-Huxley model which uses four variables of state, this model only uses two variables of state and can be derived from the linear differential equation with a nonlinear damping coefficient $k = v^2 - 1$ [20]. This yields the following pair of differential equations

$$\begin{aligned} \dot{v} &= v - \frac{v^3}{3} - w + z \\ \dot{w} &= -\epsilon(bw - v - \delta), \end{aligned} \tag{1}$$

where v is the "activator" variable and w is the "inhibitor" variable, which is why the system is often called a "relaxation oscillator". The constants b and δ control the dynamics of the system, z is an external stimulus that is included to allow the study of perturbations, and ϵ is a constant separate the time scales of the two variables.

This model, known as the FitzHugh-Nagumo model after J. Nagumo *et al.* created the equivalent circuit of it and model the dynamics in space [18], has become a canonical model of pattern formation and has been used to explain phenomena in biological, chemical and physical systems. Particularly of interest to our research group which works in the area of cardiac dynamics is its ability to sustain re-entry, or spiral waves, meaning that an impulse can re-excite the heart after refractory which often leads to arrhythmias, in one [21, 22], two [23, 24], and three dimensions [25, 26]. While it has not been able to yield an accurate quantitative description of cardiac action potentials and many other properties found in cardiac tissue, there have been attempts [27] made to improve the model so that it is more realistic to cardiac dynamics.

The FHN model can produce a variety of complex patterns including (i) a uniform stationary instability in which a monotonically growing uniform mode leads to bistability of uniform states i.e. stripe patterns, (ii) a non-uniform stationary instability in which a monotonically growing non-uniform mode leads to stationary patterns, and (iii) a uniform oscillatory instability in which a uniform mode with oscillatory

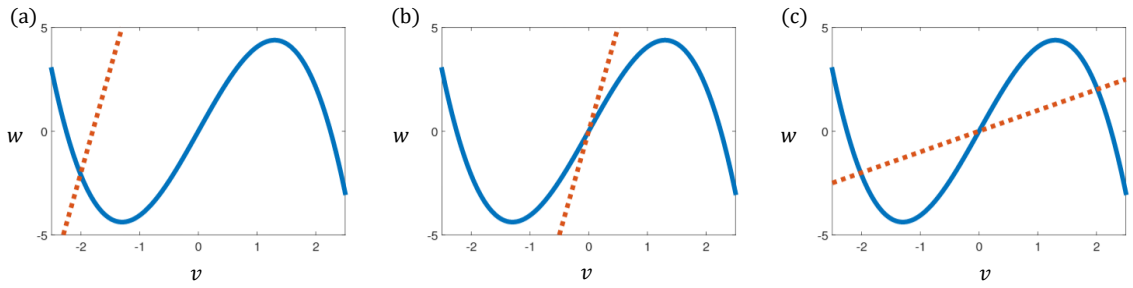

Figure 1: Three cases of nullcline intersection in the FHN model. Points of intersection represent stationary uniform states. a) Trajectories get attracted to the fixed point. b) Trajectories will be attracted to the cycle that oscillates. c) Trajectories are repelled away from the unstable fixed point at the origin and attract to one of the other two equilibria.

growth leads to long-wavelength traveling waves [19]. First, we discuss the different stationary uniform states that can exist and then we discuss the stability that can lead to producing such patterns.

To find the stationary uniform states, or fixed points, of a set of coupled differential equations, we can look at the intersections of the lines formed by setting $\dot{v} = 0$ and $\dot{w} = 0$. These lines are called the *nullclines* of the system and for Equation 1, there are two: a third order polynomial and a line. In the representation used here, the third order nullcline is symmetric about the origin. When shifting the linear nullcline about the horizontal axis, two different sets of dynamics can arise: (i) $|\delta| \geq 1$ leads to a stable fixed point at the intersection of the two oscillators on the outer branches of the cubic nullcline (Figure 1 a) or (ii) $|\delta| < 1$ leads to stable cycle and an unstable fixed point at the intersection of a single point on the middle branch of the cubic nullcline (Figure 1 b). Changing the slope of the linear nullcline, b, can cause the nullclines to intersect at three points leading to a Hopf bifurcation with two stable and an unstable fixed points if $b \leq 3/2$ (Figure 1 c) [15]. These dynamics are independent of ϵ, which affects the stability of these discussed in the next section.

The FHN model can be extended to 2-dimension space by coupling cells of Equation 1 diffusively. Particularly of interest is diffusive coupling in the v variable because

of the use of FHN to study cardiac dynamics where v represents the membrane potential of cardiac cells and w represents the current in individual ion channels, which are not coupled together. We now consider the FHN in 2D space as follows:

$$\dot{v} = v - \frac{v^3}{3} - w + z + D\nabla^2 v \tag{2}$$

$$\dot{w} = -\epsilon(bw - v - \delta) \tag{3}$$

Where ∇^2 is the Laplacian and D is a diffusion coefficient. In systems of coupled FHN oscillators, pulse solutions, multiple pulse solutions, periodic travel waves and spiral waves have been proven to exist [28]. We now look at the stability of these solutions.

2.1.1 Linear Stability Analysis

We consider the case in Figure 1 (b) (take $\delta = 0$) perform linear stability analysis, a method to observe the possible instabilities of the uniform state to non-uniform perturbations of that state. In order to do this, we consider first the zero solution given by $v_s = 0, w_s = 0$. For FHN, typically ϵ is the control parameter. Particularly, when $\epsilon > \epsilon_H = 1/d$, there exists a single stationary uniform state which is linearly stable. When $\epsilon = \epsilon_H = 1/d$, there exists a Hopf bifurcation to uniform oscillations.There is also another bifurcation to investigate: when $\epsilon = \epsilon_T = D_w/(2 - b + s\sqrt{1-b}$ which is the Turing bifurcation; however, for the purposes of this project, we take $D_w = 0$ so $\epsilon_T = 0$ We consider the stability of the zero solution to the growth of a Fourier mode k by starting with a new solution given as the zero solution + deviations which may grow as a function of k: $v(x,t) = v_s + \delta v(x,t)$ and $w(x,t) = w_s + \delta w(x,t)$. We define the following:

$$\begin{bmatrix} \delta v(x,t) \\ \delta w(x,t) \end{bmatrix} = \begin{bmatrix} \alpha_k(t) \\ \beta_k(t) \end{bmatrix} e^{ikx} + c.c. \tag{4}$$

Inserting into equation 2, and linearizing α_k and β_k yields the following system of ordinary differential equations:

$$\dot{\alpha_k} = (1 - k^2)\alpha_k - \beta_k \tag{5}$$

$$\dot{\beta_k} = \epsilon(\alpha_k - a_1\beta_k). \tag{6}$$

Looking for solutions of the form:

$$\begin{bmatrix} \alpha(t) \\ \beta(t) \end{bmatrix} = \begin{pmatrix} \alpha_k(t) \\ \beta_k(t) \end{pmatrix} e^{\sigma(k;e)t} \tag{7}$$

where $\sigma(k;t)$ is the growth rate of the perturbation along the k mode. Solving the eigenvalue problem which is given as follows:

$$\begin{pmatrix} 1 - k^2 & -1 \\ \epsilon & -\epsilon a_1 \end{pmatrix} \begin{pmatrix} \alpha_k \\ \beta_k \end{pmatrix} = \sigma \begin{pmatrix} \alpha_k \\ \beta_k \end{pmatrix} \tag{8}$$

leads to the characteristic equation:

$$\sigma^2 + (k^2 - 1 + \epsilon b)\sigma + \epsilon b(k^2 - 1) + \epsilon = 0 \tag{9}$$

which has solutions:

$$\sigma = \frac{1}{2}(1 - k^2 - \epsilon b) \pm \frac{1}{2}\sqrt{(1 - k^2 + \epsilon b)^2 - 4\epsilon} \tag{10}$$

which is complex when $(1 - k^2 + \epsilon b)^2 - 4\epsilon < 0$ or

$$\omega_0^2 = \epsilon - \frac{1}{4}(1 - k^2 + \epsilon b)^2 < 0 \tag{11}$$

where ω is the frequency of the growing modes. Looking at the real part of Equation

10, we can calculate the instability threshold and the critical mode that grows past this threshold value by the condition that the growth rate is zero $\sigma_R(k, \epsilon) = 0$. This gives the relationship:

$$\epsilon(k) = \frac{1 - k^2}{b} \tag{12}$$

whereas the change with respect to the wavenumber:

$$\frac{d\sigma_R}{dk} = 0 \tag{13}$$

which yields $k = 0$, the wavenumber of the critical mode which begins to grow at the instability point. These two conditions give the instabiltiy threshold $\epsilon_c = \frac{1}{b} = \epsilon_H$. If these are plugged into the equation for the frequency of the growing modes, Equation 11, yields $\omega_0^2 = \frac{1}{b} - 1 > 0$ which means that the first mode to grow as ϵ cross the critical point as the form:

$$\begin{bmatrix} \delta v \\ \delta w \end{bmatrix} = \begin{bmatrix} \alpha \\ \beta \end{bmatrix} e^{i\omega_0 t} + c.c. \tag{14}$$

$$= \begin{bmatrix} \alpha \\ \beta \end{bmatrix} e^{i\sqrt{\epsilon_c - 1}t} + c.c. \tag{15}$$

and is a uniform Hopf bifurcation where the growth of the first mode is uniform and the growth is oscillatory in time.

Deviations λ from the instability point can be considered of the form $\lambda = \frac{\epsilon_c - \epsilon}{\epsilon_c}$ which can change the growth rate to be $\sigma_R = \frac{1}{2}(\lambda - k^2)$. This means that any finite distance above $\lambda = 0$ leads to a band of long-wavelength modes that grow along side the uniform mode.

2.2 Chimeras

The previous section focused on some of the dynamics that can form through out the FHN system given different parameters to the set of equations. However, it has been observed in some systems [29, 30] that coupled oscillators can have different temporal dynamics coexisting in the same system even through the equations of each oscillator in the system are the identical leading to a combination of different patterns through out space. These sorts of spatio-temporal patterns, the coexistence of multiple types of dynamics, have been dubbed "chimeras."

In the area of coupled oscillators, the idea of a chimera state sprung into existence in 2002 from Kuramoto and Battogtokh [29]. Shortly after, the name was coined by Strogratz and Abrams [30] after the Greek Mythological beast whose earliest written evidence is credited to Homer's Iliad: a fire-breathing hybrid between lion's head, a goat's body, and a serpent's tail [31]. Just like this beast was created to be a plague for men, so too was this problem a plague for me, but unlike the men of mythology, my goal is not to defeat the chimera, but to subdue the beast and understand its behavior.

Abrams and Strogatz defined a chimera state as a spatio-temporal pattern in which a system of identical oscillators is split into coexisting regions of coherent (phase and frequency locked) and incoherent (drifting) oscillation, although later papers often adapt slightly different definitions. In their iconic paper [30], they use a version of the Kuramoto model, a model for phase coupling of oscillators, to show the existence of such states. To do this, they start with a ring of identical oscillators, oscillators which are described by the same exact differential equations including parameter set. These oscillators have a coupling network such that each oscillator is coupled to some radius of oscillators on either side of it. The governing equation of the system is given

as follows:

$$\frac{d\theta}{dt} = \omega - \int_{-\pi}^{\pi} G(x - x') \sin[\theta(x, t') - \theta(x, t) + \alpha] dx' \tag{16}$$

with θ is the oscillator phase, ω is the natural frequency, x is the position of the oscillator, α is a phase shift and $G(x)$ describes the coupling between oscillators where the strength of coupling decreases with distance between oscillator. This is given by:

$$G(x) = \frac{1}{2\pi}(1 + A \cos x) \tag{17}$$

where A is the coupling amplitude in the range of $[0, 1]$. Initial phases are given by a random distribution of:

$$\theta(x) = 6re^{-0.76x^2} \tag{18}$$

where r is a uniform variable on $[-\frac{1}{2}, \frac{1}{2}]$. This distribution yields oscillators which have small fluctuations from the oscillators near the boundaries making them closer to phase synchronizing while the other oscillators are random. This system begins near a chimera state and is left to integrate in time. The phases after a period of time are shown in Figure 2 which is taken from the Abrams & Strogatz paper. What we observe is that the oscillators have separated into two groups of phases: those coherent with phase $\theta \sim 0$ and those that are decoherent from $[-\pi, \pi]$. The local order parameters $R(x, t)$ which describes the local phase coherence and $\Theta(x, t)$ which describes the local average phases are calculated as follows:

$$R(x, t)e^{i\Theta(x,t)} = \int_{-\pi}^{\pi} G(x - x')e^{i\theta(x',t)} dx', \tag{19}$$

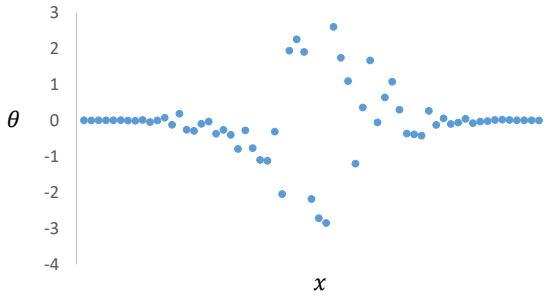

Figure 2: A plots reproduced from Abrams & Strogratz 2004 [30]. The phases of oscillators plotted in space x with periodic boundary conditions.

are also shown in Figure 2 (b,c) and show that the oscillators have a coherence close to 1 (max coherence) in the area where the phases are near $\theta = 0$ and that R drops significantly for those oscillators that are in the incoherence part of the chimera.

This work also began classifying a few types of chimeras that were found in this model such as those that are stable and those that are unstable. They found this is dependant on the amplitude A of the random initial conditions and the parameter $\beta = \pi/2 - \alpha$, a function of the coupling delay, α. Following this, many other systems were studied, including the FHN model discussed above, and these models were studied in a variety of coupling topologies. A non-exhaustive list of the types of topologies that have been studied so far include:

1. A ring of oscillators with non-local coupling [29, 30, 32–35]
2. A two-dimensional array of oscillators with non-local coupling [36] and tori [37]
3. A two-dimensional sphere of oscillators [38]
4. An all-to-all coupled network with inhomogeneous coupling strengths [39]
5. Two distinct subnetworks of oscillators with all-to-all coupling within and between the sub-networks [35, 40]
6. Erdos-Renyi and scale free networks [41]

7. Bipartite networks [42]

In particular, we are interested in the first two cases in terms of the topology of how the oscillators are connected. Therefore, we do not consider (3-6) and just focus on the chimera research that has been conducted on topologies with non-local coupling in a ring and 2D array of oscillators; however, it is important to note that at this time, nonlocality of some sort is thought to have been needed for chimeras to form, and often it is even included in the definition of chimera. Before tackling this last thought, I would like to discuss some of the work that has been done on chimeras for the FHN model.

2.2.1 Chimeras in other FHN Systems

With the rise in interest of Chimera states [29, 30], the FHN model has been studied in a variety of cases. First we discuss some of the work that has been done already, particularly in 1D rings and 2D arrays of oscillators before explaining how our new work is different.

In 2013, Omel'chenko *et al.* [43] first looked at rings of nonlocally coupled FHN oscillators where both the activator and inhibitor oscillators were coupled with themselves and with each other:

$$\begin{aligned} \epsilon \dot{u}_k &= u_k - \frac{u_k^3}{3} - v_k + \frac{\sigma}{2R} \sum_{j=k-R}^{k+R} [b_{uu}(u_j - u_k) + b_{uv}(v_j - v_k)] \\ \dot{v}_k &= u_k + a_k + \frac{\sigma}{2R} \sum_{j=k-R}^{k+R} [b_{vu}(u_j - u_k) + b_{vv}(v_j - v_k)] \end{aligned} \tag{20}$$

where R is given as the radius of coupling b_{lm} and θ are the coupling strengths and a_k is a fixed parameter that determines whether oscillator k is oscillatory or excitable.

For different ranges of parameters, they found chimera states with a section of coherence and a section of incoherence, like those of other models studied. This can be seen in [43] in the red plots, which show the phases of a ring of oscillators, and the

black plots, which show the mean phase velocities of the oscillators. Also, they found parameters where there were multiple sections of coherence splitting up sections of incoherence. Here they coined the term "multi-chimera states," which differentiates from previously observed chimeras because there are multiple regions of coherence an decoherence. The particular number of regimes of incoherence depended on the choice of radius of coupling R and coupling strength σ used in their simulations. In their study, the non-local, off diagonal coupling between the two variables was a crucial part of the occurrence of these chimera states observed.

Another example of chimeras in the FHN model is from work by Guo et al. [44] where the FHN oscillators are expanded to a 2D system. The equations are those in Equation 20 but now the topology is of a grid lattice of system size $N \times N$. Their simulations resulted in spiral wave chimeras of three types: (i) outwardly propagating spiral waves chimeras with incoherent core, (ii) inwardly propagating spiral wave chimeras with incoherent core, and (iii) a spiral wave chimera with an anti phase spot. Again of note is that this coupling matrix, which is compared to the "phase frustration" parameter in the Kuramoto system, is a "crucial quantity for the occurrence of chimeras."

2.3 Extension of the FHN Model

Expanding the FHN model, we propose a system that can have chimeras while only having nearest neighbor coupling via diffusion, which is unlike the studies discussed previously. We show that the collective motion of the identical oscillators in this new system can be classified into four situations: i) phase synchronized periodic oscillators, ii) the resting state with all fixed oscillators, iii) traveling waves with varying amplitudes, and iv) spatial-temporal patterns where oscillators exist in both oscillatory and fixed states, which are seen in 1D and 2D spatial systems.

2.3.1 Fifth Order Nullcline

We propose the extension, which we dub "FHN5" to differentiate from the original model, referred to going forward as "FHN3" as follows:

$$\begin{aligned} \dot{v} =& - v(v^2 - x_1^2)(v^2 - x_2^2) - w + D\nabla^2 v \\ \dot{w} =& \epsilon(v - dw - \delta). \end{aligned} \tag{21}$$

where the nullcline of v is a quintic polynomial (Figure 3). We use a quintic model to maintain long-term dynamics for w as v approaches $\pm\infty$. While there are a few ways of doing this (multiplying by $\dot{v}^2$, $v\ddot{v}$, v^{2n}, etc.) this is the most convenient and straight forward. With this change, FHN5 has two *basins of attraction*, or the set of initial conditions where oscillators evolve to a particular attractor as time goes to infinity: (i) a fixed equilibrium point and (ii) an attractive cycle.

2.3.2 Linear Stability Analysis

Similar to the FHN3, we can perform linear stability analysis on FHN5. First, we consider again the zero solution $v_s = 0, w_s = 0$, which is also a solution of FHN5. As before, we consider a perturbation about the zero solution and arrive at the following system of ODEs

$$\dot{\alpha_k} = -(x_1^2 x_2^2 + Dk^2)\alpha_k - \beta_k \tag{22}$$

$$\dot{\beta_k} = \epsilon(\alpha_k - d\beta_k) \tag{23}$$

with solutions of the form of Equation 7 again. Of note, the entire coefficient of α_k is negative, which is unlike the case for FHN3. This is due to keeping the leading power of FHN5 negative so that we have the form $-v^5 + Av^3 - Bv$ compared to FHN3 where

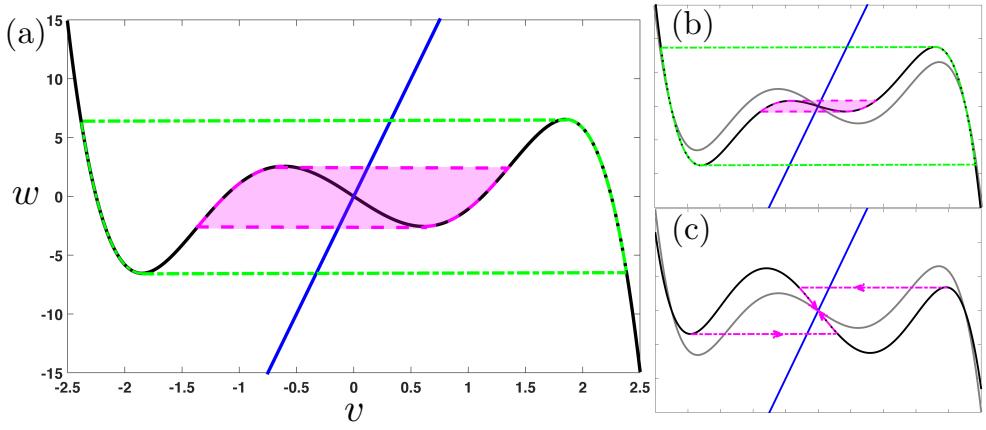

Figure 3: The nullclines for FHN5 are plotted. a) The v nullcline for $x_1 = 1.25$ shown by the black solid line as a quintic polynomial. The w nullcline is given by the solid straight line (blue). The dashed "–" line (magenta) shows the boundary of the two basins of attraction. The dashed-dotted line "-·" (green) shows the attractive cycle. b) Nullclines for $x_1 = 0.75$. Colors and symbols are the same as (a) but the nullcline with $x_1 = 1.25$ is shown lighter (gray). c). Nullclines for $x_1 = 1.55$. The nullcline with $x_1 = 1.25$ is shown lighter (gray). The dashed "–" line (magenta) shows the trajectory of two oscillators who originally start on the outer branch of the nullcline, but the inner relative extrema block the path and all trajectories get attracted to the stable fixed point at $(0, 0)$.

we have $-v^3 + Bv$. The eigenvalue problem is now as follows:

$$\begin{pmatrix} -(x_1^2 x_2^2 + Dk^2) & -1 \\ \epsilon & -\epsilon d \end{pmatrix} \begin{pmatrix} \alpha_k \\ \beta_k \end{pmatrix} = \sigma \begin{pmatrix} \alpha_k \\ \beta_k \end{pmatrix} \tag{24}$$

The characteristic equation is then

$$\sigma^2 + \Big(x_1^2 x_1^2 + Dk^2 + \epsilon d\Big)\sigma + \epsilon d\Big(\big(x_1^2 x_2^2\big)^2 + Dk^2\Big) = 0 \tag{25}$$

which gives us the solution of

$$\sigma_\pm = -\frac{1}{2}\Big(x_1^2 x_2^2 + Dk^2 + \epsilon d\Big) \pm \frac{1}{2}\sqrt{\Big(x_1^2 x_1^2 + Dk^2 - \epsilon d\Big)^2 - 4\epsilon} \tag{26}$$

This can be complex (see Appendix A) when $\Big(x_1^2x_2^2 + Dk^2 - \epsilon d\Big)^2 < 4\epsilon$ and therefore we can define the frequency of the oscillations to the stability as $\omega_0^2 = \epsilon - \frac{1}{4}\Big(x_1^2x_2^2 + Dk^2 - \epsilon d\Big)^2 > 0$. The real part of σ determines possible instability about the of the zero solution.

By setting $\mathrm{Re}(\sigma(k;\epsilon)) = 0$, we arrive at

$$\epsilon(k) = -(x_1^2x_2^2 + Dk^2)/d \tag{27}$$

and since ϵ is strictly positive, this means that the $\mathrm{Re}(\sigma)$ cannot be zero. Also, since $\Big(x_1^2x_2^2 + Dk^2 + \epsilon d\Big)$ is positive definite, $\mathrm{Re}(\sigma)$ is strictly negative. This means that the zero solution is a spiral sink. Further, we can conclude that the $\mathrm{Re}(\sigma) < 0$ for all parameter values and wavenumbers and the frequency of oscillations is given by ω_0. Figure 4 shows how the $\sigma_\pm$ decay with wavenumber for a variety of diffusion constants D. We see that for low wavenumber, oscillators for one eigenvalue grow (orange dashed line), while oscillators for the other eigenvalue decay. Also, the real parts for both eigenvalues decay. For some critical wavenumber k_c which depends on D, $\sigma_\pm$ becomes real-valued, but negative with different values for σ_+ and σ_-. This means, for $k > k_c(D)$, perturbations are uniformly stable.

What also can be seen is the affects of the relative basin size on these eigenvalues. Included in Figure 5 is the effects of the relative basin size on the eigenvalues for a fixed diffusion. (Plots of eigenvalue vs wavenumber for all pairs of (r_b, D) can be seen in Appendix A). There is a point where the imaginary parts of $\sigma_\pm$ disappear and $\sigma_\pm$ becomes strictly real. This occurs between $0.48 < r_b < 0.54$.

2.3.3 Dynamics in 1D rings

Now, we look at the long term dynamics for simulations of oscillators described by this model.

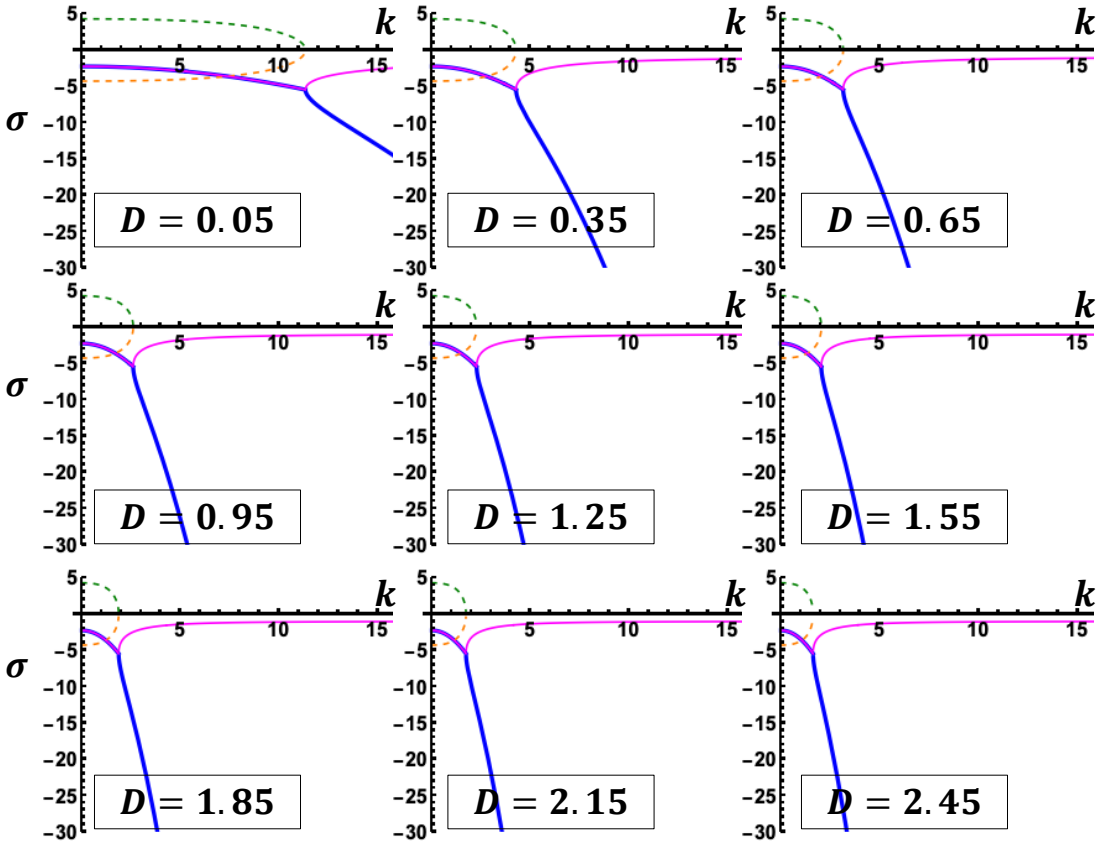

Figure 4: Plots of $\sigma_{\pm}$ vs k for different diffusion $D = 0.05, 0.35, 0.65, 0.95, 1.25, 1.55, 1.85, 2.15, 2.45$ values. The solid lines are the real part of $\mathrm{Re}(\sigma)$ and the dashed lines are $\mathrm{Im}(\sigma)$. Relative basin size is fixed $r_b = 0.3$

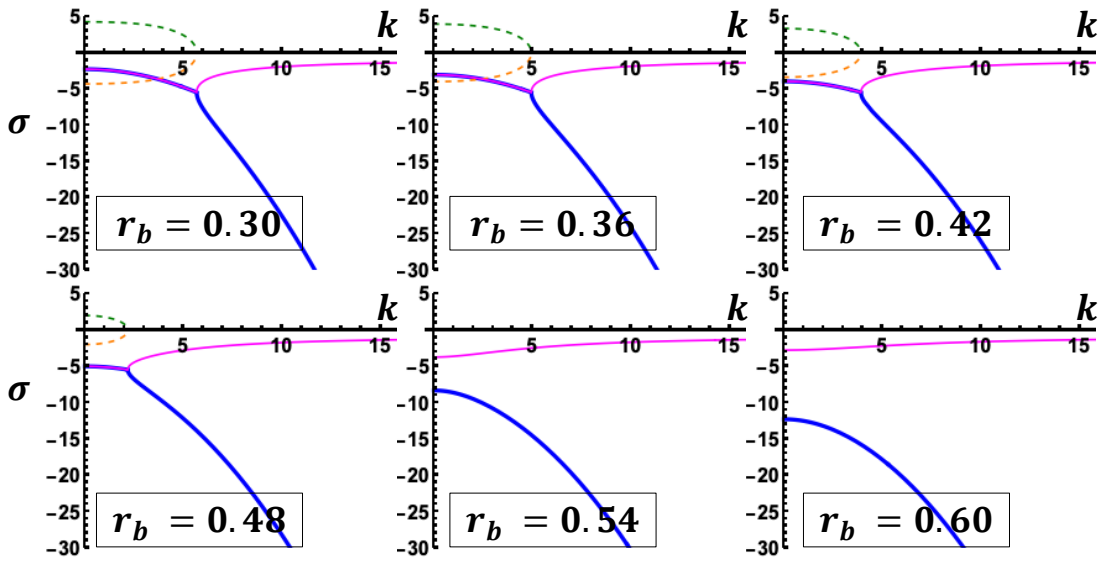

Figure 5: Effects of relative basin size r_b on $\sigma_{\pm}$ vs k plots. $D = 0.20$. $r_b = 0.30$, 0.36, 0.42, 0.48, 0.54, and 0.57. The solid lines are the real part of Re(σ) and the dashed lines are Im(σ).

For the purpose of these simulations, we use Euler integration with a finite difference method for the Laplacian with integration values $dt = 0.00625$ and $dx = 1$ that give convergent results [45]. For the parameters, $\delta = 0$ and $d = 0.05$. We also consider two cases of ϵ, one $\epsilon = 0.01$ and one $\epsilon = 1/d$. The diffusion D is varied $(0, 3]$, $x_2 = 2.5$ is fixed, and x_1 is varied $\in [0.75, 1.55]$. This is so that the relative size of the basin of attraction is changed as show in Figure 3. The relative basin length is defined as $r_b = x_1/x_2$.

The size of the ring is $N = 200$ identical oscillators which are coupled diffusively with nearest neighbor coupling and a periodic boundary. Each oscillator has initial conditions sampled randomly from $v_i \in [-2.5, 2.5]$ and $w_i \in [-12, 12]$ and run sufficiently long so that transient effects are ignored. Each parameter set is run for multiple initial conditions and the results are averaged such that the standard error is small relative to the average. We use a global order parameter which is defined as the percentage of fixed point cells labeled $\phi \in [0, 1]$ where $\phi = 0$ means all oscillators of the system are oscillating in the attractive cycle and $\phi = 1$ means all oscillators are

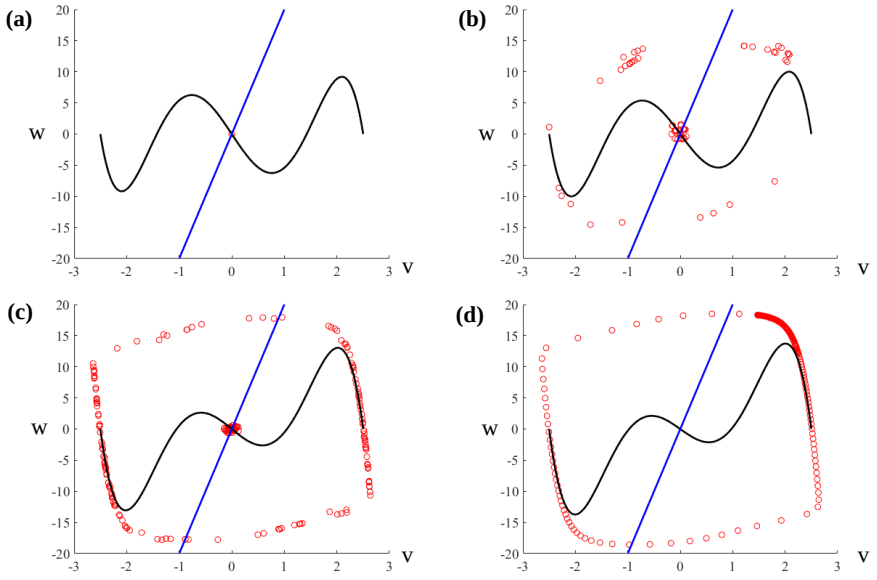

Figure 6: Snapshot of (v_k, w_k) for all oscillators in phase space at $t = 500$. (a) $(r_b, D) = (0.57, 0.95)$ where all oscillators are at the fixed point. (b) $(r_b, D) = (0.54, 0.85)$ where 150 oscillators are at the fixed point and 50 are oscillating. (c) $(r_b, D) = (0.42, 0.20)$ where 50 oscillators are at the fixed point and 150 are oscillating. (d) $(r_b, D) = (0.39, 2.65)$ where oscillators are making propagating waves.

at the fixed point attractor shown as the intersection of the two nullclines in Figure 3. We run these simulations for a range of diffusion $D \in [0, 3]$ and relative basin size $r_b \in [0.30, 0.62]$ where complex dynamics occur.

As expected, there are dynamics where all oscillators will be attracted to the fixed point solution, which can be seen in Figure 6 (a). When this happens, the oscillators will remain at the fixed point once attracted there. By plotting the oscillators value in time as shown in Figure 7 (a), we observe this can happen quickly ($t < 1$) and the dynamics are a steady state. Also as expected, there are steady state dynamics where all the oscillators will be attracted to the outer basin and remain in this cycle. Figure 6 (d) shows a snapshot of a case where this happens. Also looking at the phases of the oscillators in time, Figure 7 (d) shows that, for this case, waves are propagating through our system. This is also a steady state case.

Of particular interest, there exists a region where some oscillators will travel to

the fixed point attractor and others will travel to the cycle attractor. Plotting $v(x,t)$ for these states shows a spatio-temporal pattern of two different dynamics for large time periods, which we call the chimera state. This can be seen in Figure 6 (b, c) which show the phases of the oscillators in (v,w) space and in Figure 7 (b, c) which shows spaces vs time plots for two different sets of parameters where oscillators will split into "islands" of fixed points and "islands" of oscillations. For nearest-neighbor coupling, this simultaneous dynamics has not been observed in FHN3.

We also calculate the mean phase velocities of each oscillator defined as $\omega = 2\pi M_i/\Delta T, i = 1, ..., N$ [43] for each of the four dynamical cases and we find that:

- Case (a): All oscillators approach a mean phase of $\omega = 0$ when attracted to the fixed point.

- Case (b): Some oscillators attract to the fixed point still approach $\omega = 0$ while oscillators that are in the attractive cycle approach a constant $\omega = \omega_c$. There are also oscillators with mean phase velocity $\omega = \omega_b > \omega_c$ which are at the boundaries of the oscillating islands.

- Case (c): Most oscillators attract to the fixed point and approach $\omega = 0$ while there are a few oscillators that are in the attractive cycle approach a constant $\omega = \omega_c$. There are also oscillators with mean phase velocity $\omega = \omega_b > \omega_c$ which are at the boundaries of the oscillating islands.

- Case (d): All oscillators approach a mean phase velocity of $\omega = \omega'$. This does not differentiate between traveling waves or phase coherent oscillations.

Alternans [46] is a phenomena of oscillating pulse width in a plane wave that has been seen experimentally in cardiac systems [47–50], and has been characterized as a precursor for fibrillation. This is a type of instability that comes from a bifurcation [47]. Cytrynbaum and Keener showed that alternans are typically absent from FHN3

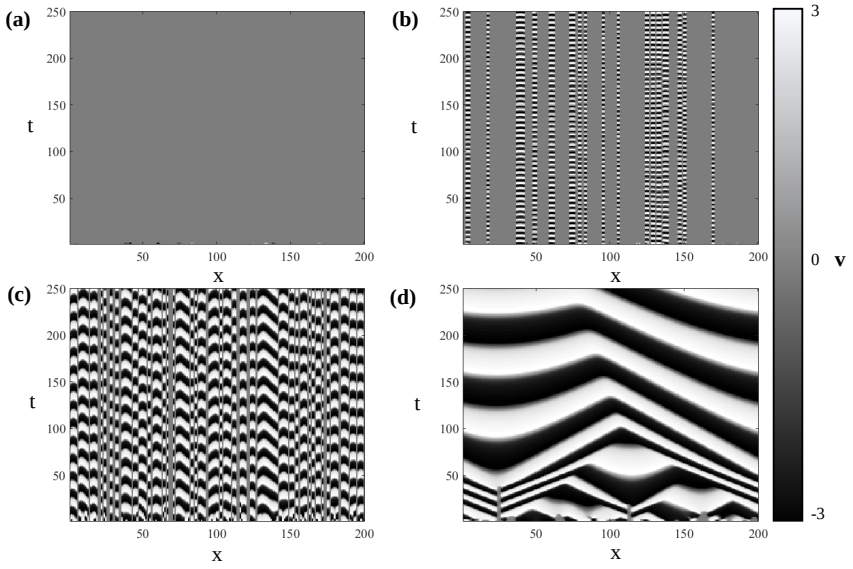

Figure 7: Position vs time plots for the v phase all 200 oscillators for 500 time units with same parameter sets as for Figure 6. White are oscillators with $v = 3$, black are oscillators with $v = -3$ and gray are oscillators with $v = 0$. (a) $(r_b, D) = (0.57, 0.95)$. (b) $(r_b, D) = (0.54, 0.85)$. (c) $(r_b, D) = (0.42, 0.20)$. (d) $(r_b, D) = (0.39, 2.65)$.

due to electronic effects as the wave back behaving as a trigger wave front [51]; however, that is not the case for FHN5. Not only can this model sustain a single alternating wave, but up to three for the size of $N = 200$.

The full dynamics in the range of D and r_b values we studied can be seen in Figure 9 where we use the order parameter ϕ identified with color. The transition between the different states where purple ($\phi = 0$) indicates that all the cells are in the oscillatory state and red ($\phi = 1$) indicates that all the cells are at the fixed point. The white dashed line in Figure 9 shows a phase transition, below which, a simulation with the same percentage of fixed points compared to a case above, will result in smaller and more island. Above, the islands will be bigger and there will be fewer of them.

Looking more closely at the what is happening in this phase space, we plot the average number of islands $\bar{n}$ that form at steady state. We find that similar to the phase transition in ϕ, there is a phase transition in the number of islands that form,

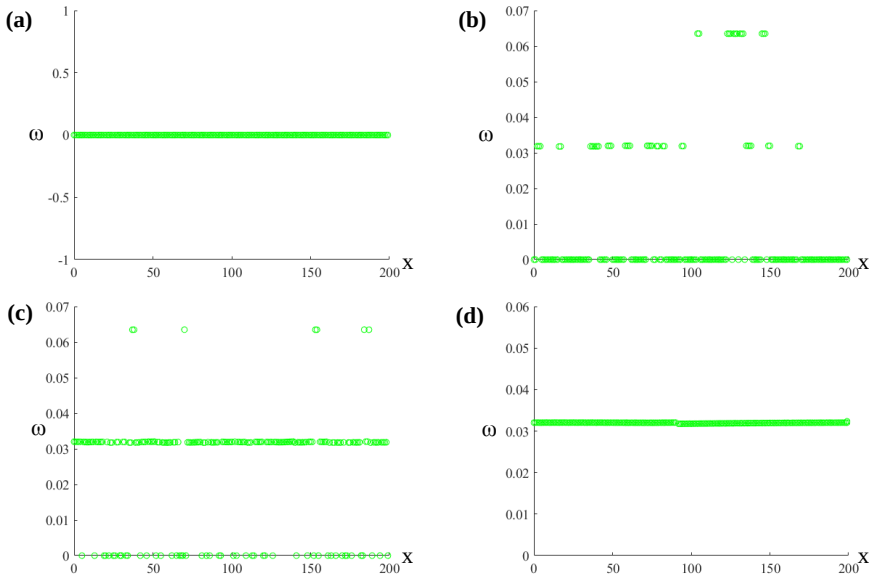

Figure 8: Snapshot of (x, ω) for all oscillators in phase space at $t = 500$ with same parameter sets as Figure 6. (a) $(r_b, D) = (0.57, 0.95)$. (b) $(r_b, D) = (0.42, 0.20)$. (c) $(r_b, D) = (0.54, 0.85)$. (d) $(r_b, D) = (0.39, 2.65)$.

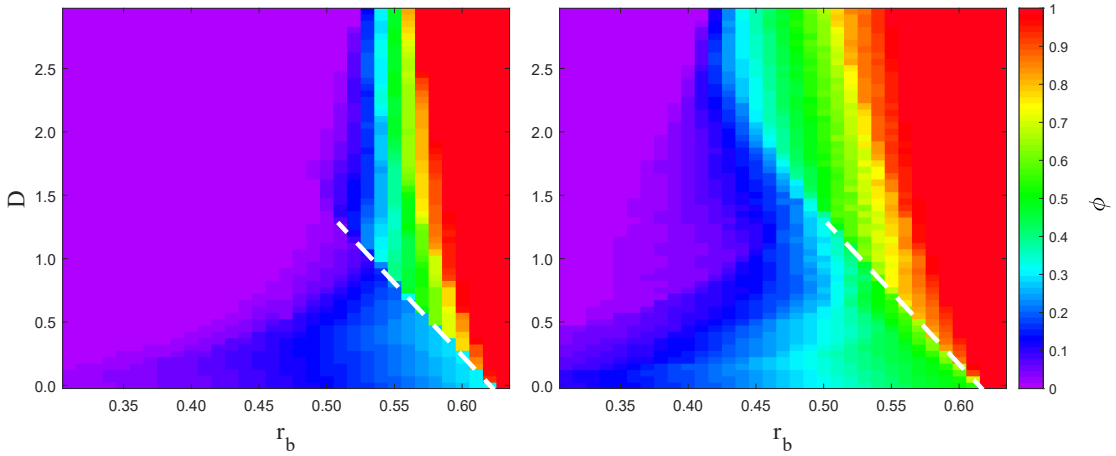

Figure 9: (r_b, D) phase space showing the percentage of fixed point cells ϕ for 1D system with nearest neighbor coupling and periodic boundaries. Region I (purple) shows where all cells are attracted to the oscillating cycle. Region II (red) shows where all the cells are attracted to the fixed point. The other areas are where chimera states exist. The white dashed line shows a change in the dynamics of the chimeras. Left, $\epsilon = 0.01$. Right, $\epsilon = 1/d$

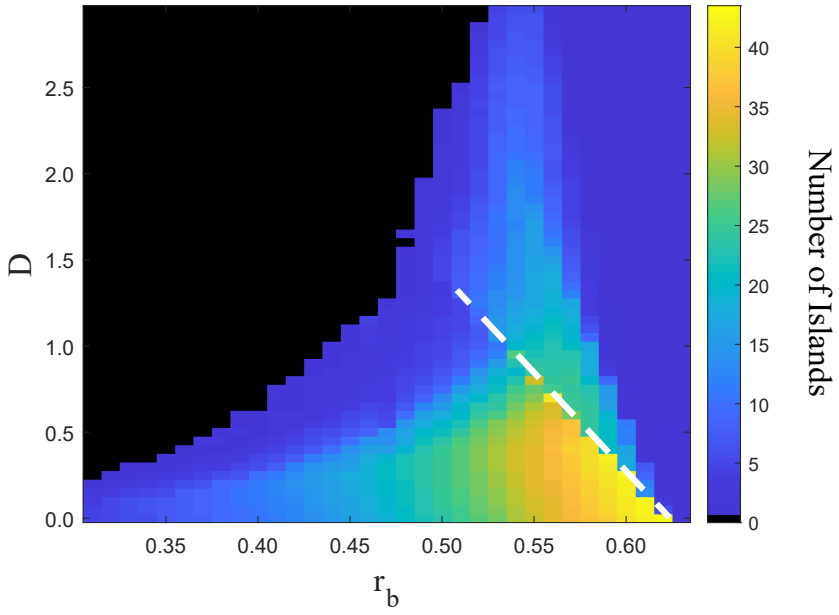

Figure 10: Phase space for number of islands that form for different parameters sets for 1D FHN5 200 oscillator system with $\epsilon = 0.01$. The black region is where there are no islands and all cells are oscillating. The dashed white line is the same as in the plot for the number of total fixed points. Below that line, there are many more islands that appear. Above that line there are much fewer islands even though there are more fixed points.

showing a sudden decrease which can be seen in Figure 10. However, Figure 9 shows that the total number of fixed points actually increases across this phase transition. To understand what happens, we calculate what the average island size is for our set of parameters.

To do this, the total number of fixed points ϕ can be divided by the by the average number of islands:

$$\bar{a} = \frac{\phi}{n} \tag{28}$$

and measure the average size of the islands $\bar{a}$ that form for each parameter set.

Indeed, when choosing two parameter sets that have the same number of total fixed point cells on either side of the transition, the island size varies significantly.

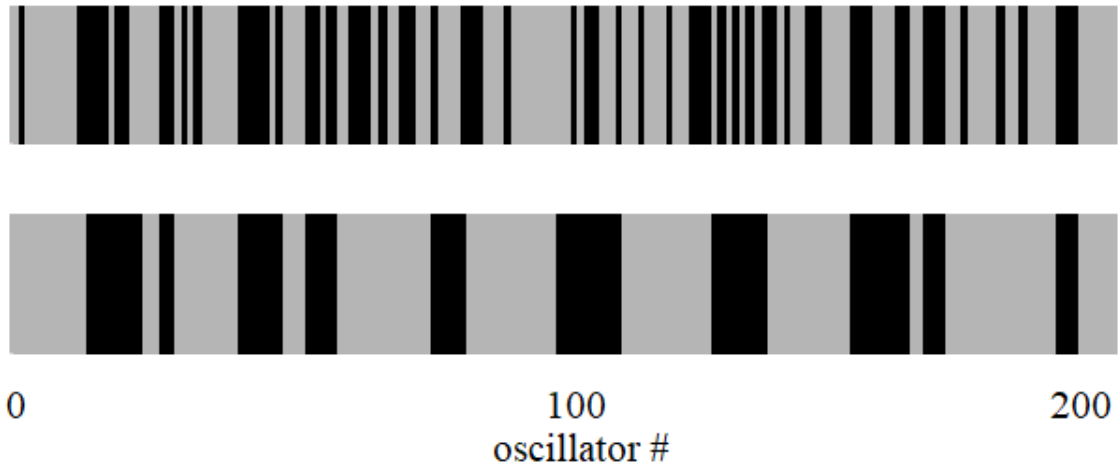

Figure 11: Snapshot of the variables v_i for t=10000 stating with the same initial conditions for (v_i, w_i) for (a) $(r_b = 0.55, D = 0.75)$ (b) $(0.54, 1.25)$. Each simulation reaches a steady state with $\phi = 0.395$ of the cells in the fixed point attractor. Gray are oscillators which are oscillating. Black are oscillators which are in the fixed point attractor.

Figure 11 (a) shows a snapshot of a simulation with parameters picked below the phase transition. The islands are on average 1.7 cells wide and a total of 78 fixed point cells. Fig 11 (b) shows a snapshot of the same initial conditions but above the phase transition and in this case with the same number of fixed points, the islands are a bit bigger at about 5.2 cells on average and there are fewer of them.

2.3.4 Dynamics in a 2D grid lattice

Similarly, the dynamics of a 2D grid lattice of FHN5 oscillators can be investigated. For this case, each oscillator has four nearest neighbors coupled with diffusion on a $N = 200 \times 200$ periodic lattice. In this case, the dynamics are much richer: traveling waves are not limited to one part of our phase diagram as they are in the 1D case.

Just as in the 1D, a phase diagram can be made showing ϕ, the average percentage of fixed points per parameter set. This is seen in Figure 12 for $\epsilon = 0.01$ and $\epsilon = 1/d$. This phase diagram has a similar structure as the 1D phase diagram, however, the area where chimeras are accessible is smaller. Again, the discontinuity in the average

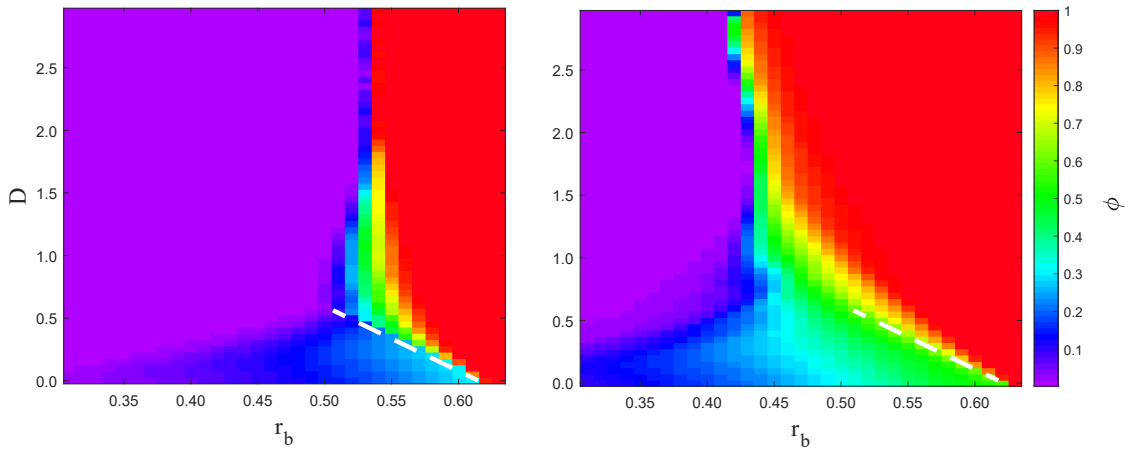

Figure 12: (r_b, D) phase space showing the percentage of fixed point cells ϕ for 2D system with nearest neighbor coupling and periodic boundaries. Region I (purple) shows where all cells are attracted to the oscillating cycle. Region II (red) shows where all the cells are attracted to the fixed point. The other areas are where chimera states exist. The white dashed line shows a change in the dynamics of the chimeras. Left, $\epsilon = 0.01$. Right, $\epsilon = \epsilon_H = 20$.

number of fixed points can be seen, which is emphasized with a white dashed line. This line is at a slope that is less steep than it is for the 1D case. Again, this does not appear dependant on ϵ.

In 2D, the chimera states can have a few different patterns. One case which is shown in Fig 13 (a) is when most of the space has waves that are traveling through out with island of fixed points that are small and sparse. After a transient period, these fixed islands will remain and the wavefronts and oscillation period will become constant. Another case which is shown in Figure 13 (b) is when most of space is fixed and there are islands which will oscillate at a constant rate. Again, the sizes and shapes of these islands will remain the same after a transient period.

These different dynamics can also be thought in terms of percolation theory: gray locations block waves of oscillations from traveling though; in the case where these fixed cells are disconnected (Fig 13 (a-d)), the waves can transverse the rest of the medium. The discussion section discusses more thoughts and possible open questions

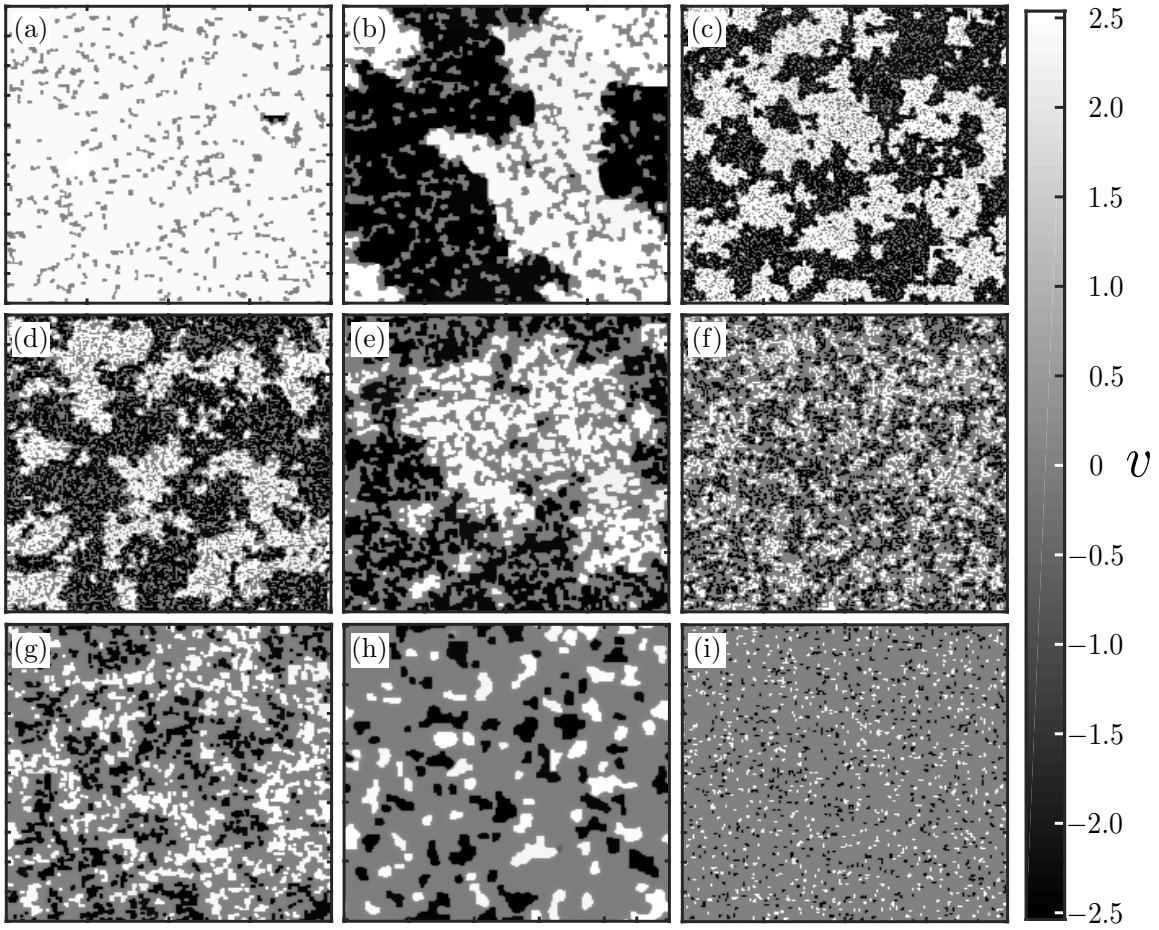

Figure 13: Nine 200×200 spatial dynamics of v variable with periodic boundary conditions for parameters (r_b, D) of (a) $(0.50, 0.85)$ with 9.8% fixed, (b) $(0.51, 1.05)$ with 22.2% fixed, (c) $(0.57, 0.25)$ with 30% fixed, (d) $(0.53, 0.50)$ with 41.2% fixed, (e) $(0.52, 1.05)$ with 48.8% fixed, (f) $(0.53, 0.70)$ with 64.7% fixed, (g) $(0.57, 0.30)$ with 68.5% fixed, (h) $(0.53, 1.50)$ with 76.0% fixed and (i) $(0.59, 0.20)$ with 90.2% fixed. White and black regions are cells that are oscillating. Gray are cells that are in the fixed point basin.

for continuing studying in this direction.

2.3.4.1 Spiral Waves

For 2D, there exists more dynamics that were not possible in 1D. One such dynamics is the spiral wave which can arise in chemical and biological systems such as the Belousov-Zhabotinsky chemical reaction[52], during ventricular fibrillation in the heart[25], or retinal spreading depression[53]. Spiral waves are discussed more in depth in Chapter 3.

For initial conditions that will form the spiral wave in 14, for $\epsilon = 0.01$ we do the following:

$$\begin{aligned} v_{ij} =& 2\cos\Big(\arctan\big(\frac{j-n/2}{i-n/2}\big)\Big) \\ w_{ij} =& 3\sin\Big(\arctan\big(\frac{j-n/2}{i-n/2}\big)\Big) \end{aligned} \tag{29}$$

where (i, j) gives the spatial location of the oscillator and n is the length of the side for square domain. Parameter ϵ is increased to 0.1 and integration parameters are changed to $dt = 0.0025$ and $dx = 0.5$. In order for the spiral wave to be sustained, we implement Neumann boundary conditions. Once the spiral is initiated, it persists for the duration of the simulation.

However, for $\epsilon = 1/d$ spiral waves form spontaneously. For a large enough D in the Region I of our phase plot in Figure 12, spiral waves can occur from random initial conditions. Figure 15 shows long term dynamics from the same initial conditions of a subset of parameter sets from the phase plot. Spiral waves with shorter wavelengths appear spontaneously for parameter sets in the upper left of the phase plot. The upper right shows systems with will settle at the fixed point solution for all oscillators. In the middle of the parameter set, simulations will produce dynamics of mostly fixed points with spots of oscillations

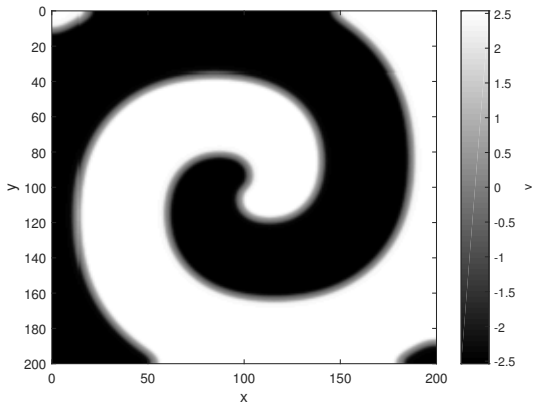

Figure 14: Spiral wave in the v variable that forms and persists in the FHN5 with 200×200 cells, $\epsilon = 0.1$, $D = 6.0$, $r_b = 0.45$, $dt = 0.01$ and Neumann boundary conditions. Phases were plotted at t=1000.

Besides spiral waves, traveling waves, fixed point islands, and oscillating islands, a new structure that forms spontaneously in the chimera regime are what I call "adjacent counter-propagating waves" (ACPW). These are waves that propagating anti-parallel next to each other through part of the 2D system. An example of this is shown in the blow up of the chimera that forms in Figure 16. For these cases, the waves look as if they pass next together along an unseen boundary. These ACPW are sustained for the duration of the simulation.

2.4 Conclusions and Discussion

Chimeras, spatio-temporal patterns that can occur from coupled identical oscillators, were once thought to only thought to occur if non-local coupling was implemented. We have implemented an extension of a well studied model, the FitzHugh-Nagumo model, which is able to produce chimeras in both 1 and 2D with strictly local coupling between identical oscillators. This extension, dubbed here as FHN5, has two basins of attraction that uncoupled oscillators may be attracted to dependant on their initial conditions. There for, these chimeras which form spontaneously, unlike many previous examples, have two or more types of coherence, with no decoherence

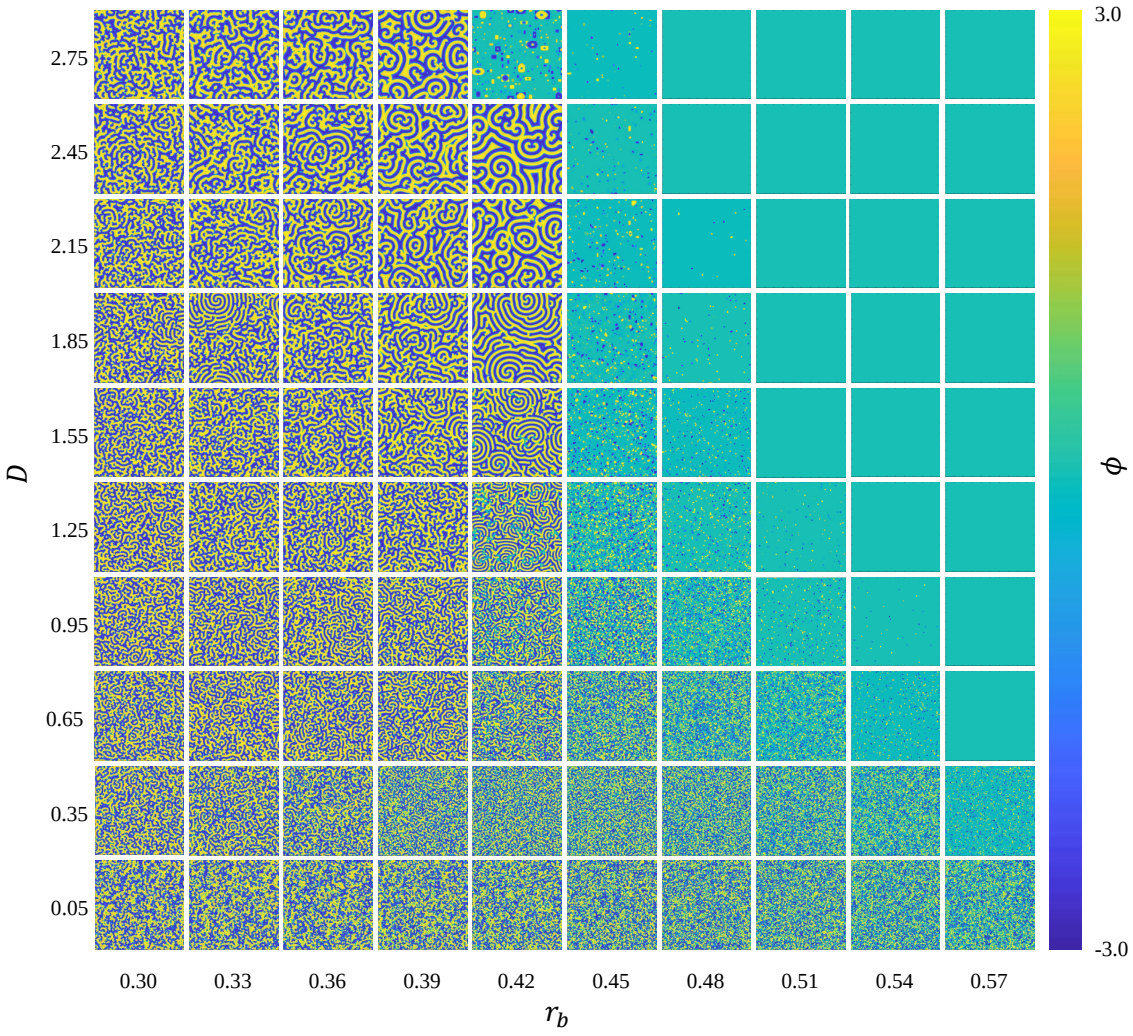

Figure 15: Snapshots of long term patterns that are observed in the 2D FHN5 model with $\epsilon = \epsilon_H$ for different parameter sets of (r_b, D). Simulations all started with the same set of random initial conditions for v and w. Images were taken at $t = 700$.

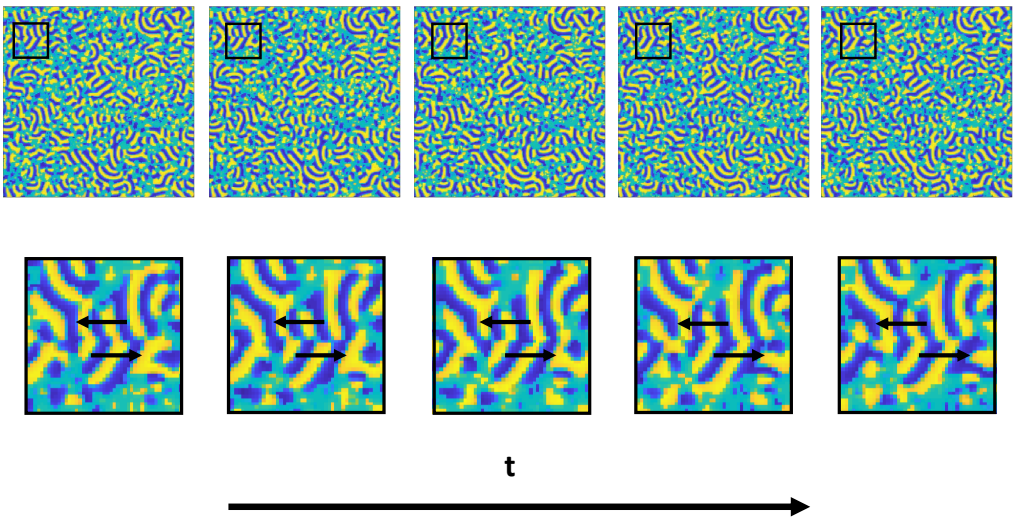

Figure 16: Snapshots of a chimera taken every 11 time-steps for $(r_b, D) = (0.43, 1.20)$. One section in each snapshot is blown up beneath the simulation to show "adjacent counter-propagating waves" which appear spontaneously and are sustained throughout the duration of the simulation. Simulation time moves from left to right for the images. Arrows in the blown up sections show the direction of the propagating wavefronts.

These chimeras are dependent on the diffusion strength between the FHN5 oscillators and on the relative basin attraction size of the two attractors in this system.

2.4.1 Percolation theory

One interesting question to investigate in the future is how the islands that appear in our 2D FHN5 can affect the waves that are traveling through the system. As a certain point, the number of fixed points in our system can grow so large that we do not have traveling waves any more, but we have islands of oscillations in a sea of unchanging fixed points. There is a certain percentage of fixed points that this is more likely to happen, however, the distribution of these fixed point will also affect how the waves are permitted to travel.

To analyze the dynamics we see in this system, we can take a page out of percolation theory. Percolation theory is an area of statistical physics which is the study

of cluster size in a system and can often give insight about how fractal-like (i.e. self-similar) the system is and how scaling works in the system. For percolation theory, if we have a lattice, we can say that each site is either occupied with probability p or empty with probability $1 - p$. p is then the occupation probability or the concentration of the system. We can also then define a cluster or a group of nearest neighboring occupied sites. In this case, p is similar to our fixed point percentage ϕ, which tells us the probability that a cell will be attracted to the fixed point attractor.

We can also define the cluster number $n_s(p)$ which is the number of clusters of size s per lattice site. In this chapter, I have presented just the average size of the islands, but I can also look more closely at the distribution of sizes that can occur in one simulation. When p is small, there is a very small chance that one cluster will percolate between two opposite boundaries of the system (i.e. span the system). As we increase the occupation probability towards 1, we will more likely be able to have a cluster span the system. Typically, a percolating cluster will appear around p 0.59.

We can also define the percolation threshold p_c. This is the concentration at which an infinite cluster appears for the first time in an infinite lattice. However, this is not well defined in a finite lattice. Looking at the 1D case, we can see that a cluster will only span the system in each site is occupied. This means that the concentration is 1 and there is one cluster that goes from 0 to N. Therefore, the percolation threshold $p_c = 1$. For 2D, this will tell us when a wave cannot travel from one side back onto itself.

2.4.2 Future experiments

Recent work by Arce, González and Fenton use the FHN5 cell model to describe the dynamics of a saline oscillator, a tabletop experiment involving two concentric containers of different density liquids connected by a small hole. The water from one container can flow into the other and after some time, the water from the second

container can flow back into the first creating an oscillation. The behavior of this system depends on the exposed areas of both containers, as well as the area of the hole and the concentration of the salt water. Their recent work showed that this oscillator can also be bistable, having dynamics where the flow can either oscillate as mentioned, or water can simultaneously flow from each container into the other (fixed point). They proposed the FHN5 to describe the two possible dynamics of this oscillator. What is currently uncertain is whether or not coupled saline oscillators can form chimeras like we see in simulations. This is an open area that can be continued to be explored.

Chapter III

LIVING SIMULATION: DYNAMICS OF A HUMAN SPIRAL WAVE

> *We then sailed on up the narrow strait with wailing. For on one side lay Scylla and on the other divine Charybdis terribly sucked down the salt water of the sea. Verily whenever she belched it forth, like a cauldron on a great fire she would seethe and bubble in utter turmoil, and high over head the spray would fall on the tops of both the cliffs. But as often as she sucked down the salt water of the sea, within she could all be seen in utter turmoil, and round about the rock roared terribly, while beneath the earth appeared black with sand; and pale fear seized my men. So we looked toward her and feared destruction; but meanwhile Scylla seized from out the hollow ship six of my comrades who were the best in strength and in might.*
>
> —Homer, *The Odyssey*, Book XII, lines 234-240

[1]

Just as cells in biological systems can form more complex behavior as a collective, groups of people also can behave as an excitable medium and cooperate, resulting in emergent behavior at larger scales. The idea to study the dynamics of groups of people is not new: there is research that has been and is currently being conducted on how people leave events [54, 55], how people line up or queue [56], how mosh pits occur at some of the heavier concerts [57][2], and even how a group of people who are standing or sitting in place at sporting events causes a wave to propagate, often dubbed the "Mexican wave" [58]. These studies have been of interest in order to understand how best to implement crowd control, reduce injury and minimize wait times. This chapter focuses on work similar to the "Mexican wave" study, but poses the question of whether or not a group of people can exhibit some of the other types

[1] Translated by A. T. Murray

[2] I have been to exactly one concert where a mosh pit happened and I did not take advantage of the research I could have been conducting there, unfortunately

of patterns that have been seen in other excitable media provided that they are given a certain set of rules. In this case, we treat our participants as if they are cellular automata and test if a spiral wave can be produced by their "activations." We also observe the effects of some participants not following the rules, and how properties of the dynamics that occur can change depending on the of physical set up parameters and human interaction.

3.1 Cellular Automata

While the dynamics of excitable media with spatial extent are typically encoded via a set of PDEs, usually in the form of a reaction diffusion model, they can also be described more simply with cellular automata that follow a set of rules. In fact, the first simulations of excitable systems were performed with cellular automata models [59] and also used to simulate the Mexican wave [58].

Cellular automaton is a discrete modeling method that is used to study a variety of systems in computer science, physics, mathematics, and biology [60, 61]. The discrete space and states used in this method makes modeling simple and fast and yet can still display a wide range of complex dynamics. In order to implement this modeling method, a "regular" grid of cells is defined where each cell has one of a finite number of states. By "regular," we mean each cell has sides that are of equal length with all interior angles being equal to each other. Examples include equilateral triangles, squares, and hexagons. These examples allow for a uniform tiling of a flat space.

The states of the cells can be a variety of types such as "on/off" (Game of Life) [62], red/green/blue or various other combination of colors, or a discrete set of numbers. The grid can exist in any finite number of dimensions, but for this project we focus on the two-dimensional case. A neighborhood of interaction also needs to be defined so that it is known which cells may affect other cells. Common examples of neighbors are depicted in Figure 17. The two main cases are that of the Von Neumann neighborhood

with what is called "Manhattan's distance" n and the Moore neighborhood. For the Von Neumman neighborhood, the Manhattan distance describes which cells a path can be constructed by treating the cells like square street blocks to travel that is of or less than that distance. Figure 17(a) shows an example of a Manhattan distance of 1 and (b) shows an example of a Manhattan distance of 2. The Moore neighborhood includes all cells that are 1 cell away from our selected cell, including the diagonals.

Defining the neighborhood is important in what over all patterns and dynamics can occur. The rules that cause cells to change states are also necessary for patterns and dynamics. Given these, the dynamics of the system can be studied. Let's first examine the well-known and studied "Game of Life."

3.1.1 The Game of Life

A famous example of cellular automata is in Conway's Game of Life [62]. It is called such because the rules are inspired by processes of life, which will become apparent when reading the rules. These rules are as follows:

- Rule 1: Any live cell with fewer than two live neighbors dies (underpopulation)
- Rule 2: Any live cell with two or three live neighbors lives on to the next generation
- Rule 3: Any live cell with more than three live neighbors dies (overpopulation)
- Rule 4: Any dead cell with exactly three live neighbors becomes a live cell (reproduction)

Examples of each rule case are depicted in Figure 18.

When these rules are implemented with certain set or initial conditions (the states of each cell), different dynamical patterns can spontaneously appear and may even persist. These can be classified into three types of patterns: (i) the still lifes, (ii) the oscillators with period n, and (iii) the "spaceships." Of particular interest for our

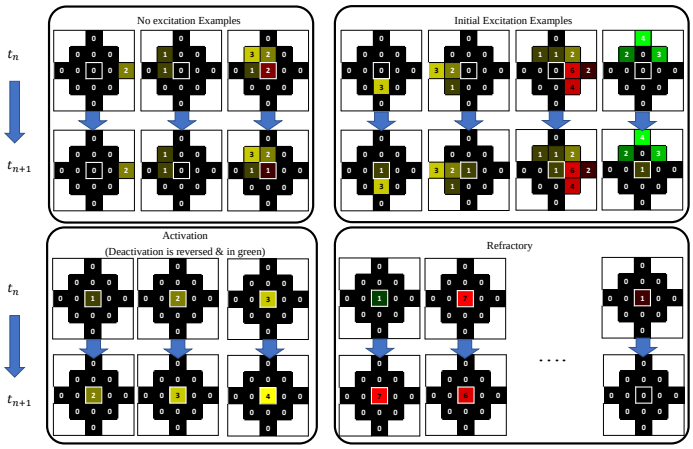

Figure 17: Three of the different neighborhoods that can be use when simulating cellular automata. The filled blue cell is the example cell and the orange shaded cells are the surrounding neighborhood. (a) Von Neumann's neighborhood with a Manhattans distance of 1. The only cells that affect the selected cells are the ones directly up/down and left/right of the selected cell. (b) Von Neumann's neighborhood with a Manhattans distance of 2. The only cells that affect the selected cells are the ones 2 steps away some combination of up/down and left/right of the selected cell if you can only step up/down/left/right. (c) Moore neighborhood. The only cells that affect the selected cell are those one step away, admitting the diagonal, as well as up/down/left/right.

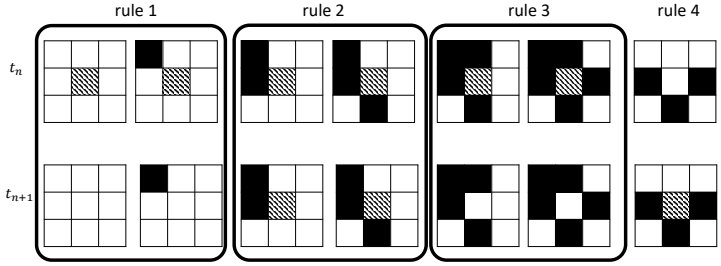

Figure 18: Game of Life rules visually using Moore's neighborhood. The top row shows examples of different situations at a particular time t_n. The bottom row shows how the rules affect the middle cell (the patterned cell) depending on the states of itself and its neighbors. Rule 1 shows two cases where the middle cell dies out because of underpopulation. Rule 2 shows two cases where the middle cell lives to the next generation. Rule 3 shows two cases where the middle cell dies due to overpopulation. Rule 4 shows a case where the middle cell is born due to reproduction of 3 neighboring living cells. Note that only the center cell is getting updated in this visual. In the regular implementation, all the cells will be updated simultaneously depending on each cells set of neighbors.

purposes are the last two types, where oscillating patterns can remain stable, and where patterns can move through the space of the system. However, they can all work together to form long lasting patterns

3.1.2 Wolfram's Classes of Cellular Automata

In 1983, Stephen Wolfram, who originally became interested in cellular automata and studied the statistical mechanics of these sorts of simulations [60], also became interested in what arbitrary cellular automata can do in terms of pattern formation for the system when started from random initial conditions. He found that these dynamics could be classified into four different types:

- Class 1: Nearly all initial patterns evolve quickly into a stable, homogeneous state.
- Class 2: Nearly all initial patterns evolve quickly into stable or oscillating structures.
- Class 3: Nearly all initial patterns evolve in a pseudo-random or chaotic manner. Any stable structures that appear are quickly destroyed by the surrounding noise.
- Class 4: Nearly all initial patterns evolve into structures that interact in complex and interesting ways, with the formation of local structures that are able to survive for long periods of time [61].

3.2 Spiral Waves

We first touched on spiral waves in Chapter 2 due to their appearance in the FHN5 model. However, let us now go into greater in depth in regards to what they are, where they have been observed, and what information can be measured from them for the purpose of this project.

Much like long wavelength traveling waves, spiral waves–or spiral vortices–are an additional type of structure that can be observed in 2D. At the spiral core, the magnitude of the amplitude vanishes and the phase is singular. the presence of a singular core can be found by integrating $d\phi$ around a closed path C, i.e.

$$\oint_C \nabla\phi \cdot \mathbf{dl} = 2\pi n, \tag{30}$$

where n is an integer representing the topological index, here known as winding number, of the spiral vortex, and ϕ is the phase of the medium at the particular location and time. These spiral waves propagate outwards from the core which we showed in a time slice of the FHN5 in 2D in Figure 14.

There are many biological systems where spiral waves can appear. In the body, studies on the uterine lining of pregnant guinea pigs [63], the cerebral cortex [64], graphical tongue [65], as well as the heart [66–68] have shown to exhibit spiral waves. These spiral wave patterns serve a variety of purposes: some inhibitory, some supplementary, and some still unknown. The mechanisms that form spiral waves can also vary.

Most of these spiral patterns in the human body are abnormal, but the most dangerous spiral waves can occur in the heart [69]. Spiral waves of electrical activity in the heart have been shown to induce tachycardia as the fast spiral rotation drives the heart to a faster contraction rate. When spirals break into multiple waves, the heart is in a state of fibrillation, a condition of fast, globally unsynchronized contraction in which the heart fails to pump oxygenated blood to the body. Without intervention, this behavior is deadly, killing more than 630,000 Americans die of heart disease each year [70].

3.2.1 Spiral Waves and Cellular Automata

Inspiration for creating spiral waves in crowds of people came from dynamics observed in colonies of giant honey bees [71]. Bees of the species *Apis dorsata* have a unique nest in which members of the colony cover the surface of the nest, packing together into a dense crowd of bees. When a hornet attacks the colony, the bees closest to the hornet flip over and repel the predator with their legs. Neighboring bees imitate and briefly flip over on their back before righting themselves. The result is a dynamic spiral pattern that propagates outwards through the colony which is also known as "shimmering" as seen in videos of [71]. In this image, which was taken from the video "Life in the Undergrowth" produced by the BBC, the wave of bees is excited by harassment by famed British natural historian, Sir David Attenbourough. Our goal was to reproduce the shimmering observed in the colonies of honey bees with a large crowd of people without requiring the harassment from a British nturalist. Surely, if bees can coordinate themselves in such a way, humans can too.

3.3 The Mexican Wave as an Excitable Medium

The Mexican wave, often seen at sporting games, is a synchronization phenomenon among excited fans where a column of people will stand with their arms up and sit back down while the next column of people repeats this same motion. When done correctly, this results in a plane wave that propagates through the medium of fans in the stadium, similar to waves propagating through excitable media [58].

For this study, Farkas et al. analyzed videos of 14 different waves in football stadia with over 50,000 participants [58]. For their studies, no instructions were given and participants were seated in the the stadium at the typical spacing between seats; however, seats may not always be filled and there are typically open spots through out the stadium. They measured that the spontaneous wave that formed moved at

a speed of 12 meters (20 seats) per second and had a width of about 6-12 meters—which is an average width of 15 seats. The people who are involved in the excited part of the wave are on average a few dozen standing simultaneously. The wave then proceeds around the stadium.

The way this study modeled the behavior of the participants was by considering each as having one of three states: active (standing and waving), refractory, resting/excitable state. Two different models were studied which involved differences in the stochasticity.

One major result is that triggering a wave requires a critical mass of initiators and depends on the activation threshold of individuals on average. Each individual in their model is set at a certain activation threshold $c_i \in [c - \delta c, c + \delta c]$ at random. If the weighted concentration of active people within a radius R was above that threshold, that individual will also excite. The weight decreased exponentially in distance and changed linearly with the cosine of the direction so that people that are between the individual and the incoming wave will have an influence w_0 times greater than people in the other direction. This anisotropy is used because of the individual's anticipation of the wave coming after the initial instigation of the wave.

Using these same ideas, we have studied how a spiral wave can be instigated, sustained, and breaken up in a grid of people.

The heart can be studied as an excitable medium where, due to the natural refractory period of caridac cells, a plane wave can break and turn into a spiral wave [72, 73]. This can lead to fibrillation which is one of the leading of death in the US [74]. We investigate whether a similar spiral wave can be sustained in a collection of people if given proper rules and initial conditions. This refractory period is something that is present in models of excitable media, but is not necessary for the study of the Mexican wave as the wave front never reaches the wave back while individuals are in their refractory period.

3.4 Experiments of Human Waves

The experiments are carried out by collecting volunteers to act as our excitable medium. Volunteers were offered donuts or pizza, which in hindsight was ironic given the relationship between spiral waves and sudden cardiac death; however, perhaps these experiments provided more physical activity than Tech students and staff would have seen otherwise during the time of the experiment. No other possible benefits or harm were expected for the individuals. For the images in this thesis, we have blurred the faces of our volunteers.

For 1D experiments, volunteers were asked to stand in a line, and for 2D experiments, volunteers were asked to stand in a grid lattice. The number of volunteers depends on the experiment. The volunteers were told the following rules:

1. An individual starts at rest in a standing position with hands down by their side. This is considered the default resting state.

2. If any of the nearest neighbors (left or right) lifts their hands over their head, the individual then raises their own hands over their head (activation).

3. After activation, the individual brings their hands down and cannot excite again (refractory) until after their hands are all the way down.

The number of neighbors is set by the dimensions and topology of the experiment. In 1D, a participant either has one or two nearest neighbors determined by whether they are at in the middle or end of the system. In 2D, a participant has 2-4 nearest neighbors determined by whether they are the corners, lateral boundaries or middle of the system.

For the initial conditions, certain participants are asked to start in the activated state and certain participants may be asked to be in refractory so that they will not activate at the start of the trial. All other individuals are asked to be in rest. We

started recording and asked the end participant to begin. This is done multiple times with excitations started from either end of our cable. A camera was placed so that the entirety of the 1D line is in view and multiple trials are recorded.

For 1D experiments, initial conditions that we test include which end of the 1D line the excitation starts. We also test the effects of the orientation of participants and spacing between the participants on their reaction times and wave speeds. For the 2D experiments, we study the effects of various initial conditions including corner activation, lateral activation, and spiral wave activation. A camera is placed in front of the 1D and small systems or on top of a near building for the larger size systems to get and an overhead view of the activation and multiple trials are recorded. To process these videos, a tracker program is used. Depending on the current trial the left or right hand of each person is tracked (which ever is clearer, i.e. not hidden behind an individual standing in front of them, but also in some cases, an individual may not raise both hands during activation). The time series of each person is plotted and the action potential duration (APD), wave speed, and wavelengths are measured.

The APD is a term borrowed from physiology and describes the time it takes for the membrane potential to rise and fall. The entire cycle includes (i) the APD, the (ii) refractory period during which the cells are unable to re-excite, and (iii) the resting period where the cells can re-excite. An example of this is shown in Figure 19. The APD can be measured by timing the total time it takes for participants to completely raise and lower their arms and the total period of the cycle can be measured by timing from the start of one action potential (AP) to the start of the next AP.

These measurements are reproduced in a simulation, created through cellular automata. The purpose of the simulations is to test how human interaction may be coupled in a different way than the rules which were given to individuals. Putting in the same rules we give our volunteers, we expect to see the same dynamics. However, for the 2D cases, this is not what is observed and we discuss why that may be the

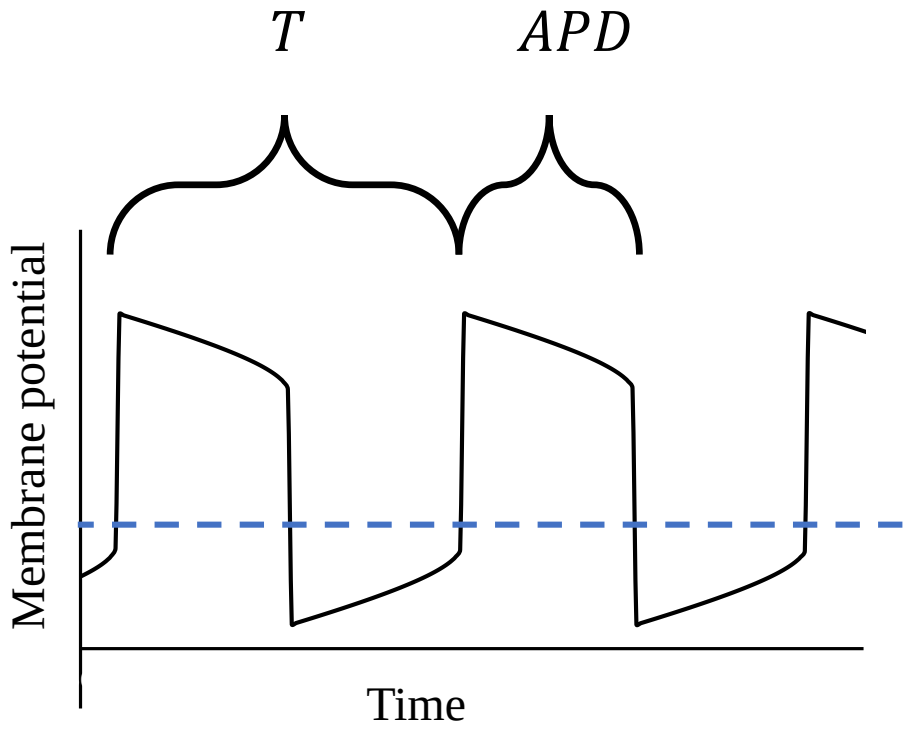

Figure 19: Example of an action potential. The period T and the action potential duration (APD) are shown. The refractory period isn't visible in this image, but occurs after the APD.

case.

3.5 1D Waves

In order to further understand how interactions between people can result in a wave, we first look at a line of people. From these experiments, we measure the effects of spacing and orientation on wavelength and wave speed.

3.5.1 In a Cable

For our 1D experiments, we had 16 volunteers stand in a line one arm-length away from each other and face toward the camera which is on the normal to the line, as can be seen in Figure 20(a). We ran five trials where the volunteer on the left end and five trials where the volunteer on the right end was asked to start a wave and all other volunteers were asked to follow the instructions above. We tested from both ends in order to remove any directional biases that could appear.

Having the volunteers now face to the right, we initiate a wave on the right so that the wave is coming from the front of each person for five trials, which is shown in Figure 20(b). We also initiated the wave from the left end so that the wave is traveling from behind for five trials.

We track the hands of the individuals via "DLTdv digitizing tool", Tyson Hedrick's MATLAB tracking program [75]. The time series of each individual was normalized and plotted The period and APD were measured. We calculate that the wave propagates an average of 3.2 people/second when the wave is coming from left or right of the participant. One trial is shown in Figure 20(c) which shows the normalized action potentials of each participant. The slope of the diagonal line through the 16 time series is the wave speed in people/second. However, the wave propagates an average of 4.0 people per second when the wave is coming from in front of them. This shows that the direction of the wave affects the wave propagation speed, which will matter in the 2D lattice case. For the Mexican Wave, the propagation only comes

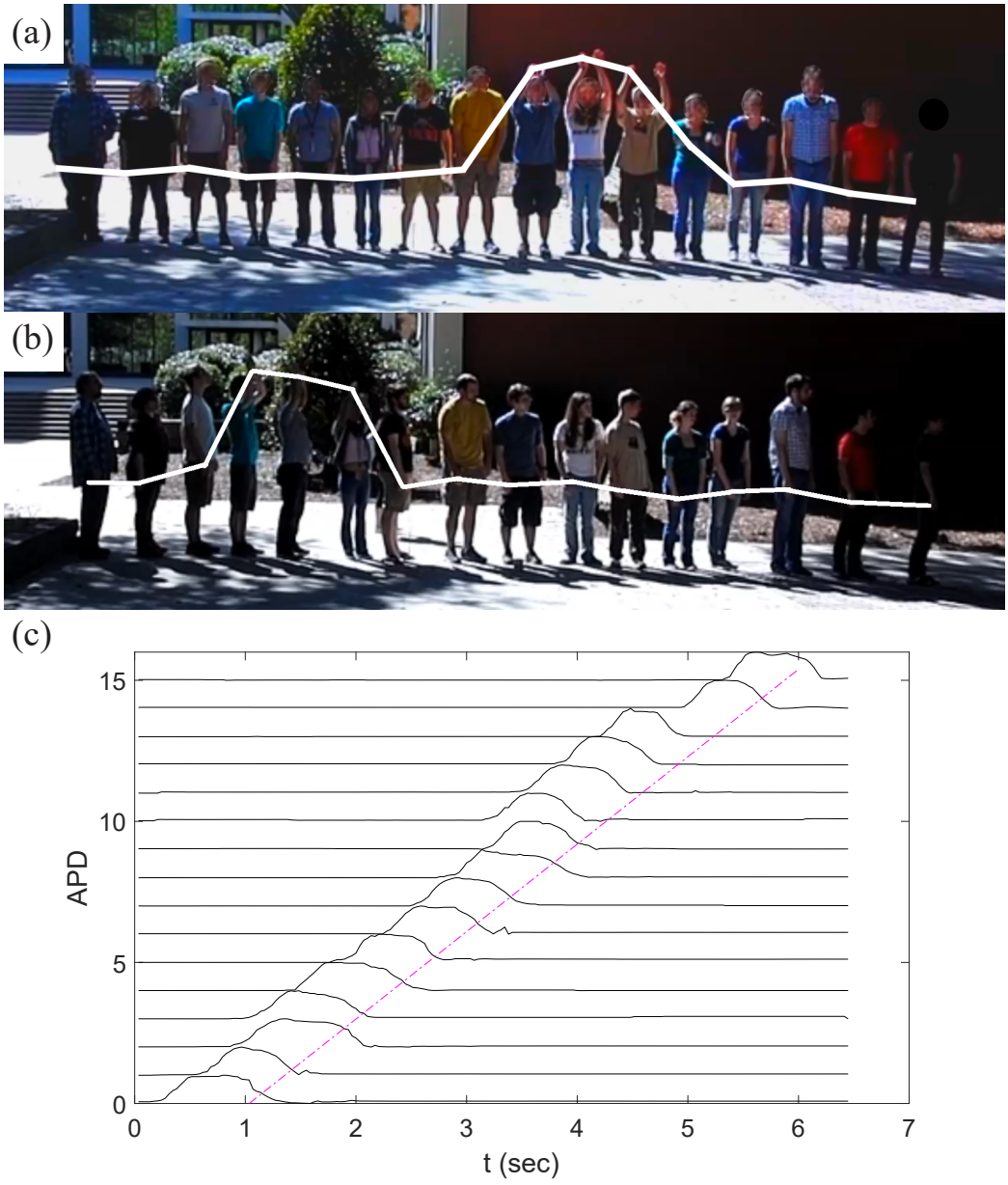

Figure 20: (a). Image of experiment involving 16 participants preforming "the wave." A white line shows the current measured height of each of participant used in data. (b) Similar but the participants are facing to the left and the wave is coming from in front of them. (c) Plot of normalized height of hands of each participant in time. The time series are shifted up such that each time series' base line starts at a different value.

Figure 21: 33 participants standing shoulder to shoulder to form a ring. A wave was started at the bottom and the person with their hands up is the participant starting in refractory. The image was taken when the wave was halfway around the circle with 6 participants in activation.

from the left or the right so we do not have a similar issue with speed depending on the propagation of the wave.

3.5.2 In A Ring

We have 33 volunteers stand so that they make a closed ring. The volunteers stand shoulder-to-shoulder and one participant initiates a wave. A participant on one side of the instigator is asked to be in refractory and every other participant is in the rest state. Because of this set of initial conditions, the wave transverses the ring in one direction and only stops when we stop the experiment.

3.6 2D Waves

3.6.1 Lateral and Corner Activation

First we instigated a pulse wave. We did this in two ways: (i) by activating one participant in the middle of an external side and (ii) by activating one of the four corners. In the first case, a participant activated and has three nearest neighbors expected to activate on the next time step. A roughly circular pulse will propagate out from the initial excitation. The wavelength can be measured by counting the number of activated participants across the direction normal to the motion. The

Figure 22: A wave is initiated in the lower right and propagates towards the upper left. The wave propagation is in the form of a slightly obtuse angle with a wavelength of 7 people.

wavelength is measured to be about 6 people and the wave speed is measured to be 2.9 people per second.

For the corner activation, a participant at the bottom right corner starts in activation and proceeds to refractory. A wave will propagate from this corner in the form of two plane waves connected at a corner (or an L-shaped wave). This is seen in Figure 22. The APD is measured as in the previous experiment and is 7 people and the wave speed is 3.0 people per second.

3.6.1.1 Collisions and Wave Annihilation

For this experiment, participants activate two waves beginning at opposite corners of the system colliding at the center with the same rules mentioned above. To do this, the opposite corner individuals begin in activation state and proceeds to refractory as the neighboring individuals were left to propagate the waves. This experiment also resulted in a clearer wavelength and wave speed as the wave traversed the larger system of 500-600 individuals.

As expected from a reaction diffusive system [76], when the two waves collided, the activation died out leaving participants in rest. Figure 23 shows still frames of this occurring.

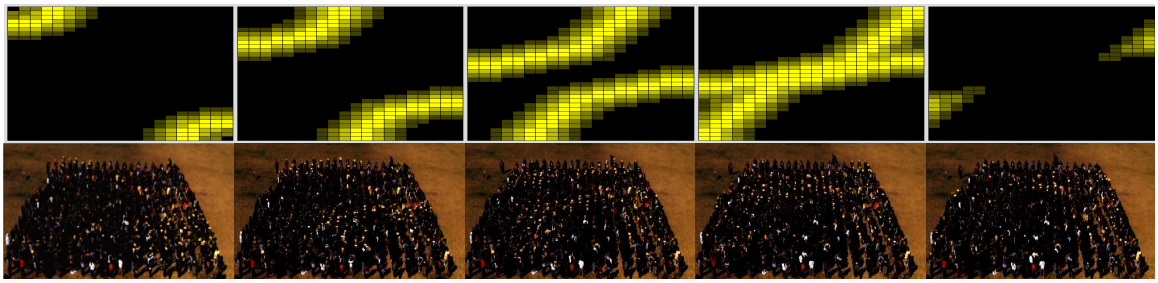

Figure 23: Two waves excited from opposite corners in simulation and experiment. The upper left wave was excited slightly later than the lower right one. The two waves approached the center of the grid where they met and were annihilated.

3.6.2 Stable Spiral Waves

In order to start spiral waves, participants were given a particular form of initial conditions. To do this, we use the same initial conditions used in some cardiac simulations: a half row of activated participants with a half row of deactivated participants directly parallel. All other participants are in the rest state and can activate at any point. By doing this, the symmetry of the wave, which would normally propagate outward in all directions is broken. The wave now is forced to propagate around the block of refractory cells, which will only be able to activate after a short time period later.

The average activation and deactivation times of our participants, the average rotation speed of the spiral, and the average wavelength of our spiral are measured from the trials conducted. To do this, videos of our successful spiral runs are processed in MATLAB by taking the difference of successive frames which will make all pixels that are the same appear black and those where there is motion white. The white pixels are then highlighted yellow and overlaid on top of the original image in which motion can then be tracked easier.

We expect the dynamics to be different from the 1D case due to the system being more coupled— i.e. each cell has more neighbors to couple to i.e. and that coupling has an orientation since our individuals do no have a field of view of their entire

neighborhood simultaneously.

3.6.3 Size Effects

We have done multiple cases of the human spiral wave with different size groups of volunteers. We have data for systems as small as 2×2 individuals to as large as 25×25. Next, let's examine how size of the system affects wave speed, rotation speed, and wavelength. In particular, we will consider two cases as the experimental set-ups are slightly different and seem to affect the dynamics in these cases: (i) sitting and (ii) standing.

3.6.3.1 Classroom experiments

For these experiments, we have volunteers sitting in desks in a lecture hall. These are on risers such that each subsequent row is 38cm higher than the previous row. For these experiments, participants sit in the desks and so are also unable to rotate their bodies as easily as in the standing cases, an example of which is shown in Figure 24. However, the same rules that were given in the larger cases discussed above were given to these participants.

There are a total of 12 trials ranging from grids of 2×2 participants to 13×13. Spiral waves were initialized as described above and videos of each trial were recorded. For each trial, individuals were tracked using DLTdv5 [75] and the times series were normalized. This was done as follow,

$$y_{norm}(t) = fracy(t) - y_{min}y_{max} - y_{min} \tag{31}$$

which was done for each excitation. This is because sometimes the participant would shift in their seat or change the starting or ending position of the hand (in lap, on desktop, on back of chair etc.). Then, the period T was measured at 25% of the height of the signal from the start of one activation to the start of the subsequent

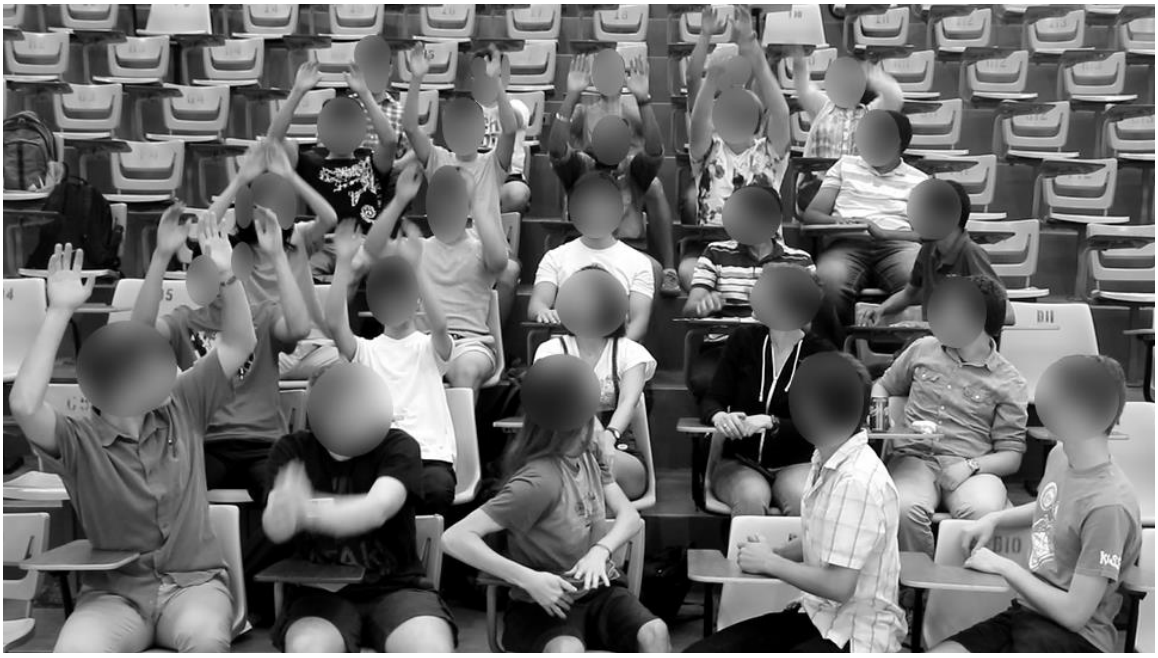

Figure 24: A snapshot of a classroom experiment of $L = 5$ from a spiral that is rotating counter-clockwise.

activation.

Figure 25(a) shows the average APD measured per trial of 12 trials total. This was plotted per the system length $L = \sqrt{N}$ where N is the number of participants. The error bars denote the standard deviation per trial. Our data shows that L has little-to-no effect on the APD of the individuals. The APD for these seated experiments is 0.97 ± 0.01 seconds. The period of activation T is also plotted vs L in Figure 25(b). Unlike the APD, the period appears affected by the system length. More experiments are needed to determine a stronger relationship; however, we can conclude there is a positive relationship between L and T, meaning that the rotation speed of the spirals is larger for smaller systems.

For these system sizes, we are not able to clearly determine a wavelength, which appears larger than the system size.

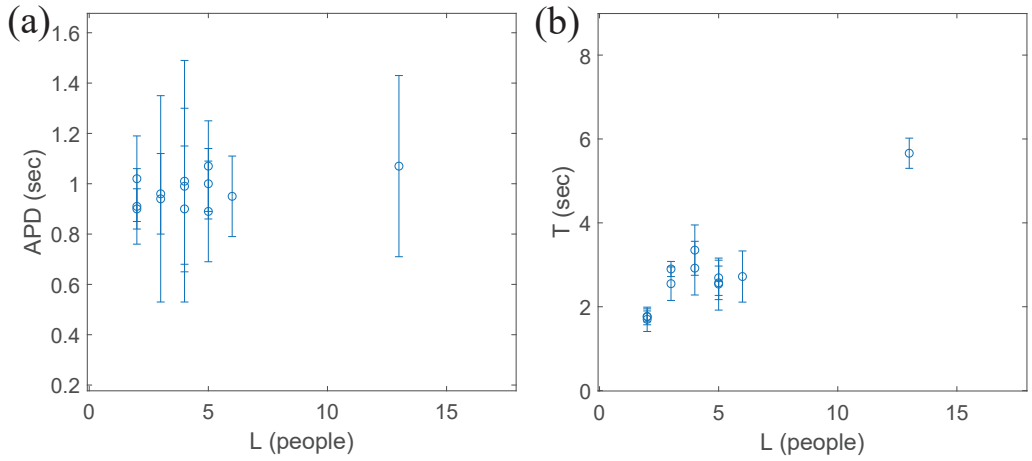

Figure 25: (a) Average APD in seconds plotted vs the length of the system in number of people. (b) Average period in seconds plotted vs the length of the system in number of people. Error bars in both plots refer to standard deviation.

3.6.3.2 Field Experiments

We performed two sets of experiments with 600 people organized into approximately square grids of 25×25, as shown in Figure 26. All participants were provided the cellular automata rules mentioned above and were also given a yellow sheet of paper that helps to distinguish in aerial view when they have their hands up, and we proceed to initiate propagating waves. Initiation of a spiral wave requires breaking the symmetry in the propagation of a wave; therefore, to initiate a spiral wave we used the following initial conditions: (1) forming a line of excited elements at the center of the crowd halfway into the domain as shown in the first image of Figure 27 and (2) designating a line of initially refractory elements directly to the right of the excited line for the first few times steps, which ensures these elements will not be activated by their neighbor at the start but could be activated later on. In these experiments, we could initiate spiral waves (Figures 26 and 27 middle) with a given chirality (right or left handed) by modifying the initial condition, i.e. which side of the initial excited line was made refractory (left or right). While the Mexican wave can also propagate left or right, the key difference is the half line of initial activation

Figure 26: Left. Screenshot of our 2015 experiment where a spiral of people holding yellow papers have their hands up. Right. Same image but the spiral is highlighted to be visually clearer.

and that the wave can propagate in all directions causing it to begin to curve around the initial refractory line.

Analysis of the experiments showed that the waves have a width of activation of 7 people, an average propagation speed of the plane wave of about 3 people per second, and a rotation period averaging 4.5 seconds.

An unexpected result is that the activation APD is half as long in the classroom cases as compared to that of the much larger cases. This is likely because participants are not putting their arms completely down at their sides but instead are resting their hands on the desk top which is approximately elbow-height.

3.6.4 Simulation

The values from the field experiments can be reproduced in a cellular automata simulation where the elements or "people" are given a 2 seconds excitation time and a refractory time of 1.5 seconds before being able to activate again. Cells get excited as soon as any of their four neighbors become excited, and we use a time step of 0.25 seconds and give each element a size of one person. Cells take on four states: rest (black), activation (yellow), deactivaton (green), and refractory (red). While in activation or deactivation, the cells can take an activation value $\{1-4\}$, otherwise cells have an activation value of 0. Cells also have a refractory value $\{1-7\}$ which

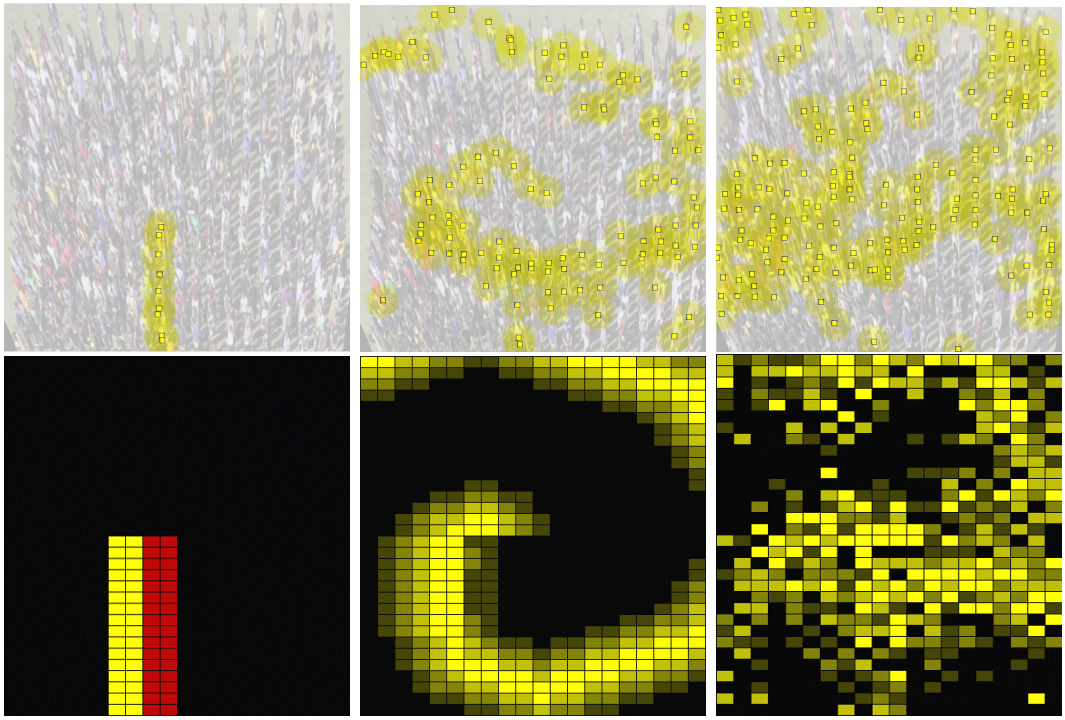

Figure 27: Top. Single frames of an experiment where volunteers with their hands up are highlighted and the background is greyed out. We have snapshots of the initial conditions, a little while later after the spiral has formed, and in a different trial after the spiral has broken up. Bottom. Simulation with neighborhood of Manhattan size 2.

begins after the activation returns to 0 and decreases from 7. Once the refractory value reaches 0, cells are in rest state and take an activation value of 0 again.

A threshold value is defined which determines if a cell activates. If the sum of the activation values of all cells in a particular rest cell's neighborhood is greater than that threshold, the cell turns yellow and begins activation. Figure 28 shows 4 different threshold values y_t in the simulation at different times to match the dynamics to the corner activation experiments. Increasing y_t increases the excitability of the cells and causes the wave to propagate faster and also changes the shape. Using a $y_t = 2$, meaning the sum of the neighborhood values must be greater than 2, matches the corner wave speed and shape the best.

A striking difference emerged between experiments and simulations. While cellular automata simulations will produce spiral waves that follow a diamond shape (Figure 29), which is that of an unresolved spiral, the waves from the crowds are relatively smoother and spiral waves are curved. The smoothness or curvature of the waves can be explained by small difference in reaction time between people and the observation that people actually react to more than just their four nearest neighbors. We therefore increased the dispersion of the model by allowing a total of twelve neighbors (von Neumann neighborhood with Manhattan size = 2) to be sensed by each element (person) as well as increasing the activation threshold of the nearest neighbors. With these modifications, the model can reproduce the experimental spiral wave dynamics including speed, wavelength and period as seen in Figure 27. The new rules can be seen visually in Figure 30.

With this process, the number of activation steps determines the wavelength, which can be seen in Figure 31. These simulations show examples of how the number of activation steps affects the wavelength (the number of cells across the activation). This along with the number of step for the refractory state determine the period of

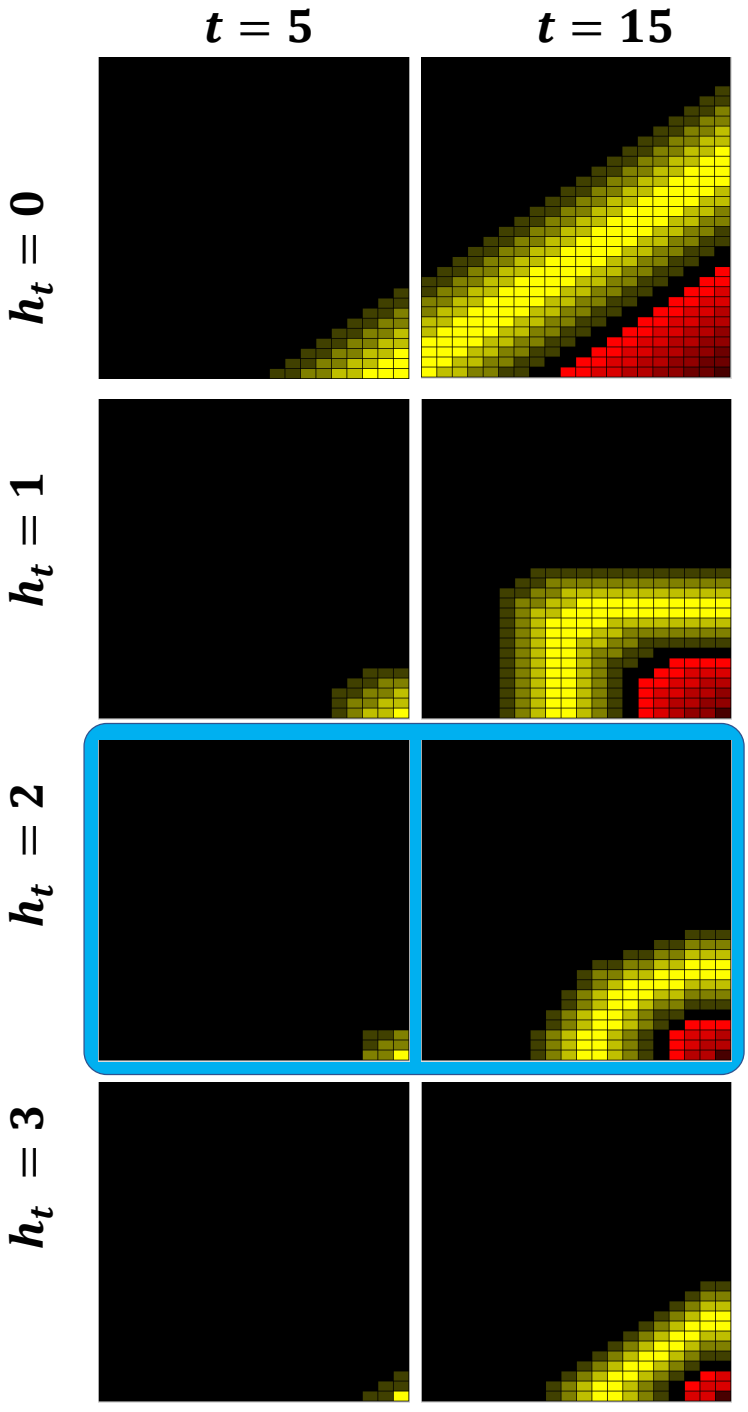

Figure 28: Corner wave simulation at $t = 5$ and $t = 25$ for different threshold values. For $y_t > 3$, the wave does not propagate. The simulation boxed in blue is the threshold used for the spiral simulations.

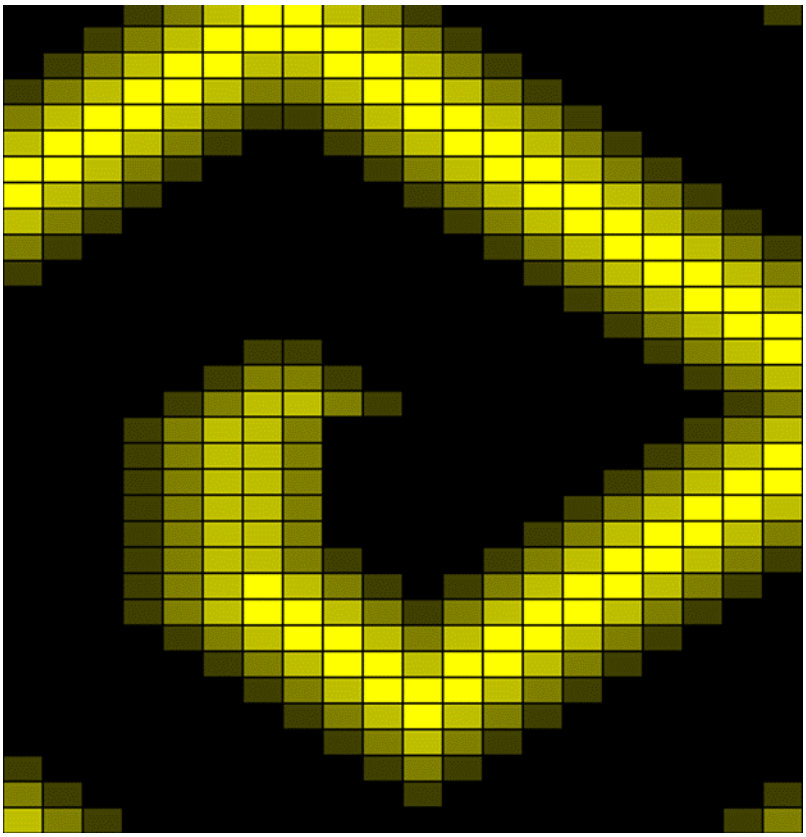

Figure 29: Simulation of a spiral wave with the number of activation steps of 4 and number of refractory steps of 7. The Manhattan size is 1, which was described by the rules given to the participants.

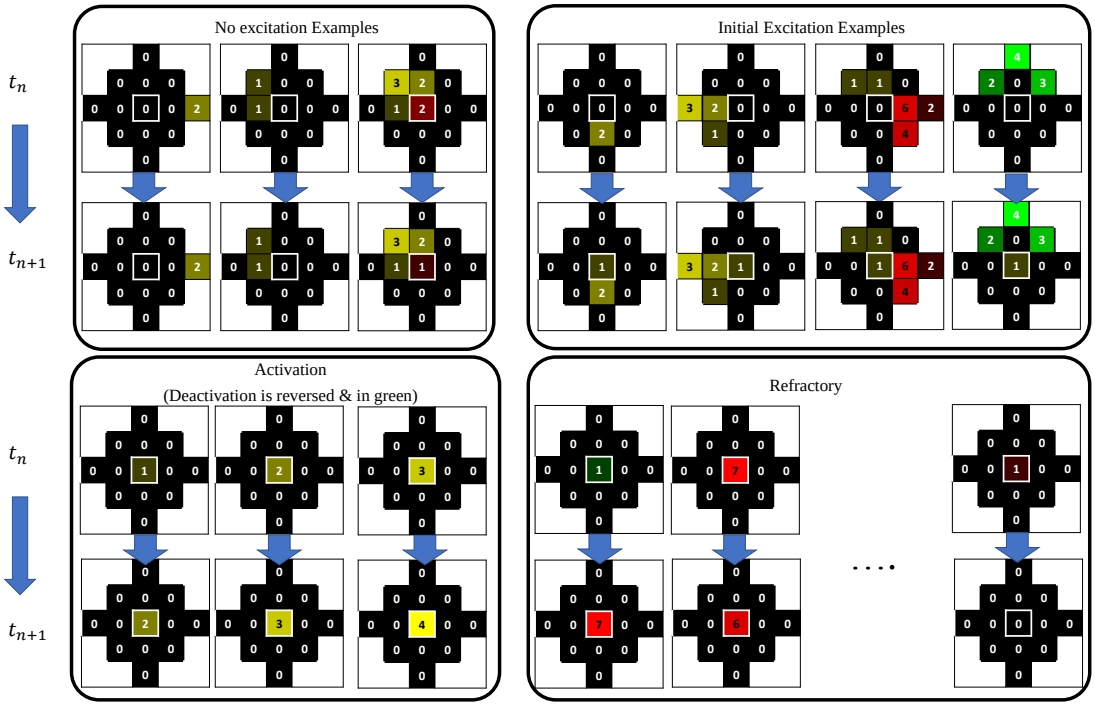

Figure 30: Activation rules for spiral wave cellular automata simulation with a von Neumann neighborhood with Manhattan size = 2. The cell of focus is the center cell in each situation with multiple examples. Rules are broken up into (i) no excitation, (ii) initial excitation, (iii) activation/deactivation, and (iv) refractory. Cells that are colored black are in rest. Cells in shades of yellow are in activation. Cells in shades of green are in deactivation. Cells in shades of red are in refractory. Note, only the center cell is being updated from t_n to t_{n+1}

rotation, given by

$$T_{rot} = \Delta t * \big(2 * n_A + (n_R + 2\big), \tag{32}$$

where Δt is the step time, $n_A \equiv$ the number of activation steps and $n_R \equiv$ the number of refractory steps.

The first 2 in this calculation comes from the number of steps activating and deactivating. The second 2 comes from the rest between deactivation and refractory and the rest at the end. What is seen is that 4 activation steps and 7 refractory steps gives the wavelength (about 7 or 8 people) and rotation period $T_r = .25*(2*4+7+2) = 4.25$ which matches experiment.

3.6.5 Spatiotemporal Disorder and Stochasticisty

Many systems that exhibit spiral waves also have been shown to lead to complex spatiotemporal dynamics when the spirals break into multiple spiral waves. There are many known mechanisms that can destabilize a spiral wave and lead to break up, with some arising from the elements coupling or heterogeneity in space ("static" mechanism), with others resulting from the intrinsic element dynamics ("dynamic" mechanism). In the experiments in crowds of people, a welcome surprise was that some of the spiral waves transitioned to complex disordered dynamics as shown in the far right of Figure 27. Breakup of the original spiral wave was driven by small variations in reaction times between participants, who excited themselves much too early, too late, or not at all, which is seen in field experiment. Those who miss the activation completely are called "dead tissue," in analogy with cells that are dead in the heart that can no longer excite. In these cases, the wave can successfully propagates through the medium, though it will affect the spread of the wave and the rotation speed. When there is a critical density of any of these types of randomness, however, the wave may break apart.

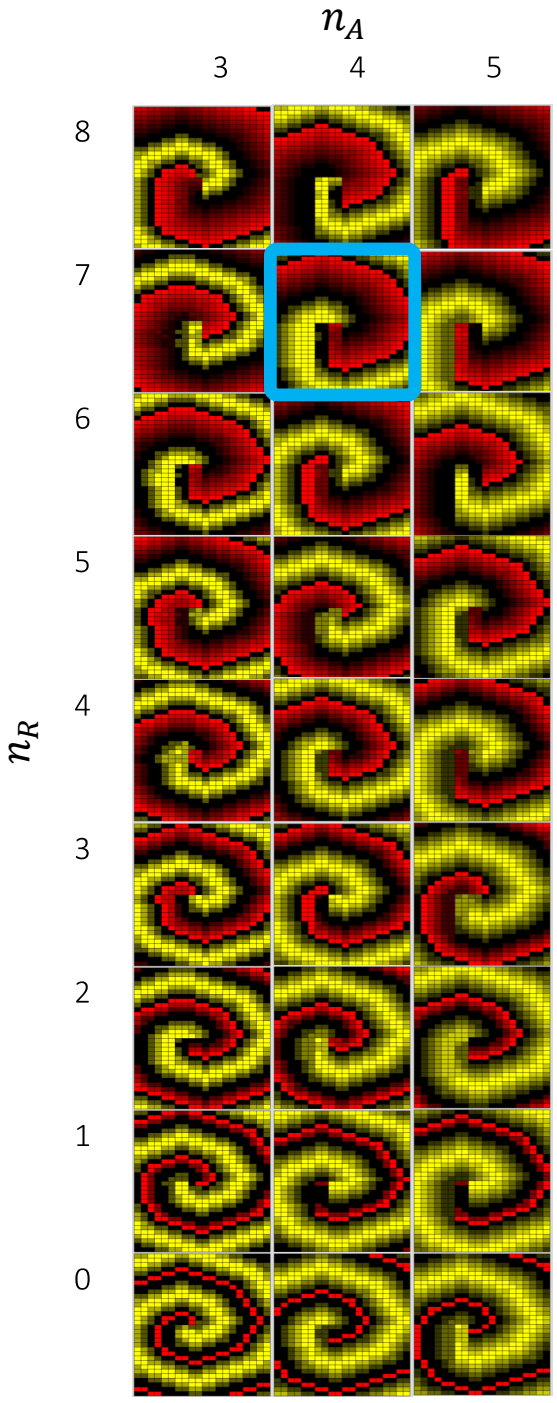

Figure 31: Set of simulations with different parameters. Yellow cells are those currently in activation. Red cells are cells currently in refractory. Both values affect the rotation period. The simulation in the blue square is the parameters that match the experiments

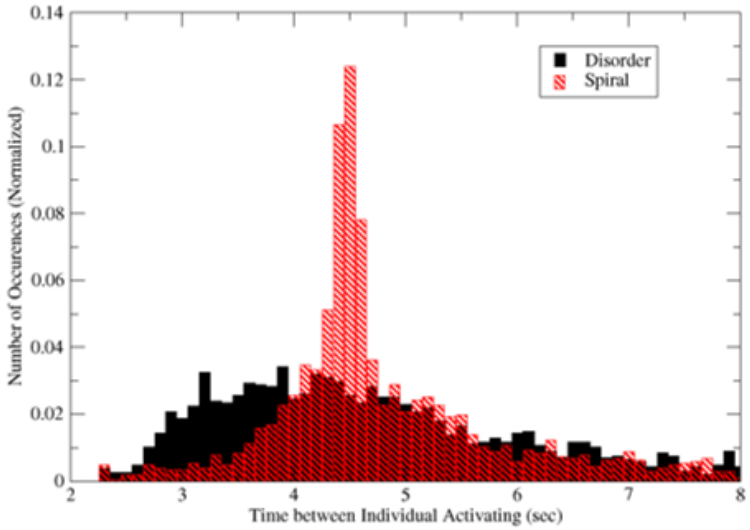

Figure 32: Histogram of experimental data of the period between each oscillation. Red shows a trial where a spiral is visible for multiple rotations. Black shows the same duration for decoherence.

For an example of a spiral wave that succeeds multiple rotations, the time between each activation is recorded in a histogram, red in Figure 32. The peak of this histogram matches the average rotation speed, 4.5 seconds. What is clear is that there is a large spread between activations, which is due to some of the randomness mentioned previously. The time between activations is also measured in the case for disorder, black in Figure 32, which shows a lack of appearance of a particularly frequency, with the activations being more spread out.

These three types of randomness can be included in the simulation for the spiral wave and the same histogram can be made to determine what may be the cause for the spiral wave break up, as well as how much of each type of randomness is needed. A parameter for the likelihood of each type of randomness is included.

- For each cell slightly outside of the Manhattan neighborhood of size 2, a cell has a probability p_{early} of activating
- For each cell that should activate, there is a probability p_{late} that it will not. The next time set it can.

- For each cell that should active, there is a probability p_{dead} that it turns into refractory and can not activate until the next time a wave is propagating towards it.

Figure 33 shows the histogram for different probabilities of each of these parameters. Each plot has the histogram for the normal wave where each of the probabilities $p_i = 0$. For the case of early activation, the histogram becomes more skewed to the left and the dominant period becomes larger. For $p_{early} > 0.50$, a spiral wave is not sustained. For the case of late activation, the histogram skews to the right and the dominant period becomes smaller. For $p_{late} < 0.50$ a spiral wave is also not sustained. For dead tissue, the histogram also becomes more skewed to the right and the dominant period becomes smaller as well; however, the spread increases more drastically, and much longer periods that were not accessible in previous simulations are accessible now. Finally, a mix of these can be studied as well and a few examples are shown in the last histogram.

Finally, we also observed a fourth individual dynamic in some of the experiments. In these cases, an individual activates when there is no wave present or oncoming, and can appear to be deliberate. These individuals are called "trolls," coined after the term used to describe a person on the internet who deliberately tries to incite discord by posting on the internet with the intent of provoking a emotional response, or excitation, from others. Trolls can also be seen in the heart–premature atrial/ventricular contractions (PAC/PVCs). These are pretty common, but people with too many often require surgery (ablation), where a cardiologist burns the hear to that spiral waves can't fit. This is called the maze procedure.

As we see with internet trolls, this can occur in small groups, and as this experiment includes individuals who volunteer, there may be cases where neighboring cells have some who excited themselves without any clear close neighbor being excited. Simulations show that only a small probability of cells being trolls, activating while

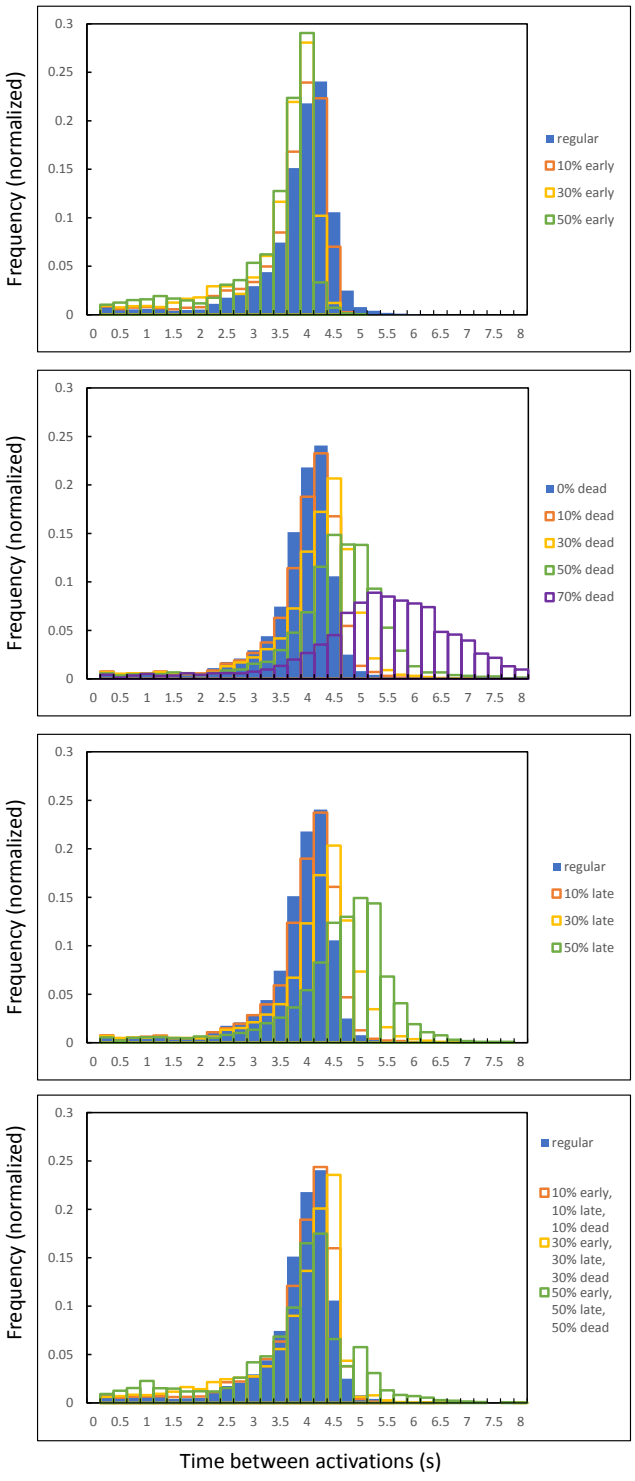

Figure 33: Histogram of simulations of the period between each activation. Blue shows the plain simulation of a spiral wave with no randomness. The different plots show how early, dead, late, and mixed activation affect the spread of the periods. These simulations were all run for 130 time steps.

in rest without any wave present, can cause spiral wave break up. At this time, we do not have an estimate in how likely this has occurred in experiment, but may be something for future study.

Of note for the probability of randomness: these simulations currently lack memory. This means that certain cells are not denoted as typically being late, early, dead or a troll. Each cell has an equal probability of activating in any of these ways, and yet the dynamics still see in agreement. For future work, and perhaps not cellular automata simulations, a possibility is giving each cell a natural frequency or a different threshold of excitability.

3.7 Discussion

The work presented here serves as an example of how a simple system, a person with a few rules, when grouped can generate new emergent behavior with spatial and temporal dynamics much more complex than that of the single element. In this case, the crowd can lead to the formation not only of waves but of spiral waves and even the development of complex spatiotemporal disorder. Furthermore, we have shown that it only requires a few single elements to destabilize a spiral wave and create irregular dynamics, which underscores the ease with which small system changes can lead to fibrillation in the heart and similar behavior in other systems.

This project originally began as a proof of concept to test whether spiral waves could be produced with a grid of people following simple rules. The short answer is: yes. At least for a short time, until certain random factors take over.

The surprising result that despite instruction to look at nearest neighbors, individuals looked further into the crowd to decide their own behavior. However, for our purposes, this was not much of an issue: the spiral was able to form and persist in most cases. In other situations, looking further into the crowd to decide their own behavior may be an issue. This may be important to consider for studies of crowd

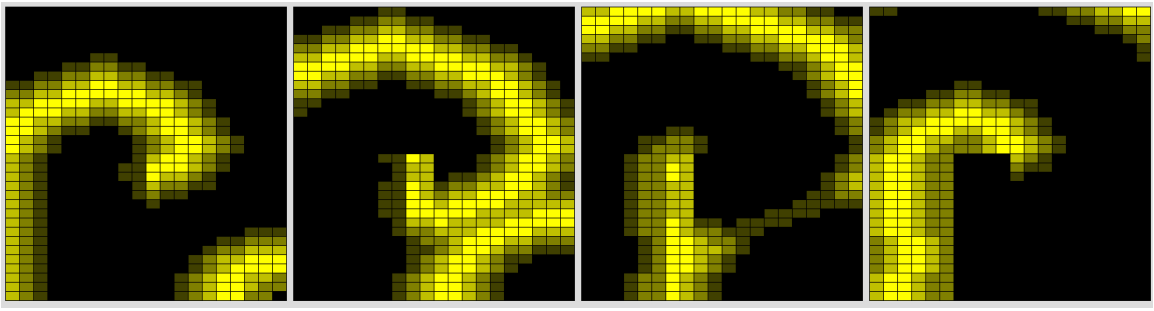

Figure 34: Simulation of the "well-intentioned physicist," (WIP). The WIP reflects a wave back toward the spiral core by activating again shortly after the initial activation. The spiral wave persists despite the reflected wave. Images taken every 5 time steps. Activation steps are hidden but still used as described earlier.

control.

Of interesting note: Mathematicians and physicists are not good subjects for this activity. Trials conducted particularly where physicists happened to be on the boundary of the system resulting in waves being reflected back towards the center of the system, despite no instruction to do so. It is of my assumption that in the mind of a physicist, if the boundary is not periodic than it must be that is a Neumann boundary where there is a zero-flux condition which will cause waves to reflect. Some of these trials led to spatio-temporal disorder. I had done one simulation with this case of individual which I dubbed the "well-intentioned physicist" where a particular physicist, or group of, was at a corner and reflecting waves. In this simulation, the spiral is stable (Figure 34) which is what was seen in the experiment.

Trials conducted at SIAM Dynamical Systems 2015 were also mostly unsuccessful for unknown reasons. Perhaps because of the experimental nature of the study. More studies are needed to determine what sort of stocasticity was added to the system to lead to this sort of disorder.

Chapter IV

PATTERN FORMATION IN *ARTEMIA FRANCISCANA*

> *This he planned of mazey wanderings that deceived the eyes, and labyrinthic passages involved. so sports the clear Maeander, in the fields of Phrygia winding doubtful; back and forth it meets itself, until the wandering stream fatigued, impedes its wearied waters' flow; from source to sea, from sea to source involved. So Daedalus contrived innumerous paths, and windings vague, so intricate that he, the architect, hardly could retrace his steps.*
>
> —Ovid, The Metamorphoses, Book 8, lines 159-168

[1]

In this section, we discuss the patterns that can be observed by the swarming of brine shrimp, specifically the Great Salt Lake strain of *Artemia franciscana*, at high concentration. These patterns can be easily observed with simple tabletop experiments; however, the cause of these patterns is unknown. We experimentally test the effects on certain physical parameters such as concentration, temperature; however more parameters may also affect pattern selection such as salinity, luminosity, light color, and the relationship of extended-area to depth. We then develop a model for the behavior of individual shrimp to set the ground work for creating a model many body-model to describe the full system. The goal of the inertial many-model is to capture the basic length and times scales of the patterns, which patterns selected, the stability of those patterns, and the transitions that occur between patterns. Future work can continue investigating these parameters to understand more deeply the interactions between shrimp and the underlying mechanism that causes the patterns to form.

[1] Translation by Brookes More

4.1 Background

Active matter systems have been studied in a variety of experimental [77–80] and theoretical [81] situations over the last few decades. Active particles can be described as anything that absorbs energy from its surroundings or has an internal energy source and depletes this energy in order to move. Much of the interest in active particles is in understanding the collection behavior of many individuals [82, 83]. Because of the energy flux involved at the level of the individuals, there is a breakdown of time reversal symmetry, which is often a characteristic of a non-equilibrium dynamic system. Large scale behavior emerges from a collective self-organization which can yield directed motion or patterns [83].

Examples of active matter systems under study span a wide variety of scales and include suspensions of swimming bacteria and colloids (micro-scale), cell suspensions, actin filaments [84], microtubules [85], bird flocks [54, 77], fish schools [54], human crowds (kilometer scale) [54], and many more [86]. Swarming depends primarily on local interactions between individuals in the swarm, whose movements are often broken up into translational and rotational components.

Aside from closing a gap in our understanding of living systems that exhibit some sort of emergent behavior, there are practical reasons for studying active matter, including applications to robotic devices, active self-assembly and crowd control. Also, after understanding different sorts of active matter systems, there may be a way to develop a unified theory of active matter or to understand if there are a few typical subclasses of collective motion patterns [83].

For the purpose of this chapter, we consider the individual shrimp as "self-propelled particles" that are near identical in terms of size, morphology, and behavior.

4.2 Active Matter

4.2.1 Passive Brownian Particles

First experiments to gain insight about random trajectories of colloidal grains suspended in water were conducted in the earliest twentieth century by Jean Perrin [87]. One key observation he made was that there were discontinuities in the trajectories of the colloids, famously thought to be impossible by Einstein [88]. This finding led to a phenomenological description posed by Paul Langevin that the motion of the colloid could be divided into two main forces: (i) a mean drag force $-\zeta\vec{v}$ which acted in opposition to the displacement of the colloid in the fluid, where ζ denotes the friction coefficient, and (ii) a random force $(2B)^{1/2}\vec{\xi}$ describing the effect of collisions by solvents atoms that drive the colloid motion, where ξ is the force due to random collisions with other particles and B is the amplitude of the noise. Newton's second law for these particles is then given by the stochastic differential equation,

$$m\dot{\vec{v}} = -\nabla U - \zeta\vec{v} + (2B)^{1/2}\vec{\xi} \tag{33}$$

where m is the mass of the particle under the potential U. The random force ξ has correlations $\langle\xi_a(t)\xi_b(0)\rangle = \delta_{ab}\delta(t)$ meaning that at different times, there is no correlation between the noise caused by the collisions with molecules of the fluid, which is a property of Gaussian white noise. These fluctuations happen on microscopically short time scales and also the collisions do not contribute to any overall net force meaning $\langle\xi(t)\rangle = 0$ [89]. This is the Langevin equation that is used to describe the time dynamics of a passive Brownian particle (PBP). If we consider the particles without the potential, we can find the average velocity squared at a given time t as follows,

$$\left\langle [v(t)]^2 \right\rangle = \frac{dB}{m\zeta}(1 - e^{-2|t|/\tau_m}). \tag{34}$$

Here, d is the spatial dimension of the system. More importantly, we have a time scale $\tau_m = m/\zeta$ which gives us information about the inertial time scale which is the time at which the effects of friction on the particle over take the effects of the inertia of the particle.

When $t >> \tau_m$, the equipartition theorem relates the fluctuations of the velocity via temperature T of the solvent as $\langle v^2 \rangle = d(T/m)$ (Boltzmann constant is set to 1). Therefore, the amplitude of the noise is $B = \zeta T$ and the mean-squared displacement (MSD) which describes how the individuals deviate from their original position over time is given by,

$$\begin{aligned} \left\langle \Delta r^2(t) \right\rangle &= 2d\frac{T}{\zeta}\left[|t| - \tau_m(1 - e^{-|t|/\tau_m})\right] \\ &= \begin{cases} d\frac{T}{\zeta}\frac{t^2}{\tau_m} & \text{for } t << \tau_m \\ 2d\frac{T}{\zeta}|t| & \text{for } t >> \tau_m. \end{cases} \end{aligned} \tag{35}$$

This says that at short time scales the particle is ballistic where $\langle r^2 \rangle \propto t^2$ in nature, but at large time scales it is diffusive where $\langle r^2 \rangle \propto t$. We can also get a relationship for our translational diffusion constant, yielding $D_t = \lim_{t\to\infty} \langle \Delta r^2(t) \rangle / (2dt) = T/\zeta$ via the Einstein relation, namely $D = \mu T$, with $\mu = v_d/F$ the mobility of the particle's drift velocity.

4.2.2 Self-propelled particles

Now, we will begin to describe how the physics of PBP relate to those of particles that have an internal energy source causing themselves to propel through the fluid. To do this, we add in a term to our Newton's second law force balance, Eq. (33), namely a sustained energy source that embodies the microscopic conversion of energy stored in the environment into a directed motion of the particle. Here, inertial effects are ignored and the particles thus experience zero net force, so that the damping force, the self-propulsion, are all in balance. The force balance is between the damping

force $-\zeta r$, the self-propulsion u, and forces deriving from a potential $-\nabla U$ yielding an equation as follows:

$$\dot{r} = u - \mu_t \nabla U + (2Dt)^{1/2}\xi. \tag{36}$$

Here, $\mu_t = \zeta^{-1}$ is the translational motility, which is inversely proportional to the drag coefficient. As the fluid has less drag on the particles (i.e. $\zeta \to 0$), the particles can move more easily and the forces due to the potential are maximized (conversely, as the fluid has more drag on the particles (i.e. $\mu_t \to 0$), the particles cannot move as easily, and the forces due to the potential are minimized).

To find how well a particle's orientation given by a vector $\vec{u}(t)$ stays constant during a typical persistent time τ, we assume that the correlations between the direction of motion of a particle decay exponentially in time so that the particle holds no memory of much earlier times:

$$\langle u_\alpha(t) u_\beta(0)\rangle = \delta_{\alpha\beta}\frac{v_0^2}{d} e^{-|t|/\tau}. \tag{37}$$

There are a few main models whose statistics different include higher order terms inspired by various biological systems: run-and-tumble particles (RTPs), active Brownian particles (ABPs), and active Ornstein-Uhlenbeck particles (AOUPs).

Run-and-Tumble particle is the first of a limiting model of stochastic dynamics that is relevant to the shrimp. For this, particle motion consists of persistent swimming motion in straight lines called "runs" followed by sudden changes of direction called "tumbles" [83, 90–92]. Particles move at fixed speeds v with tumbles occurring at fixed rate α, each which decorrelates the swimming direction. This motion is of a diffusive random walk at times scales larger than α^{-1} and length scales larger than $\ell = v/\alpha$. For d dimensions, the diffusivity is given as $D = v^2/\alpha d$ [92].

We choose to focus on the ABPs.

4.2.3 ABP statistics

Originally introduced to mimic the dynamics of self-phoretic colloids with asymmetric chemical and/or physical properties [89, 93], the dynamics are broken down into periods of motion of fixed speed v_0 with a diffusive process controlling the direction of motion. This rotational diffusion is what causes the direction to decorrelate over time [92]. For a two dimensional system, the self-propulsion term which is included in Eq. (33) is written as $u = v_0(\cos\theta, \sin\theta)$ where the rate of change of the angle is given by:

$$\dot{\theta} = (2D_r)^{1/2}\eta \tag{38}$$

with an angular diffusivity D_r and the Gaussian noise term $\langle \eta(t)\eta(0)\rangle = \delta(t)$.

It has been shown [94] that the calculations of the large-scale diffusivity D can be generalized as a superposition of those for both RTP and ABP dynamic, resulting in a modified diffusion constant given by

$$\begin{aligned} D &= \frac{v^2}{\alpha d} + \frac{v^2}{d(d-1)D_r} \\ &= \frac{v^2}{d}\left(\frac{1}{\alpha} + \frac{1}{(d+1)D_r)}\right) \\ &= \frac{v^2}{d}\tau, \end{aligned} \tag{39}$$

where $\tau^{-1} = \alpha + (d-1)D_r$ is the relaxation time of the particle.

4.3 Bioconvection

A key phenomenon that relates to this experiment is that of light-induced bioconvection. Bioconvection patterns are often observed in laboratory experiments of shallow suspensions of randomly swimming micro-organisms. The first detailed observations of this phenomenon were recorded in 1911 by Wager [95], but it is noted that it could

have been observed as early as 1848. This is due to the micro-organism being slightly denser than that of the fluid they are in, and their natural tendency to swim upward on average against gravity (negative gyrotaxis) [96–98]. These patterns have also been observed in natural habitats of micropatches of zooplankton [99]. The scope of this thesis does not cover the mechanisms behind the upward swimming of the shrimp but the effects of the collective motion.

The basic mechanism of bioconvection is analogous to that of a Rayleigh-Bénard convection where a temperature gradient δT between the top and bottom of a container of fluid causes small parcels of fluid near the bottom to expand and decrease in density making them more buoyant than surrounding fluid causing it to rise, while parcels of fluid near the top will cool and contract in volume causing them to increase in density and begin to fall to the bottom as illustrated in Figure 35. In the case of bioconvection, the tendency of the organisms to swim upward causes the average density at the top of the suspension to be greater than that on the bottom. This sort of stratification with a denser upper layer and the continuous push for other micro-organisms to push toward the top causes an instability if the gradient is large enough, causing pockets of the organisms to fall and form convection cells [96]. Figure 36 shows a schematic of this process.

Experiments have been studied involving alga *Chlamydomonas nivalis* and soil bacterium *B. subtilis* [97, 98]. Of note is that these organisms are $1 - 10\mu$m in size and their motion occurs at low Reynolds number. Particularly, for the *Chlamydomonas nivalis*, work has been done to study the wavelengths of the patterns formed by bioconvection. Bees and Hill [97] show that the unstable wavenumber of these patterns are a function of time, cell concentration, and suspension depth. *C. nivalis* are gravitactic (i.e. directional movement in response to gravity), gyrotactic (i.e. directional movement in response to combination of gravitational and viscous torques in a flow), and phototactic (i.e. direction movement in response to light) which also

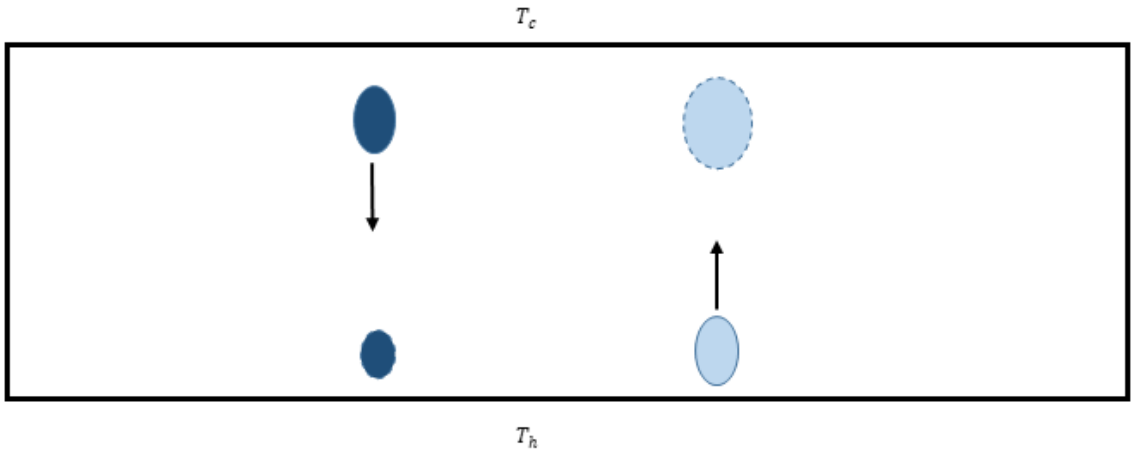

Figure 35: Rayleigh-Bénard convection schematic. The bottom is kept at a constant temperature $T_h > T_c$ which is controlled on the top. The small parcels of fluid are assumed small enough such that the temperature is uniform throughout the parcel. When the temperature gradient $\delta T > T_h - T_c$ is greater than a critical temperature T_{crit}, the buoyancy forces overcome the friction force from the fluid viscosity and the parcels will rise and fall.

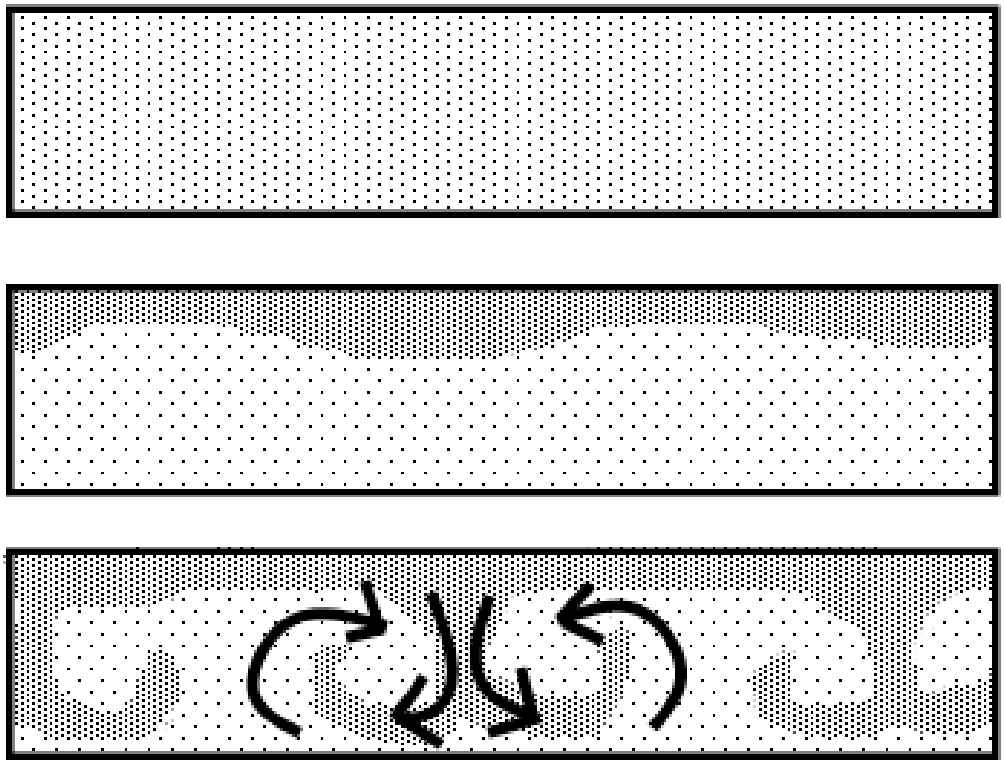

Figure 36: Schematic of bioconvection of suspensions in a shallow container. The dots show relative densities of different parts of the fluid. Gravity is pointed downward. The top shows a well-mixed system of density ρ_0. The middle shows that the system splits as organisms swim upward and cause the suspension to stratify with a denser fluid ($\rho_>$) on the top and less dense fluid ($\rho_<$) on the bottom. The denser fluid begins to fall as lower organisms in less dense fluid push up causing an instabilty at the interface of the two densities. Convection cells to form creating a pattern when viewed from above.

contribute to their motion.

Fourier analysis of images of these bioconvection patterns showed the most unstable wavelength and how it depended on cell density and the depth of the suspension. Wavenumber, the number of complete sinusoidal waves in a certain length, was defined as,

$$k = \frac{I_W}{\lambda} \tag{40}$$

where λ is the physical wavelength and I_W is the image width. The image of the sample can then be transformed from physical space to Fourier space via a Fast Fourier Transform (FFT) [100]. The discrete Fourier transform, $H(k_x, k_y)$, of image $h(x, y)$ of size N^2 for a two dimensional system is given by

$$H(k_x.k_y) = \sum_{x,y=0}^{N-1} exp\big(\frac{2\pi i k_x x}{N}\big) exp\big(\frac{2\pi i k_y y}{N}\big) h(x, y), \tag{41}$$

with k_x and k_y the wavenumbers. Particularly, the wavelength of patterns that emerged increased with suspension depth but decreased with concentration [97]. These patterns can occur at depths of about 5. These experiments had pictures of the suspensions taken every 10 seconds with a concentration of 1.89×10^6 cells/cm. Images in [97] show a petri dish which begins as a uniform color and aggregations form over time. By 20 seconds after the start of the experiment, dark areas begin to form where there is a high local concentration. These dark areas begin as a labyrinth like pattern which becomes more apparent 30 seconds after the start of the experiment. By 50 seconds, the pattern separates into about 100 dark circular spots. These spots remain in their locations but will deform.

Often, the interactions between individuals in these systems can be classified can either be simple (attraction/repulsion) or more complex (combinations of simple interactions) [101]. Mainly, the interaction between individuals is affected by that of

neighbors, either those in space or those connected by some underlying network, causing the individuals to behave differently than they would if isolated. Different models to describe collective motion of animals have been studied over the years. Reynolds first proposed a computational model of "boids" that was used to describe bird flocks and schools of fish [102].

This behavior is often important in biological functions of the individuals depending on the species but often include foraging, mating, anti-predation and migration. While there are many types of models for some of these swarming patterns, the behavior is still not completely understood [77].

We focus on *A. franciscana*, a type of zooplanketon which has other aspects that come into their swarming patterns besides those mentioned above. Many types of zooplanketon's migration patterns are affected by light and food. Aggregation also serves to reduce vulnerability to predation related to the number of individuals [103], their density [104–106], and the uniformity of the group [107].

4.3.1 Biology of *Artemia franciscana*

During their life cycle, *Artemia franciscana* go through about 17 molts, called instar stages, where their bodies drastically change in size and shape [108]. These instar stages from hatching to adulthood can be seen in [109]. *Artemia* change through instar stages in a matter of hours to days depending on surrounding environment. After hatching, the first instar *Artemia*, called nauplius larvae, are about $0.4 - 0.5$ mm in length and orange-brown in color. At this stage, their bodies consist of a head with one nauplius eye, which is common for first larval stages of crustaceans, and appendages: a pair of antennae, a pair of second antennae and a pair of mandibles [108]. Their swimming involves a stroke from their appendages that shifts their body back before propelling itself forward. This process can be seen in Figure 37 where a nauplius is undergoing about 1.5 strokes.

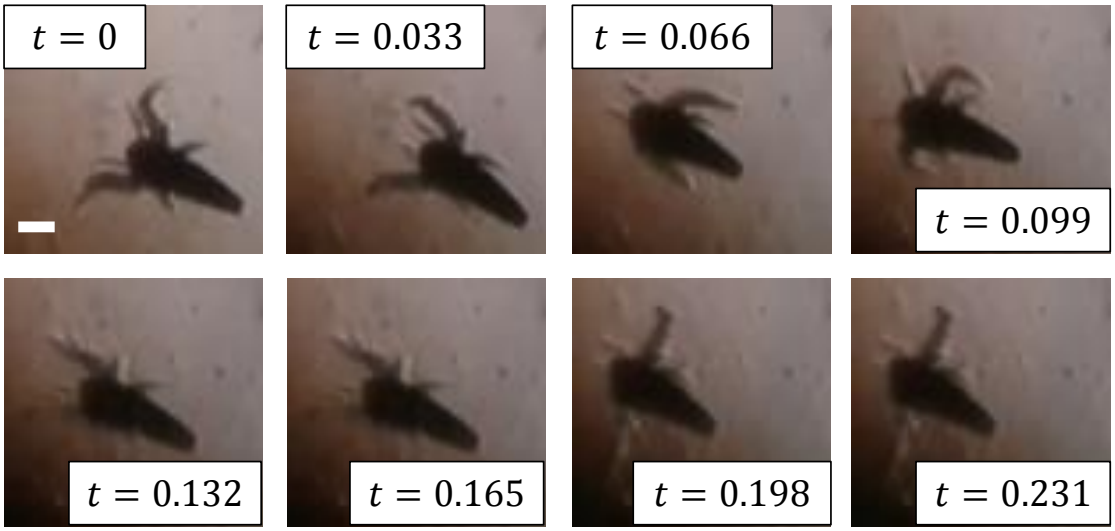

Figure 37: Images of nauplius swimming under microscope taken at $t = 0.033$ second intervals with fixed field of view. The white bar in the first image is 0.1 mm. Between $t = 0$ s and $t = 0.033$ s, the nauplius can be seen moving backwards during the stroke before pushing forward in $t = 0.066$ s. This same process is seen between $t = 0.099$ and 0.132 s.

The nauplius does not feed or mate at this stage [108, 110]. The nauplius will swim for $12 - 20$ hours, depending on temperature, before molting to the second instar, metanauplius larva. In this instar, individuals are about 0.6 mm in length and translucent in color. Because mating and feeding are both events that can affect swarming, and because the *Artemia* can grow up to 10 times larger than their original size with a very different morphology, 1st and 2nd instar stages are focused on for this project.

Artemia are known to swarm and this is attributed to protection of ingestion by predator species, reproduction, or foraging [111]. There are various parameters that are believed to affect the swarming of *Artemia*: density, age, feeding, and salinity of the surrounding water [110]. Also, *Artemia* are positively phototactic, meaning that they attracted to light [112], especially at a young age. Swarming for *Artemia* is thought to occur only if the density of *Artemia* in water is higher than a critical

density [111].

Experiments have been conducted removing parts of a swarm in successive steps until a swam no longer forms again after waiting 2 hours resulting in a critical density required for swarms. This critical density depends on the different ages of the overall sample of *Artemia* and results for a few different ages. These experiments show that the critical density at 1 day is $\approx$ 1250 *Artemia*/L, at 3 days is $\approx$ 4000 *Artemia*/L, at 6 days is $\approx$ 4500 *Artemia*/L, and at 10 days is $\approx$ 500 *Artemia*/L [110]. When the number of shrimp is less than the critical density, the shrimp swim throughout the volume of the container without

Light also plays a major role in the formation of observed swarms under three different light conditions in an aquarium of 24 L of dimensions $40 \times 20 \times 30$ cm at room temperature $19 - 20°C$. Other studies by Gulbrandsen showed that second and third instar of the *A. franciscana* exhibited dense and coherent spherical swarms about $2 - 5$ cm in diameter as either a single swarm or three linked together in a triangle when left with submerged light. These spherical swarms appeared in a vertical plane of the aquarium and the experiments do not quantify the total density of these swarms or the salinity of the water that these swarms are in. For studies under an overhead light, the *Artemia* make a "T-shaped" swarm where they swim down, loop back up approaching the water surface at an acute angle, swim parallel to the surface towards the center, and back down. This pattern can last an entire day and toggling the light would cause the pattern to break up and reappear. Also in this light condition, spherical swarms as described in the previous situation would also appear in the plane of the water's surface. Finally, when in a condition of indirect sunlight, the swarms would form spiraling streaks along the surface of the water– these did not last very long like the previous swarms [110]. Of interest to the experiments in these thesis, is the second light experiment discussed above.

Experiments on the effect of salinity level for *Artemia* swarms showed were also

conducted for salinities from 5 to 300 ppt. For these experiments, direct overhead light was used. Higher salinities (above 100 ppt) resulted in erratic swarmers forming one large clump in the center of the aquarium. From the side of the aquarium, these shrimp would stay at the top of the aquarium. Lower salinity levels around $30 - 50$ ppt yielded patches through out the surface of the water. Observations from the side of the aquarium showed that shrimp in the swarm followed loop trajectories, called "butterfly" swarms which look similar to convection cells. Experiments at a salinity of 5 ppt show that shrimp will swim random trajectories. Images of these trajectories and swarming patterns can be seen in [110], Figure 8.

Some of these patterns are of particular interest to this project and the trajectories of swarmers at 30 ppt salinity appear to be like those in convection currents. As the salinity changes the density of the sample, this may affect the wavelengths that appear in bioconvection due to the change in the viscosity of the water.

4.3.2 Dynamics of *Artemia* Swarms

One active model of *Artemia* is assuming their behavior is like that of self-propelled particles which depends on the relative distance between individuals as well as between individuals and external factors. Under uniform light, *Artemia* will swim in random direction performing obstacle avoidance [113, 114].

In 2011, experimental and theoretical studies by Ali, Fortuna, Frasca, Rashid and Xibilia studied the effects of different wavelengths on *Artemia* motion [113]. One of their findings shows that *Artemia salina* are most responsive to higher frequency lights (blue) while least responsive to lower frequency lights (red). They used a model derived from Newton's equations which takes previous models for swarming and adds in the attraction of the *Artemia* towards light. This model is given by

$$m\frac{d\vec{v}_i}{dt} = a\vec{n}_i - \gamma\vec{v}_i + \sum_{i\neq j} a_{ij}\vec{f}_{ij} + \vec{g}_i \tag{42}$$

where m is the mass of the *Artemia*, $\vec{v_i}$ is the velocity of the ith individual, $\vec{f_i}j$ is a locomotion force in the $\vec{n_i}$ direction which is given by the Vicsek model, γ is a resistivity coefficient for the medium acting on the individuals, a_{ij} is a term of the adjacency matrix which describes how strong the coupling is between the ith and jth individuals. This can be compared to Equation (33) where the potential U is related to $\sum_{i\neq j} a_{ij}\vec{f_{ij}} + \vec{g_i} = -\nabla U$. Here, $\vec{g_i}$ is the attractive force towards the light given by,

$$\vec{g_i} = C_g K_{v_i} K_{r_i} \frac{\vec{r_a} - \vec{r_i}}{|r_a - r_i|}, \tag{43}$$

with K_{v_i} and K_{r_i} the speed and sensitivity coefficients respectively. Also $\vec{f_{ij}}$ is a short-range interaction force between the ith and jth individuals given by

$$\vec{f_{ij}} = -c\left[\left|\frac{\vec{r_c}}{|\vec{r_a} - \vec{r_i}|}\right|^3 - \left|\frac{\vec{r_c}}{|\vec{r_a} - \vec{r_i}|}\right|^2\right]\left(\frac{\vec{r_j} - \vec{r_i}}{|\vec{r_a} - \vec{r_i}|}\right). \tag{44}$$

The short-range interaction force is such because within a critical distance r_c, the *Artemia* perform obstacle avoidance while outside of the same distance, they are attracted to the school orienting themselves along the other individuals. Within this critical radius, *Artemia* do not perform other behavior because repulsion dominates completely when two are in close range of each other [114]. The authors acknowledge that an issue with this method is that the parameters γ, a, C_g, K_{v_i}, and K_{r_i} are difficult to determine.

While this captures the dynamics of small number of *Artemia* in a large container, this does not produce the patterns that are seen in experiments for shallow suspensions This also ignores the tendency for shrimp to swim upward and may not describe dynamics well at higher concentrations. We begin by experimenting on individuals to understand their long term statistics and lay groundwork for a many-body model which can lead to global patterns like those observed.

4.4 Experiments and Simulations

We have found that *Artemia franciscana* will form spatially interesting swarming patterns in shallow suspensions of salt water at the age of 1 day. At this point, they are too young for these swarming patterns to be caused by mating [115]. As there are no intra-swarm collective behavior, it is thought that these patterns are not due to feeding either [110]. It is also thought that these patterns are not due to anti-predator behavior [111]; therefore we investigate more deeply the environmental factors that affect the swimming trajectories of the shrimp to determine why spatial patterns form. To do this we first hatch shrimp in a laboratory setting.

4.4.1 Hatching shrimp

Artemia franciscana Great Salt Lake strain begin as dried cysts which can remain at low temperature until ready to use. Before hatching, the cysts go through a decapsulation process to remove the hard shell that encapsulates the embryos. This process involves: (i) hydrate the cysts in fresh water with aeration for two hours, (ii) add 150 mL of sodium hypochlorite and wait for cysts to change to orange (approximately 7 minutes), (iii) drain cysts in 125μm mesh sieve and rinse thoroughly, and finally, (iv) drain and cysts that are not used promptly can be stored by adding 300 ppt saltwater and placed back in low temperature. The brine shrimp were cultured in a hatching cone by adding 1 gram/L of *Artemia* cysts to 1 L water at 25 ± 0.5 ppt, with aeration, temperature controlled at $26 - 28^{\circ}$C, and under constant light.

Experiments were conducted $18 - 36$ hours after hatch setup. *Artemia* take ≈ 18 hours to hatch into nauplii (instar I) and will quickly molt into instar II [108]. When preparing experiments, nauplii are harvested by removing the aerator and waiting for the shrimp and shells to separate. Nauplii will either settle to the bottom or swim towards a light while the shells will rise to the top and float. The nauplii are then siphoned with an airtube into a 125 μm mesh sieve and rinsed with fresh water.

Shrimp are then measured out by mass into a petri dish of 8 cm diameter and 25 ppt saltwater is added at different volumes.

Shrimp are now ready for experiments. First we discuss the collective behavior experiments that result in the patterns observed and then we study the individual dynamics in order to ascertain how environmental factors can affect the individual dynamics of the shrimp.

4.4.2 Swarming of Shrimp Aggregations

When higher densities of *Artemia* are left in a container, aggregations form which will appear as spatial patterns along the surface of the area of the sample. There are many environmental conditions that affect these patterns. These spatial patterns do not form when the sample is left in the dark, yet the same sample will develop patterns once placed in direct or indirect light. These patterns are also not seen for dead or unhatched *Artemia* or older *Artemia* under the same external conditions leading us to believe that the patterns are driven by the motion of the living *Artemia* themselves and their phototaxis. The age of a sample of *Artemia* is checked under the microscope before experiments where their size are measured their morphology is confirmed.

Shrimp are collected from their hatching container and any residual eggs, which sink towards the bottom of the container, are removed from the sample by pipette. Water is drained from the shrimp collection using a 125 μm mesh sieve. A petri dish is placed on a scale which is tarred. Drained shrimp are scooped into the petri dish weighing 10 g. Then, 20 g freshly prepared saltwater at 25 ppt is added to the sample. The sample is then allowed to sit for a few seconds under a light and the sample will start swarming producing spatially extended patterns.

4.4.2.1 Light Experiments

A light is placed at 50 cm above a petri dish filled with the shrimp-water mixture. Once a spatial pattern develops in the petri dish, the light is turned off and the sample is left in complete darkness. After waiting 10 minutes, the light is turned back on and the distribution of shrimp is observed in the petri dish and recorded. Distribution appears uniform, but within 1 minute aggregations begin to form again. Closer inspection shows that the shrimp begin swimming towards the top of the sample along the water's surface before the patterns begin to form.

Similarly, a light is placed 50 cm below the petri dish with the same sample of shrimp. After waiting more than 5 minutes, patterns do not form and the distribution appears uniform. Closer inspection shows that many of the shrimp swim down toward the bottom of the petri forming a uniform layer along the bottom of the container.

4.4.2.2 Density Experiments

For these experiments, three LED panels surround the sample and are angled down to light the sample uniformly, which is shown in Figure 38. The camera is placed directly above the sample and a videos were recorded at 60 fps. Samples are well mixed with a stirrer, but swirling the sample to mix has not shown to produce different patterns.

After recording for 10 minutes, the sample is mixed and allowed to settle again and another recording is made. Salt water is added again, the sample was weighed and mixed, and another trial was recorded. This was done multiple times until patterns seemed to no longer appear.

4.4.2.3 Analysis of Patterns

Patterns that have been observed fall into two categories: (i) long wavelength patterns where boundaries play a strong effect on the patterns that form (Figure 39) and (ii) short wavelength patterns that may or may not span the entire extended area of the

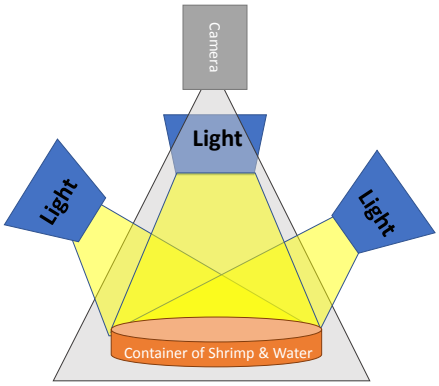

Figure 38: Schematic of experimental setup for collective motion experiments. Three LED lights are placed around the sample and angled down to reduce preference in light direction. A measuring stick is also in view for calibration during tracking.

sample (Figure 41). The long wavelength patterns are reminiscent of those observed in [110] for different salinities, however salinity in these experiments remain constant.

For the concentration experiments, images taken after 5 minutes were converted to gray-scale and processed by measuring the diameters of the larger aggregations. Images showing six different concentrations of shrimp by percentage are shown in Figure 40. At 30% concentration of shrimp, small aggregations form throughout the sample. As the the concentration of shrimp decreases, the average size of these aggregates becomes larger meaning that the overall wavelength of the sample increases.

Also studied are the development of these patterns. Figure 41 shows a sample of 15 mL of shrimp and water mixture left to sit for patterns to start to form. The first row of images show the development of a short wavelength or "labyrinthine" pattern which becomes clear 7s after mixing stops. At $t = 10$s, the system is perturbed by a jerky action to the petri dish causing the water to slosh back and forth. However, the pattern that was originally developed appears stable.

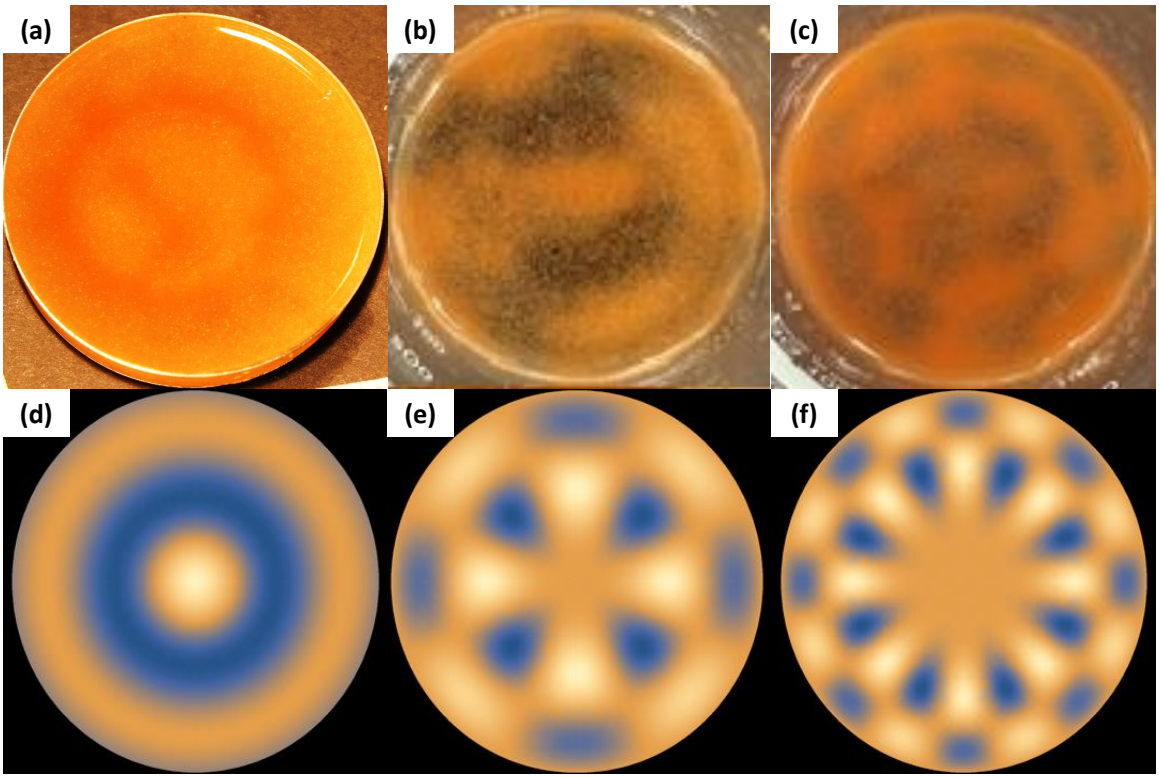

Figure 39: Above, three examples of patterns that have formed from aggregations of shrimp. Beneath, images are plots of the cylindrical harmonics resembling the above patterns. Particularly, (d) is the $n = 0$ and $k_r = j_{0,3}$ mode, (e) is the $n = 4$ and $k_r = j_{0,2}$ mode and (f) is the $n = 8$ and $k_r = j_{0,2}$ mode.

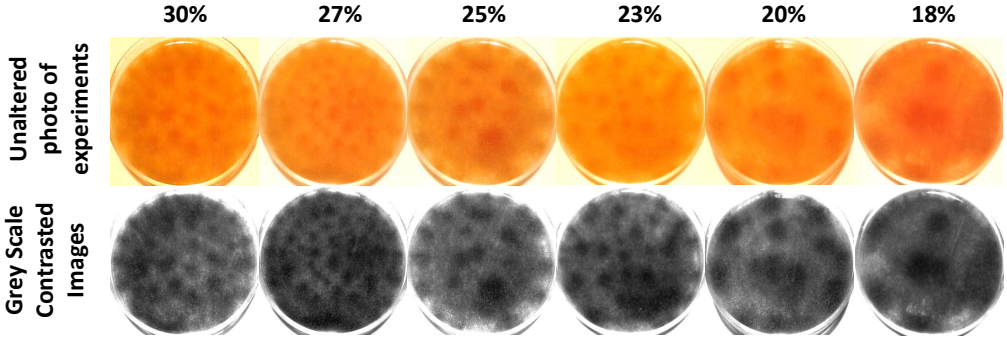

Figure 40: Images of shrimp aggregation experiments taken at six different concentrations in both original and gray-scale. Concentration is calculated by the percentage of shrimp of the sample by mass.

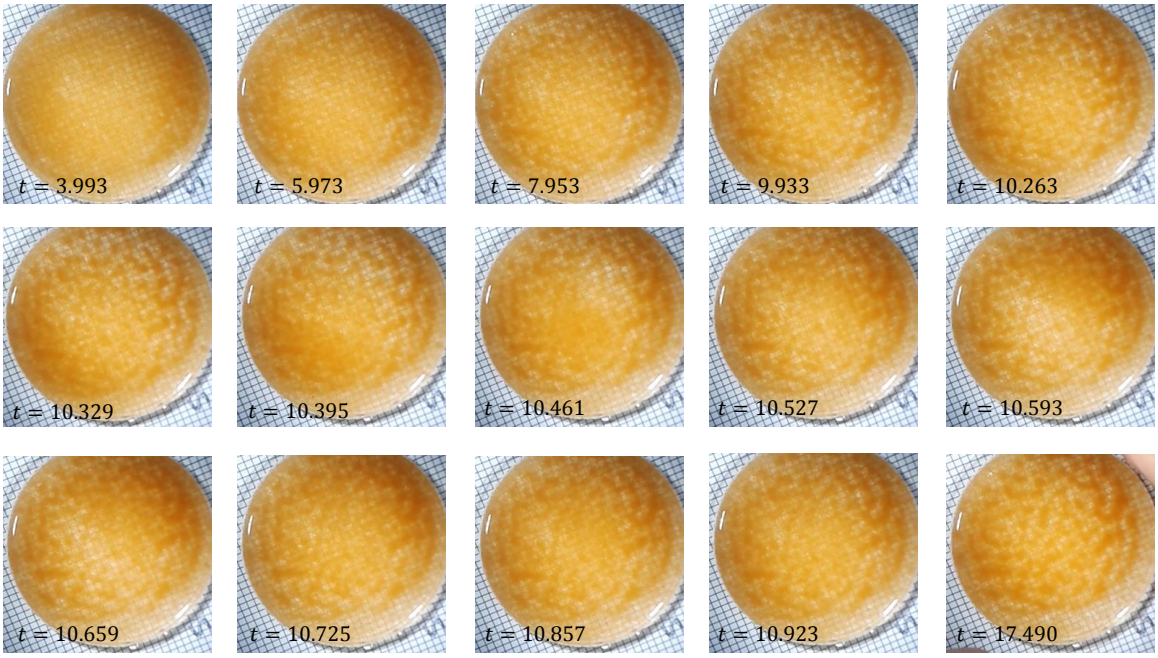

Figure 41: 15 mL of shrimp and water in a 8 cm diameter petri dish. Time (in seconds) starts as soon as mixing ends. Between the top and middle rows, the paper under the sample is pulled perturbing the sample making the water slosh back and froth between the lower left and the upper right of the sample.

4.4.3 Individual dynamics

4.4.3.1 Shrimp as Self-propelled particles

Experiments were conducted to determine how temperature and light affect the dynamics of individual shrimp. A petri dish of approximately 30 nauplii and 30 mL saltwater is place under the Canon EOS 60D camera with light as shown in Figure 42. The setup changes slightly for the collective study experiments.

Individual Shrimp Experiment: One overhead lamp placed directly above the petri dish and one camera placed at an angle from the normal of the samples surface.

A ruler is placed outside of the petri dish flat in the field of view to calibrate the size of the experiment. To control the temperature of the sample, the petri dish was placed in a bath of water of different temperatures until the sample reached equilibrium. Videos were then recorded for 3 minutes and the trajectories of the shrimp were tracked using Tyson Hedrick's VLTdv5 MATLAB tracking program [75].

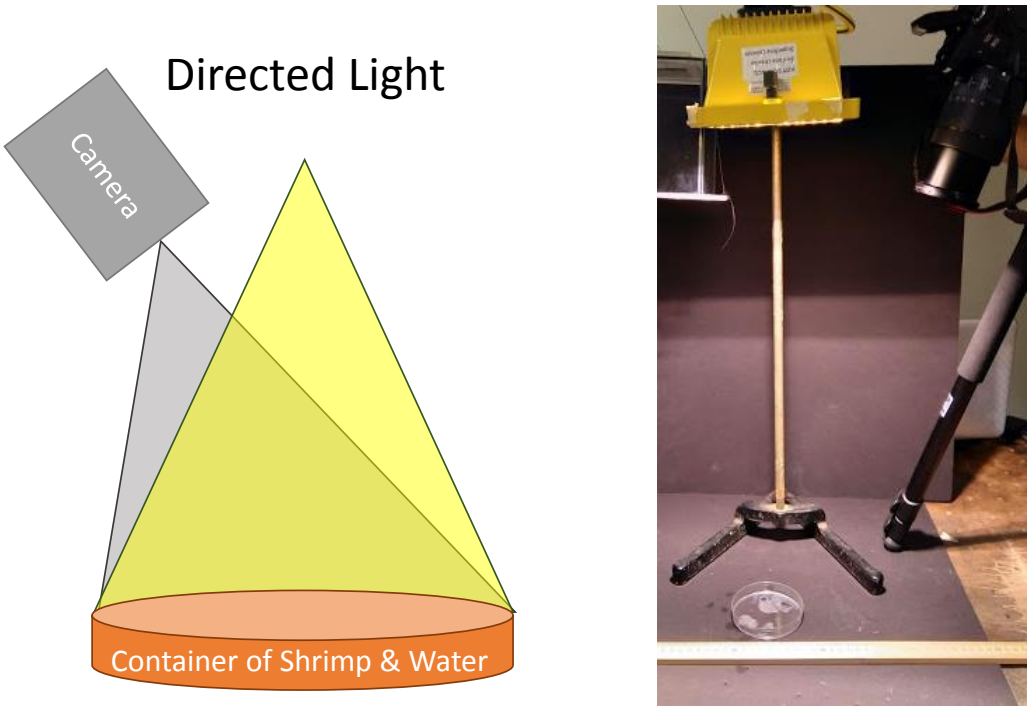

Figure 42: Left: Schematic of experimental setup for tracking individual shrimp. The light is overhead and the camera is off center angled to view the petri dish of shrimp. Right: Photo of the same setup. A measuring stick is also in view for calibration during tracking. For temperature experiments, the petri dish is put inside a wider container filled with water at a certain temperature.

4.4.3.2 Single Shrimp Statistics

After tracking the shrimp, the positions from the tracking program are converted from pixels to centimeters and the mean squared displacement (MSD) discussed in section 4.2.1, here taken as ensemble average over different shrimp, can be calculated as a function of time,

$$\langle r^2(t)\rangle = \frac{1}{N}\sum_{i=1}^{N}(r_i(t) - r_i(t=0))^2. \tag{45}$$

This describes how shrimp move from their initial position after a period of time. In section 4.2.1, the MSD is shown to take the form of power law relationship with time such as

$$\left\langle \Delta r^2(t)\right\rangle \sim \begin{cases} A_1 t^{\alpha} & \text{for } t << \tau \\ A_2 t^{\beta} & \text{for } t >> \tau, \end{cases} \tag{46}$$

with $\alpha = 2$ and $\beta = 1$. A detailed description of the fit process and values for the data sets is found in Appendix B.

The MSD is found to depend on temperature which can cause the shrimp to speed up or slow down. The inserts in Figure 43 show how the data is fit in three different sections: the ballistic section at short time scale, the diffusion section at medium time scale, and the last section where the MSD begins to approach a constant. This last section is due to the boundary of the petri container which happens at $\langle \Delta r^2(t)\rangle \approx a^2$, where a is the radius of the petri dish.

The persistence time τ, the time it takes for the shrimp to turn, can be found by finding where the t^2 region and the t region intersect. A list of these values for each temperatures is found in Table 1. What is found is that the τ inversely relates to the sample temperature. The translational diffusion D_T of the samples are measured by $\lim_{t\to\infty}\langle \Delta r^2(t)\rangle/2dt$. The sample is considered effectively two dimensional during

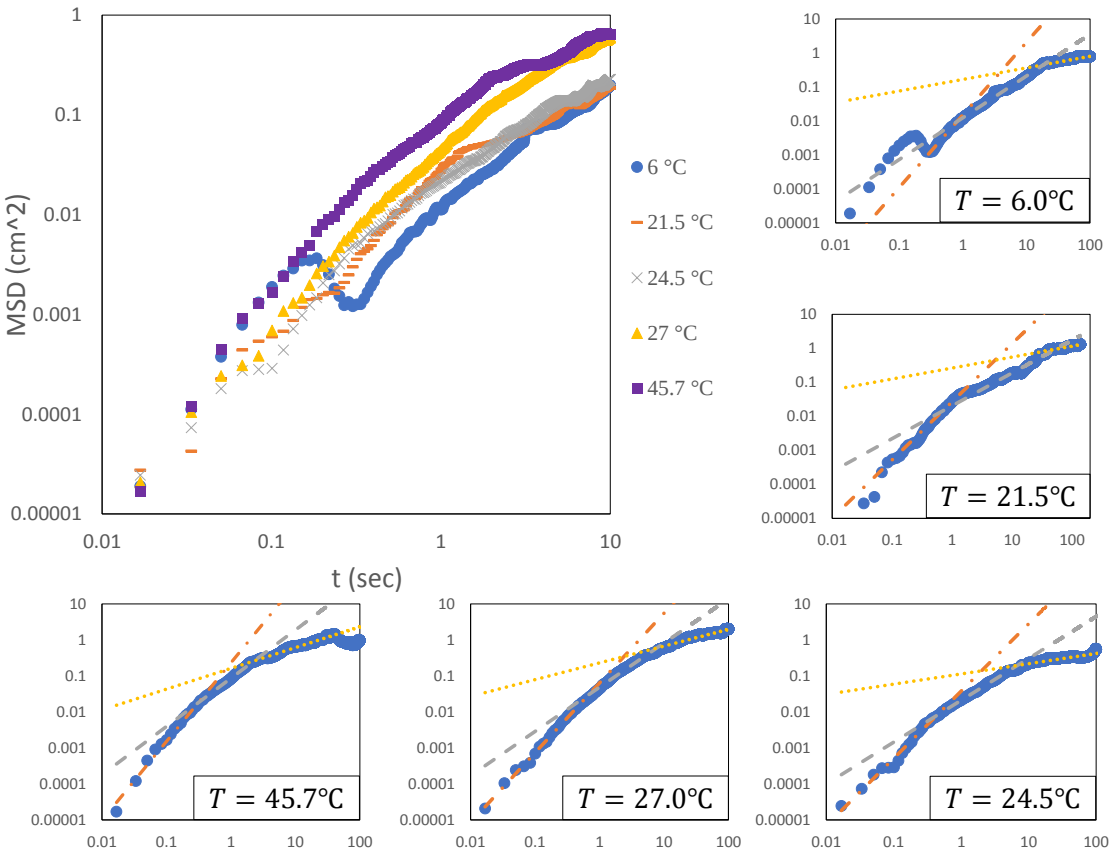

Figure 43: MSD vs time in a Log-Log plot for shrimp at different temperatures: 6.0, 21.5, 24.5, 27.0 and 45.7°C. The large plot shows how the MSD is affected by temperature with the lowest temperature having a smaller MSD at a given time and the highest temperature 45.7°C having the largest MSD at a given time. Also shown are how the slopes of the experimental data change in time for each temperature.

Table 1: Shrimp measurements at temperatures 6.0, 21.5, 24.5, 27.0, and 45.7°C. The persistence time τ is when the MSD at each of those temperatures transitions from $t^2 \to t$. The time τ_b is the time the MSD transitions from $t \to t^c$ where $c < 1$ which is due to the boundary of the petri dish. The average speed of the shrimp is given by $\bar{v}$. The translational diffusion D_T is calculated from the MSD. The rotational diffusion D_R is calculating from the max turning angles. Of note: the 21.5 °C sample repeatedly appears as an outlier and needs to be reproduced.

Temperature (°C)	τ (s)	τ_b (s)	$\bar{v}$ (cm/s)	D_T (cm^2/s)	D_R (1/s)
6.0 ± 0.1	0.95	20.61	0.6 ± 0.1	0.0016	23.9
21.5 ± 0.1	1.07	112.35	1.4 ± 0.2	0.0024	38.7
24.5 ± 0.1	0.54	6.87	0.9 ± 0.1	0.0017	21.8
27.0 ± 0.1	0.52	6.45	1.4 ± 0.2	0.0039	12.6
45.7 ± 0.1	0.31	2.28	1.6 ± 0.3	0.0101	11.1

the tracking of individual shrimp as the shrimp are only observed to swim in plane of the field of view.

Also observed in the MSD in Figure 43, after the diffusive part where the slope of the data is ≈ 1, is that a third slope appears. This happens at another time scale τ_b. Finally, the last interesting time scale which appears in the $T = 6.0$°C MSD. At $t \approx 0.5$s, the MSD sharply decrease before increasing again. This corresponds to a length scale $l \approx \sqrt{0.005}$ cm, which is the order of magnitude of the shrimp. This is likely caused by the shrimp stroke which was shown in Figure 37 where the shrimp will move backwards slightly before propelling themselves forward. As the lower temperature where the shrimp move slower, this is more apparent in the tracking and so appears more prominently in the MSD. Similar features can be seen but not as clearly for the other temperatures. For this feature to be clearer in future experiments at room temperature or higher, a higher frame rate will be needed when recording the shrimp trajectories.

Table 2: Simulation values for persistence time τ, rotational diffusion D_R, a length scale, and speed for different rotation angles and speeds.

θ_R (rad)	τ (s)	D_R (1/s)	$\sqrt{\frac{D_T}{D_R}}$	$\lvert v\rvert$ (cm/s)
$22\pi/100$	0.95	23.9	0.00818	0.49
$28\pi/100$	1.07	38.7	0.00787	0.47
$21\pi/100$	0.54	21.8	0.00882	0.53
$16\pi/100$	0.52	12.6	0.0176	1.06
$15\pi/100$	0.31	11.1	0.030	1.80

4.4.3.3 Modeling Individual Shrimp

The persistence time τ gives information for the time it takes the particles to rotate. In order to use this for modeling purposes, we need to determine the max rotation angle θ_R a particle uses for each time step. From this rotation angle, a random angle can be chosen. For this simulation, this angle is chosen such that $\theta \in [-\theta_R, \theta_R]$ is uniformly distributed.

After choosing θ_R, $N = 5000$ particles are integrated in time using Euler integration with $dt = 0.01$ and a constant speed $|v|$ which is taken from Table 1. The position is updated as follows,

$$\mathbf{r}_i(t + dt) = \mathbf{r}_i(t) + \mathbf{v}_i(t)dt \tag{47}$$

where $\mathbf{v}_i(t) = |v|(\cos\theta_i(t), \sin\theta_i(t))$. This simulation also includes zero-flux boundary conditions of a circle, in which, the initial positions and orientations of the particles are uniformly random.

For each parameter set, we calculate the auto-correlation function for the direction

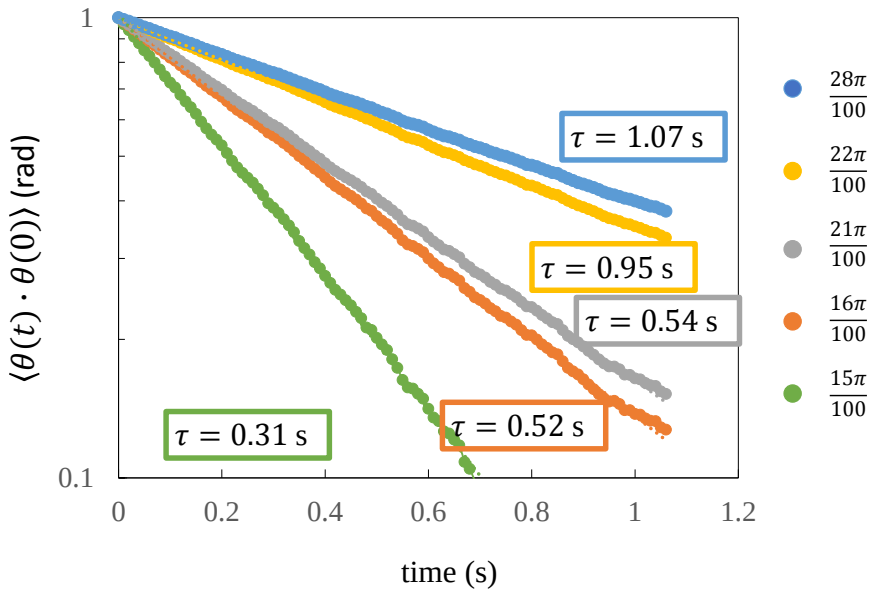

Figure 44: Simulation of the auto-correlation of shrimp direction for 5000 shrimp for different rotation angles. Each simulation is fit to an exponential function and the persistence time τ is read off.

of particles,

$$\langle \theta(t) \cdot \theta(0) \rangle = \frac{1}{N} \sum_{i=1}^{N} \cos\theta_i(t) \cos\theta_i(0) + \sin\theta_i(t) \sin\theta_i(0) \tag{48}$$

and fit the results to an exponential function of time $\exp^{-t/\tau}$ an exponential function of time is fit. Since it is expected that the direction correlation decays in time with a power of $1/\tau$, as shown in Equation (37), the power of the exponential fit gives the persistence time. Figure 44 shows five simulations that match the τ values from the shrimp tracking experiments.

These rotation angles θ_R are used to calculate the rotational diffusion constants D_R via the differential equation for the angular dynamics for self-propelled particles, Eq. (38). Setting $(2D_R)^{1/2}$ equal to the rotation angles, D_R are calculated for the different experiments shown in Table 2.

Using the calculated D_R and the measured D_T, we find a characteristic length

scale $\sqrt{D_t/D_R}$, which when divided by the time between frames in the tracking video, yields a speed. These speeds compare favorably with those calculated from experiment listed in Table 1. The individual dynamics agree with experiments. However, for a stronger understanding of the effects of temperature on the individual dynamics of these shrimp, more temperature experiments may be needed.

4.5 Discussion

The rich dynamics of *Artemia franciscana* and the relatively simple experimental setup make this a potentially useful toolbox for probing questions of collection behavior and pattern formation of active matter systems. Experiments can be set up to study the effects of different environmental factors on the statistical mechanics of Active Brownian Particle or pattern selection. Groundwork has been set for the short and long time dynamics of individual *Artemia* at a variety of temperatures showing a dependence of turning angle and speed of *Artemia* on temperature.

For shallow suspensions of aggregations of *Artemia* at temperatures in the range of 21-23 °C spatial patterns can be observed. Patterns that have been observed so far are those of long wavelength aggregations similar to cylindrical harmonics, $\exp^{in\phi} J_n(k_r r)$ where J_n is the n^{th} Bessel function and $k_r = \frac{j_{n,l}}{R}$ is the radial wavenumber, $j_{n,l}$ is the l^{th} zero of the n^{th} Bessel function, and R is the radius of the petri dish, as well as those of short wavelength aggregations similar to that of micro-phase separation. The reason for these two types of patterns to appear still needs to be investigated.

For one set of experiments, long wavelength patters are observed. These patterns are inversely dependent on concentration of the aggregation. More analysis is needed to study exact distribution of wavenumbers that have been observed as well as more resolution to the depth of the suspension of the system.

Small perturbations to the sample once the patterns form do not disturb the pattern, which have been seen in experiments. These studies can be investigated

further by having controlled oscillations to the system and observing how strong of a perturbation is need to cause mixing and disrupt the patterns.

Chapter V

SIMULATING WAVES, CHAOS AND SYNCHRONIZATION WITH A MICROCONTROLLER

5.1 Use of Microcontroller for studies of collective dynamics

For this section, we discuss a few of the models with have worked with and a new way of visualizing the dynamics for education purposes. Simulations of pattern formation [116–118], excitable media [119–121] and oscillating systems in general require the solution of multiple coupled ODEs in time (from simple models such as FHN [17, 18] and Hodgkin-Huxley (HH) [122], consisting of 2 and 4 variables respectively, to complex models with more than 80 variables [123]) and PDEs in space [124]. In many cases, the time and space discretization and the number of equations necessary to describe the system requires the use of large computational resources such as supercomputers [125–127]. As computational power continues to follow Moore's Law, which describes a power of two growth even 50 years after its conception [128], it has become easier to run large complex systems simulations using common desktop computers [129, 130]. This computational facility has, in recent years, been extended with the additional use of GPUs for scientific computing [131–133]. However, the increment in CPU power has also allowed the growth of another kind of resource to perform operations: microcontrollers (MC).

The first MC to combine read/write memory, processor and clock on one chip was created in 1971 by Texas Instruments. When introduced to the electronics industry in the form of the TMS-1000, it was used widely in calculators, toys and games, selling at an affordable $2 per unit in bulk orders [134]. In response, Intel developed a MC for

control applications in 1977, combining RAM and ROM on a single chip. These too permeated a range of applications, including PC keyboards. In the 1990s, advanced MCs were developed with electrically erasable and programmable ROM memories, which are still in use today by Atmel and Microchip. Today, MCs are even smaller, more powerful, cheaper, and used in both active research and everyday consumer items such as phones, automobiles and household appliances [135, 136].

In a recent example, Serna and Joshi simulated the logistic map using LED's driven by a MC [137]. They divided the $[0, 1]$ interval domain of the logistic map into ten equal parts and mapped each to an LED that is powered when trajectory of an initial seed lies in the corresponding interval. Fixed points are indicated by an LED that remains lit, while a group of such LEDs indicate a periodic orbit [137]. Separately, Mahmud *et al.* [138] modeled 1D cardiac tissue propagation using an analog circuits and dsPIC MCs, wherein each cell's voltage response was dictated by the Luo-Rudy phase I model [139]. Also, another example is the use of MCs to simulate the HH neuron model with output via the serial port or to an LCD [140], as well as the use of FPGA to solve the HH model [141, 142].

Because of their flexibility and low cost, MCs are becoming an important tool for physics education in the class room [143–145]. For example, Soriano et al. [146] discusses the use of different MCs for use in robotics for classroom activities and in the advancement of automatic control [146]. Also, different courses such as Cornell University's ECE 5760 "Advanced Microcontroller Design and System-on-Chip" have taught how to use a variety of MCs as components in electronic design. These lectures are listed on their website and go through multiple topics using a DE1-System-on-Chip (SoC) including visualizing the Mandelbrot set and simulating a Lorenz system. This course teaches more in-depth how the SoC works with other devices such as Field Programmable Gate Arrays and Digital Differential Analyzers [147].

The use of MCs is further demonstrated to simulate three biophysical systems

known for their rich dynamics that includes stable and unstable traveling waves, synchronization, spiral waves and chaos. The dynamics of waves in rings of neuronal tissue whose dynamics are governed by the standard FHN model [17, 18], which was discussed more at length in the introduction of Chapter 2, are visualized. While this section does not include simulations of FHN5, this extension can also be used for visualization purposes similar to what is discussed.

Then, a 3-variable phenomenological model of cardiac dynamics called the FK model [148] is studied. The three dynamic variables of the model are currents produced by the flow of Na^+, Ca^{2+}, and K^+ ions through a membrane; this model produces a more realistic cardiac action potential (AP) than the FHN. An action potential is the spike and dip of the membrane potential in cardiac cells that occurs when an electrical pulse passes through the tissue. This model is capable of demonstrating complex oscillatory pulse dynamics known as alternans [46] comparable to those observed in cardiac experiments [47–50].

Next, MCs are used to illustrate synchronization [149], an emergence of spontaneous order that can be observed in coupled oscillators such as cardiac cells [150] and fireflies [151]. The Kuramoto model [152], which describes the phase advance of coupled oscillators and can reproduce synchronization of weakly coupled homogeneous oscillators, is used for this purpose. While useful in some systems, such as the collective action of cardiac cells, synchronization is also responsible for destructive phenomena such as epileptic seizures [153] or the resonance caused by people crossing the London Millennium Footbridge while inadvertently synchronizing their footsteps with the oscillation of the structure [11].

5.2 Brief History of Microcontrollers

Microcontrollers come in all sizes and architectures, some even with their own Linux kernel installed and ready to use [154]. For simplicity and functionality, the Arduino

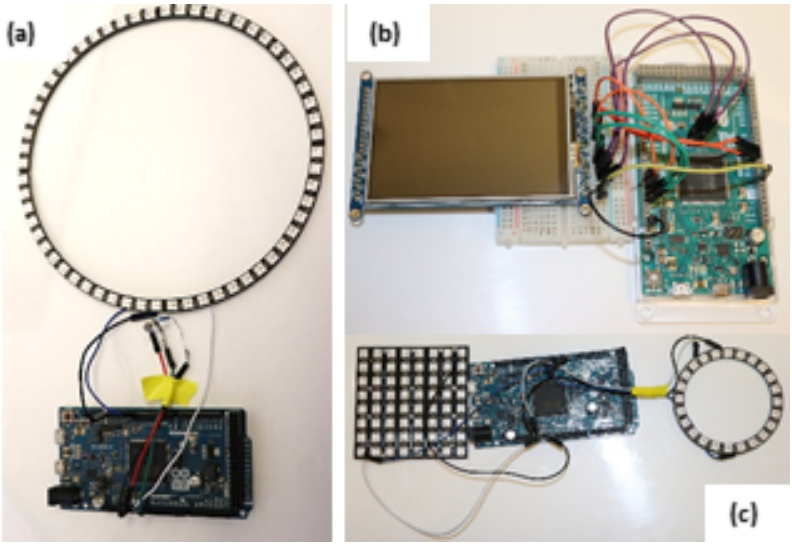

Figure 45: Arduino Due connected in a few setups. (a) the Adafruit NeoPixel 60 RGB LED ring and the photocell connected. (b) The LCD connected to a breadboad. Wire connections are listed in 3. (c) The Adafruit NeoPixel 24 RGB LED Ring and the NeoPixel 8×8 RGB LED Matrix.

Due, which is based on a 32-bit ARM core MC (cost of $39.95), is used. This is connected to the following for the different examples: (i) one Adafruit NeoPixel NeoMatrix square 8×8 RGB LED array ($34.95), (ii) four NeoPixel 1/4 60 RGB LED ($9.95 for each part), (iii) one circle Adafruit NeoPixel 24 RGB LED ring ($19.95), (iv) one Adafruit 3.5" TFT 320×480 + Touchscreen Breakout Board w/MicroSD Socket ($39.95) which also needs a breakout board for some more complicated connections, (v) a photoresister. The 60 LED ring comes in four sectors and must be previously connected by soldering the parts together. Each of these set ups are seen in Figure 45. Other displays can be used if touch screen is not needed or if a smaller size, such as the 2.8" TfT LCD with Touchscreen Breakout board w/MicroSD Socket ($29.95), is desired.

The MC that we use is the Arduino Due. The Arduino can be programmed with a language that has similar syntax to C and Java. The codes (called "sketches") can be uploaded from a computer through an USB using an Integrated Development Environment (IDE) that can run and control the LEDs even when not connected to

the computer.

For each Adafruit NeoPixel connection, three wires must also be connected to the Arduino: GND to GND, DIN to an assigned pin number, and 5V to 5V in Figure 45 (a,c). Pin numbers are assigned in the sketch written in the Arduino GUI which is then compiled and run on the Arduino itself. When programming the LED rings, the sketch must include:

```
Adafruit_NeoPixel strip = Adafruit_NeoPixel(N_LED,
Arduino_Input, NEO_GRB + NEO_KHZ800);
```

where `N_LED` is the number of LEDs in the ring being used (24 or 60 for these cases) and `Arduino_Input` is the number input of the Arduino connected to. For the ring, `Arduino_Input`= 6. For the LED matrix, the sketch must include

```
Adafruit_NeoMatrix matrix = Adafruit_NeoMatrix(x_LED, y_LED, Arduino_Input,
  NEO_MATRIX_TOP     + NEO_MATRIX_RIGHT +
  NEO_MATRIX_COLUMNS + NEO_MATRIX_PROGRESSIVE,
  NEO_GRB            + NEO_KHZ800);
```

where `x_LED` and `y_LED` is the number of LEDs in the x and y-direction on the matrix. For our matrix, both of these are 8. For the ring, `Arduino_Input`= 0.

Communicating with the LEDs is simple and it is possible to program an over-all brightness for the LEDs and pixel color on an RGB scale from 0 to 255 by using functions from the `Adafruit_NeoPixel` library:

```
matrix.setBrightness(100);
matrix.setPixelColor(n, red, green, blue);
```

The brightness function gets called once to set a limit on the overall brightness each pixel can take. Here, `n` represents the LED number which can take values $[0, 23]$ for the ring and $[0, 63]$ for the matrix. To upload and compile the sketch, the Arduino must be connected first to a computer, but afterwards can be connected to a charger and run as is. For interaction with the simulation, an Adafruit photocell (CdS photoresistor)

($0.95 each) with a 10k resistor connected in series with the Adafruit LEDs can be used. The photoresistor is used in the FHN experiments in Section 5.3 and can be attached simply between LEDs. In order for the Arduino to interact with the photocell, the following lines need to be included in the `setup()` part of the Arduino sketch

```
int photocellPin = A0; // select the input pin for LDR
int photocellReading = 0; // to store value coming from the sensor
```

and in the `loop()` function, the following is included in the sketch:

```
photocellReading = analogRead(photocellPin); // read value from
// sensor
```

Then the `photocellReading` can be used as a variable in the model that is being implemented.

Finally, for the touchscreen, the Arduino Due is assembled as shown in Figure 45 (b) which is as follows if using a breadboard which was adapted from the Adafruit website [155] where the left is the connection on the pin and the right is the connection on the breadboard. Table 3 lists how the wires connect from the Arduino and the Breadboard where the Touchscreen is connected. Finally, the USB wire is connected to the computer and the Programming Port on the Arduino. The touchscreen SPI interface pins connect the GND pin to row 6 on the breadboard and continues down the column with CD pin ending on row 25.

The following lines are included into the Arduino sketch outside of the `setup()` and `loop()` functions:

```
#define LCD_CS A3 // Chip Select goes to Analog 3
#define LCD_CD A2 // Command/Data goes to Analog 2
#define LCD_WR A1 // LCD Write goes to Analog 1
#define LCD_RD A0 // LCD Read goes to Analog 0

// These are the four touchscreen analog pins
```

Table 3: Touchscreen Connections. Wire connections for the Touchscreen to the breadboard as shown in Fig 45. The first column shows the color of wire in the image. The second column shows where on the Arduino that wire connects. The third column shows the row on the breadboard.

Color	Arduino	Breadboard
Yellow	5V	7, first column
Orange	A2	18, first column
Orange	A3	17, first column
Orange	7	16, first column
Orange	8	19, first column
Green	9	13, first column
Green	10	12, first column
Black	GND	–
Blue	SPI SCK pin	9, first column
Blue	SPI MISO pin	10, first column
Blue	SPI MOSI pin	11, first column

```
#define YP A2  // must be an analog pin, use "An" notation!
#define XM A3  // must be an analog pin, use "An" notation!
#define YM 7   // can be a digital pin
#define XP 8   // can be a digital pin
#define LCD_RESET A4 // Can also just connect to Arduino's
// reset pin

// For the Arduino Due, use digital pins 33 through 40
// (on the 2-row header at the end of the board).
D0 connects to digital pin 33
D1 connects to digital pin 34
D2 connects to digital pin 35
D3 connects to digital pin 36
D4 connects to digital pin 37
D5 connects to digital pin 38
D6 connects to digital pin 39
D7 connects to digital pin 40

#define TS_MINX 110
#define TS_MINY 80
#define TS_MAXX 900
#define TS_MAXY 940

// The display uses hardware SPI, plus #9 & #10
```

```
#define TFT_RST -1
#define TFT_DC 9
#define TFT_CS 10

Adafruit_HX8357 tft = Adafruit_HX8357(TFT_CS, TFT_DC, TFT_RST);
TouchScreen ts = TouchScreen(XP, YP, XM, YM, 300);

#define BLACK   0x0000
#define BLUE    0x001F
#define RED     0xF800
#define GREEN   0x07E0
#define CYAN    0x07FF
#define MAGENTA 0xF81F
#define YELLOW  0xFFE0
#define WHITE   0xFFFF

#define BOXSIZE 40
#define PENRADIUS 15
```

which is needed for the Arduino to communicate with the screen.

5.3 Dynamics of The FitzHugh-Nagumo Model

The FHN model is one of the simplest models used to describe excitable systems such as chemical reactions [156], neurons [157] and myocytes [158]. It uses two variables to govern its dynamics, one fast denoted as v and one slow variable denoted as w. Depending on the system described (e.g. chemical, cardiac-neural, population dynamics), v can be associated with the activator, voltage, or prey respectively while w with the inhibitor, ionic current, or predator. The model is thus described by two coupled ODEs, namely

$$\begin{aligned} \frac{dv}{dt} &= v(a-v)(v-1) - w \\ \frac{dw}{dt} &= \epsilon(bv - dw - \delta) \end{aligned} \tag{49}$$

where a, b, d, δ, and ϵ are parameters which affect the location and type of equilibria and the speed of oscillations. Depending on model parameters, dynamics can be oscillatory or excitable. In general, the values used for $\epsilon << 1$ which makes the v dynamics faster compared to w.

5.3.1 Interaction with a single FHN oscillator

As a first example, the dynamics of a single FHN cell in an oscillatory regime are simulated. The v variable oscillates and its value is plotted in time on an interactive LCD (Figure 46). The LCD displays the current value of v at the left side of the screen and propagates the value in time to the right with the right side being the furthest back in time.

If untouched, the screen will trace the auto-oscillatory signal, or action potential, in time as shown in Figure 46(a-b). The FHN is characterized by a fast upstroke, a plateau, and fast down-stroke to rest state. In this regime during the oscillator's rest state, it can still be perturbed and excited by a stimulus.

To incorporate this functionality into the simulation, the value of v can be made to be increased by a certain amount proportional to the pressure `p.z` applied anywhere on the LCD touchscreen by simply adding the following line:

```
v+=p.z/130;
```

where the maximum pressure of 1000 is scaled so that it corresponds to a value that is comparable to values that the oscillator can achieve normally. This adds in some value between 0 (no press) and 7.7 (hardest press) to our v variable during the time of the interaction. However, this can be modified depending on how the user will want the pressure to relate to the cell excitation. This way, by touching anywhere on the screen, the cell will get excited not only proportional to the pressure but also for the duration of the user's touch on the screen. This modifies the FHN equations as follows:

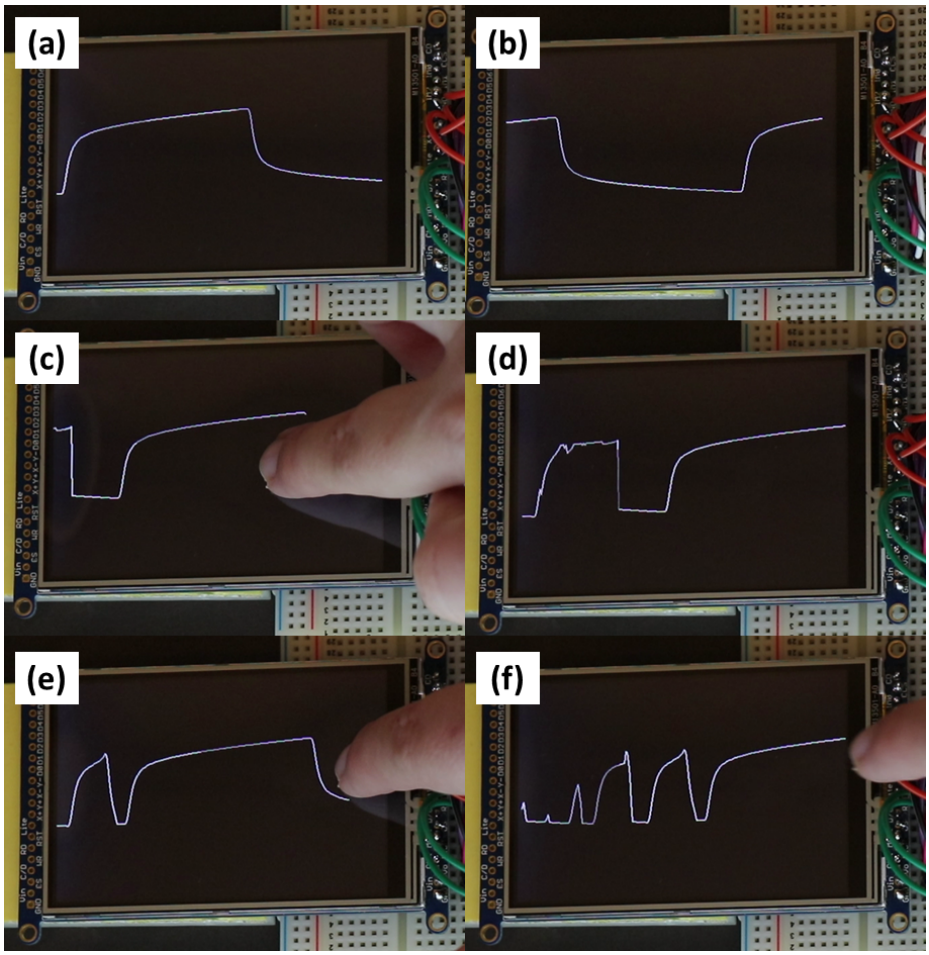

Figure 46: Six images of the touchscreen showing the action potential of one FHN oscillator. (a) A few seconds after the simulation begins, a full action potential is drawn on the touch screen. (b) This action potential will repeat at a constant frequency if left untouched. (c) While interacting with the touchscreen, the oscillator will excite, causing the voltage to increase by a certain amount depending on the pressure applied to the screen. (d) Releasing the touchscreen will cause the oscillator to start to relax. When the oscillator is excited too soon after the previous excitation, the action potential will be shorter than the typical size. (e, f) Interacting with the touchscreen very quickly after the oscillator relaxes will cause smaller and shorter excitations while the oscillator is in refractory period.

$$\begin{aligned} \frac{dv}{dt} &= v(a-v)(v-1) - w + I(t) \\ \frac{dw}{dt} &= \epsilon(bv - dw - \delta) \end{aligned} \tag{50}$$

where I is the impulse the user gives the oscillator.

Depending on when during the oscillation's period the screen is touched, the cell may excite if the stimulus is strong enough[17]. If the cell is excited during the rest period, it can easily produce early activations as shown in Figure 46(c-d) where the excitation is shown on the left (Figure 46c) and after the simulation continues, the there is a small action potential as the oscillator then continues back to rest (Figure 46d). However, if attempting to excite the cell while already excited or in the refractory period, the oscillator will not excite completely (Figs. 46(e-f)). Figure 46e shows a user interact with the screen to excite the oscillator a few times shortly after a small early activation and Figure 46f shows the results of these four additional excitations, the first which is another early activation, and then three where the oscillator is not able to excite out of the refractory period and dies very quickly.

5.3.2 1D waves in a Ring of FHN Oscillators

In systems of coupled cells, pulse solutions, multiple pulse solutions, and periodic traveling waves in the FHN model have been proven to exist [28] and their stability has also been studied [159, 160]. Specific studies of rotating wave solutions on a circular ring have shown that the existence of these solutions and their possible wavelengths depends on either diffusion coefficients or the domain size [161]. In here, the focus is on the these traveling waves, one of the main known solutions. They can be obtained by exciting a group of cells to a higher voltage potential and integrating forward in time.

When exciting cells in a ring, they will elicit waves propagating in each direction

from the stimulus site (right and left), however by using unidirectional block [162] it is possible to start waves in only one direction. These rotating waves have been shown to occur in cardiac tissue and act as anatomically induced rotating waves, known as reentrant waves, causing tachycardia [21]. In the FHN, there is a small parameter regime where waves can be elicit intermittently in each direction[163] from a single stimulus, a state that can be considered as a one dimensional spiral wave.

Here, the FHN model (Eq. 50) is integrated numerically but modified to have spatial coupling with nearest neighboring cells, with the altered equations given by

$$\begin{aligned} \frac{dv_i}{dt} &= v_i(a - v_i)(v_i - 1) - w + D\nabla^2 v_i, \\ \frac{dw_i}{dt} &= \epsilon(bv_i - dw_i - \delta), \end{aligned} \tag{51}$$

where we use the parameter values $a = 0.2$, $b = 0.5$, $d = 1$, $\delta = 0$ and $\epsilon = 0.0095$, simulating an excitable system that can sustain traveling waves. For this integration, an explicit Euler method with a $(dx)^2 = 1$ and $dt = 0.4$, which leads to convergent results in 1D [45], is used. The solution is plotted in real time to a ring of LEDs where each LED represents a cell in the simulation. Figure 47 (a) shows propagation of a stable wave (red LEDs) along the LED ring with a period of complete rotation of 3.27 seconds. This can be measured with stopwatch while watching the LEDs light up around the ring, or for more exact measurements, by using the Arduino Serial to print out value. Also, this wave has a wavelength of about 18 LEDs depending on what brightness we consider as part of the excitation, or an arclength of 108∘. These measurements are easy to take: a stopwatch or a video taken via camera or phone can be used to track the wave completing a cycle. For more accurate measurements, a tracking program can be used to track the wave front and back propagating around the LED ring.

For comparison, a simulation using a Java applet of the same system as the Arduino setup to plot the v (white) in time is shown in Figure 47 (b). For the same parameters as used in the Arduino, the wave speed and wavelength can be measured. For the wavelength, a threshold is set for the voltage and the number of cells above that threshold at a certain time are measured. Therefore, the wavelength will change slightly depending on the threshold [45]. This is similar to how the wavelength of the LEDs is measured by picking a certain brightness that can be distinguish by eye. To facilitate calculations, the threshold is picked to be $V = 0$ and measured a wavelength of 20 cells, or 120∘ for the arclength. One complete rotation takes 154 unit time steps.

Figure 47 compares both the LEDs and Java applet as well as showing the value of the calculations plotting (Figure 47 (c))which can be read out using the Arduino serial while connected to a computer. In both cases, it can be seen that once the wave is stable, the wavelength and amplitude is also stable.

It is possible to also connect a photocell to the Adafruit ring to have a simple interaction via incoming light. This makes the simulation interactive by touching the photocell, and a pulse with voltage dependant on the amount of light blocked can be programmed to propagate out in both directions along the ring. This may cause the wave that is traveling along the LED ring to break up. Connections can be made following the user's guide on the Adafruit website [164].

Similar to the change made for interacting with the FHN single oscillator with the touchscreen in Eq. (50), an impulse is added to one oscillator in the the ring. In this case, the impulse is given as follows:

```
I=(1023-photocellReading)/130;
```

where `photocellReading` takes a value between $[0, -1023]$. As the sensor gets darker, this line will make the impulse higher with the highest about 7.9. Similar to the single cell, if the impulse isn't large enough, the pulse will die, which will be seen

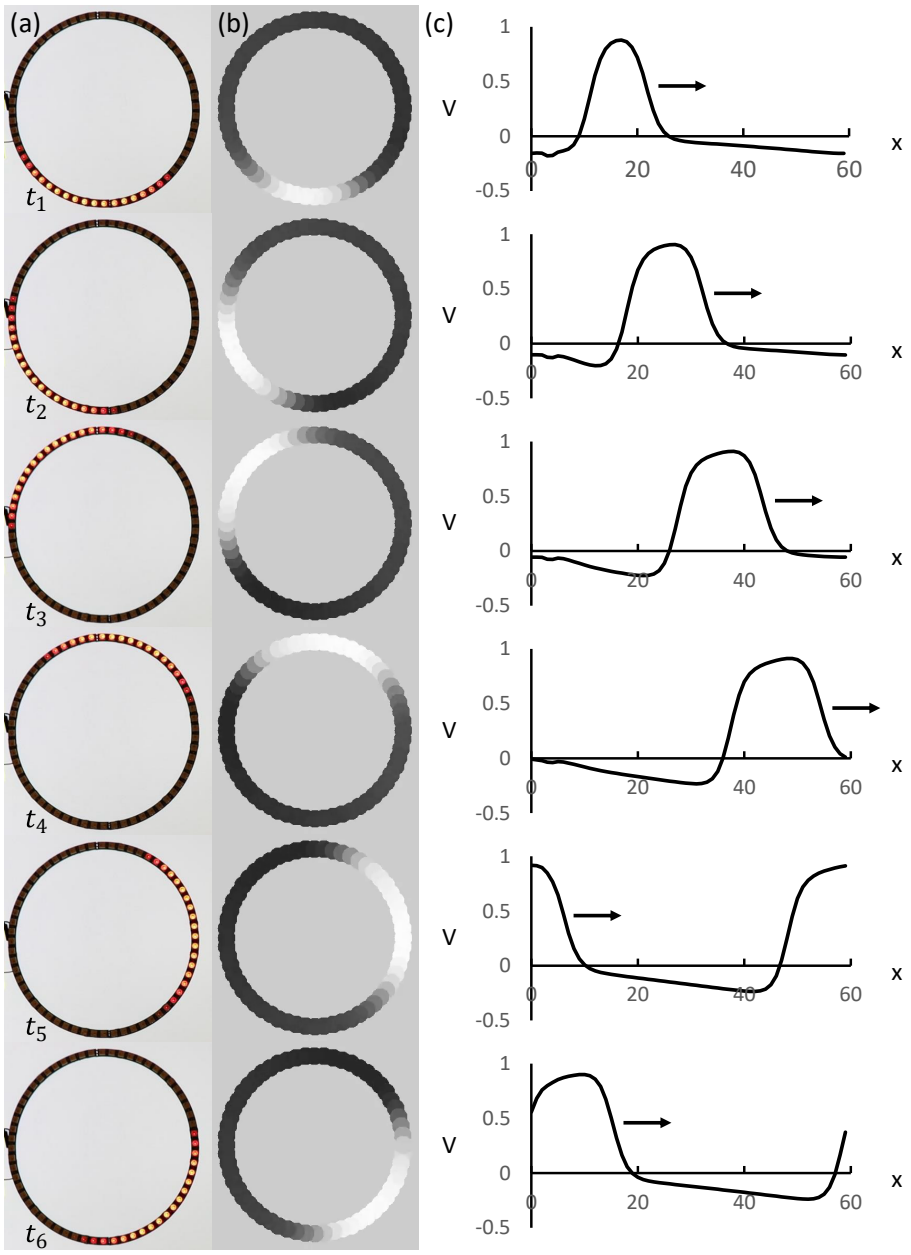

Figure 47: (a) Six images at different times of Adafruit 60 LED ring running FHN model where the brightest red LEDs show the peak v and the off LEDs show the minimum v. (b) Six still images of the simulation of the FHN model on a ring taken at 25 time-step intervals. (c) Voltage-position plots showing the wave propagates clockwise and the wavelength is constant.

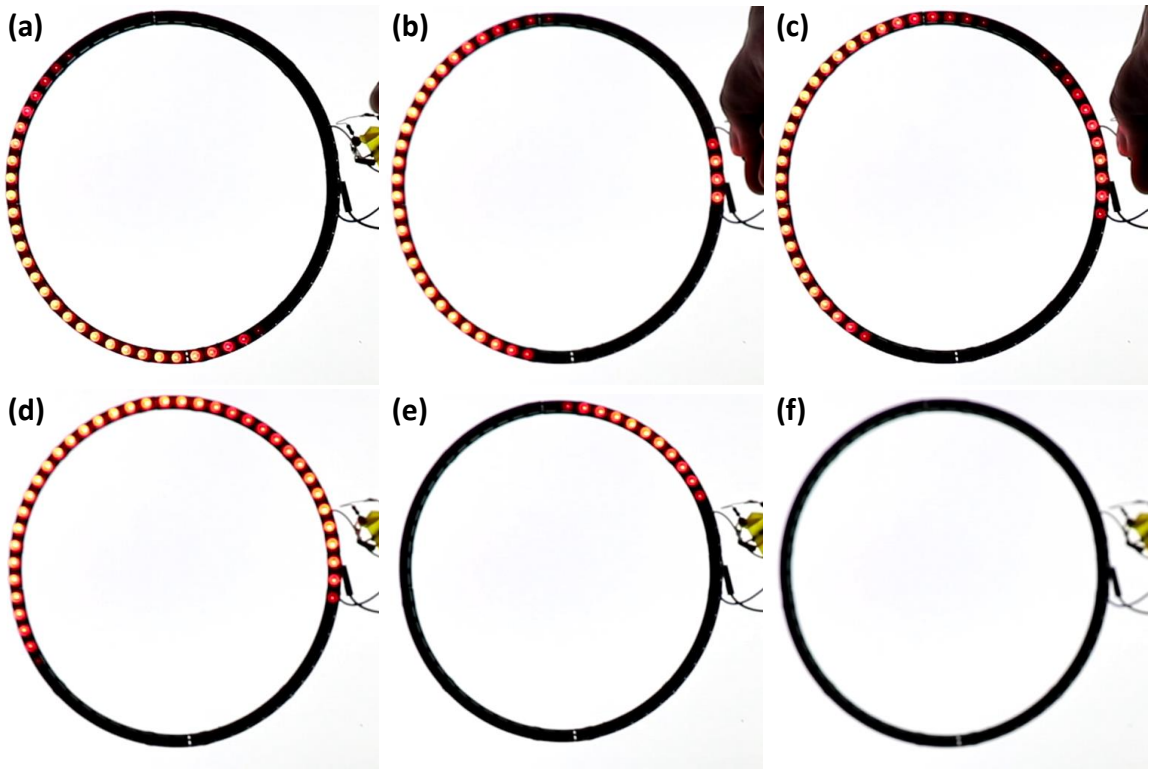

Figure 48: Interaction using a photocell with a FHN wave that is traveling around the LED ring like in the previous section. (a) The FHN wave is traveling counter clockwise. (b) Light to the photocell is blocked via a finger and cells near the photocell light up as they get activated. (c) This activation begins to spread as a wave counterclockwise as the cells clockwise are still in refractory period and block the wave. (d) The initial wave and the instigated wave collide. (e) The two waves begin to annihilate each other. (f) None of the cells are activated and the traveling wave is gone.

by an LED briefly lighting up and then dimming.

Two examples of the photocell interacting with the FHN wave are shown. Figure 48(a-c) shows a user covering the photocell which causes a cell on the right hand side of the 60 LED ring to excite. This then causes a wave to propagate. The wave can propagate in both directions but here, the cells direction clockwise are still in refractory period causing it to only propagate counterclockwise. Because a wave was already initialized and traveling counterclockwise, this new wave collides with it [Figure 48(d)], both waves annihilate each other. If left with no more interaction, there will be no more waves propagating around the ring [Figure 48(f)].

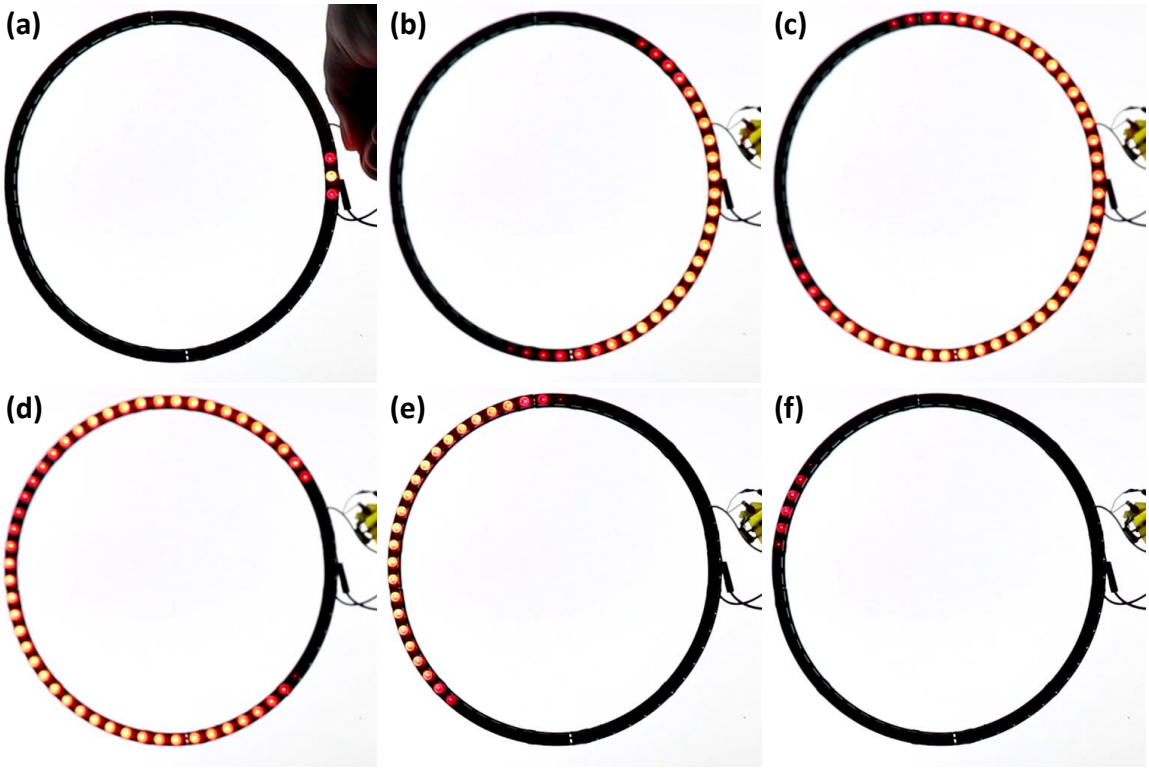

Figure 49: Example 2 of interaction using a photocell with a FHN oscillators. (a) There is no initial wave and light to the photocell is blocked via a finger and cells near the photocell light up as they get activated. (b-c) This activation begins to spread as a wave both clockwise and counterclockwise. (d-e) The two wave fronts collide and the wave begins to die out. (f) The wave dies out completely and there is no more activation.

In the second example, all cells begin in rest, shown by all the LEDs being off [Figure 49]. The user then covers the photoresister which excites the first cell [Figure 49(a)]. Since none of the cells are currently in the refractory period, the wave propagates in both directions until it collides [Figure 49(b-d)] and annihilates itself [Figure 49(e-f)].

5.3.3 2D Spiral Waves in the FHN

Reaction diffusion systems display several emerging behaviours as the dimension is increased. In 2D, besides plane and circle waves which can be seen as an extension of the 1D dynamics, more complicated dynamics like spiral waves can be formed when the symmetry is broken [165]. To illustrate the induction of spiral waves, we

extend the FHN to a two dimensional grid-lattice topology with nearest neighbor coupling. Spiral waves can be seen in many physical and biological systems such as during ventricular fibrillation in the heart [25], retinal spreading depression [53]. The interaction of external agents with the spiral waves can also create more complicated dynamics.

For visualization and interactivity, the Adafruit 3.5" TFT 320×480 + Touchscreen Breakout Board w/MicroSD Socket is used with the Arduino. This has 320×480 pixels and is interactive via pressure. The Arduino Due is limited in memory, however, so the largest system we simulate in here is 64×96 with each simulated cell being 5×5 pixels in size. larger domains can be implemented with more expensive microcontrollers such as Raspberry Pi. The connections for the screen are more complicated than for the LED strip and matrix shown in the previous sections, but can be found on the Adafruit site for several Arduino systems. For the Due, we follow the same connections except we connect to the IPSC pins.

For this simulation, Equation 51 is extended to 2D (4 nearest neighbors for the coupling term) and the integration parameters $dt = 0.06$ and $(dx)^2 = 1.2$ are used. Variables for this simulation are $a = 2.2$, $b = 1.0$, $d = 0.05$, $\epsilon = 1$, and $\delta = 0$ which leads to a system that can sustain rotating spiral waves.

To simulate spiral waves, which is one of the key dynamics studied in cardiac models, a particular set of initial conditions is used [165]. By setting the membrane potential v of half of a row of cells and the recovery variable w of row adjacent on one side higher than the resting potential, conduction blocking occurs causing the wave to only propagate in one direction.

The pressure sensor of the Adafruit display is used to make it interactive. Touching the screen will activate the section of cells touched, increasing the membrane potential and changing the local dynamics. The Arduino can determine the location of the touch and transfer that to a location in our simulation grid depending on how many

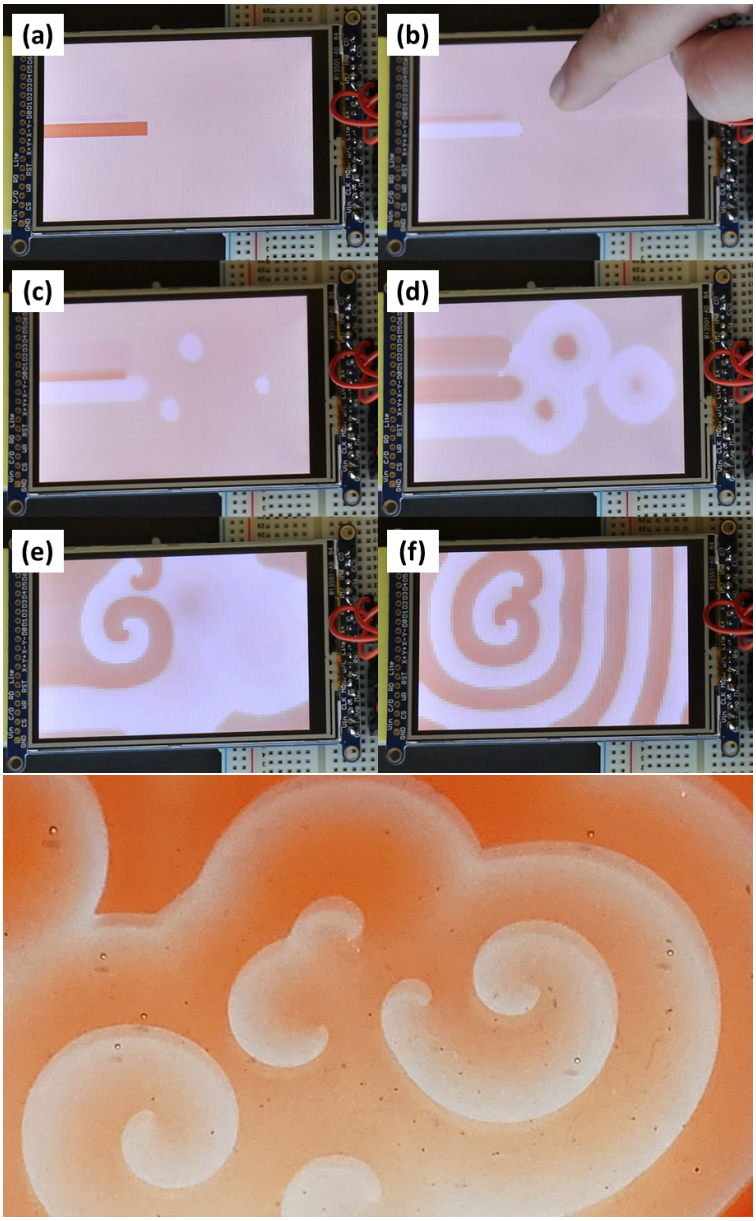

Figure 50: Top: Images of the 2D FHN model running on the Arduino with the LCD. (a) The initial conditions used to begin a spiral wave. Half a row begins in refractory and shown as the darker color with a row above slightly excited (not seen). All other cells are in rest. (b) A user interacting with the display as the simulation continues. (c) Three white spots on the right of the display show three locations where the user interacted with the display and those cells are now excited. (d) The three locations propagate target waves outward from the interacted cells. The initial activation beings to propagate out and rotate around the initial refractory cells. (e) Two spirals begin to form as the previous waves collide. (f) Much later when two stable spiral waves have formed. Bottom: Spiral waves in the Belousov-Zhabotinsky chemical reaction. The white color is the activation in the reaction and the waves are able to propagate as spirals.

cells you choose to simulate:

```
if (p.z > MINPRESSURE && p.z < MAXPRESSURE) {
  p.x = map(p.x, TS_MINX, TS_MAXX, tft.width(), 0);
  p.y = map(p.y, TS_MINY, TS_MAXY, tft.height(), 0);
  int xt=p.x/cellSize;
  int yt=p.y/cellSize;
  vt[xt][yt]=3;
  v[xt][yt]=3;

  for(int i=0;i<PENRADIUS;i++){
    for(int j=0;j<20;j++){
      xt=(i*cos(j*PI/10)+p.x)/cellSize;
      yt=(j*sin(j*PI/10)+p.y)/cellSize;
      vt[xt][yt]=3;
      v[xt][yt]=3;
    }
  }
}
```

This can cause the spiral waves to break up leading to more complex dynamics.

The Ardiuno simulations can also be directly compared with, for example, the spiral waves formed with the Belousov-Zhabotinsky chemical reaction [52]. In Figure 50, the formation of spiral waves in a Petri dish can be compared to the simulation. The petri dish is filled with a solution of 7mL from a 1L mixture (made with 84g of $KBrO_3$ in diluted in 1L of 0.6 M sulfuric acid) with 3.5mL from a 1L mixture (made with 52 g of malonic acid in 1 L of distilled water) and 1mL from a 10mL mixture (made with NaBr dissolved in 10mL of distilled water). After mixing the three components, bromine will form from the oxidation of bromide resulting in a brown color. The bromine will slowly disappears as it reacts with the malonic acid forming bromomalonic acid and converting the reaction back to clear. Then 1.0mL of ferroin is added to start the BZ reaction [166].

Pouring the reaction into a petri dish so that liquid is a thin layer and will yield a medium that is effectively 2D for the reaction. If a location in the reaction is

touched with a silver wire, the reaction will initiate there and behave similarly to a user interacting with the 2D FHN on the LCD. This reaction will lead to target waves propagating outwards like Figure 50(d) and colliding waves will create spirals.

5.4 1D waves in the Fenton-Karma Model

The second model implemented is the Fenton-Karma model (FK) [148]. This is a simplified model that reproduces the voltage (membrane potential) of cardiac cells, known as action potential using three variables, V, v, and w. This model captures similar behavior as the ones produced by some more complex cardiac cell models like Beeler-Rueter (BR) or Luo-Rudy (LR), both eight variable models, but without the heavier computational load. This model reproduces several key aspects of cardiac tissue, including the upstroke time scale of the action potential, adaptation of the action potential, and conduction velocity to changes in period of pacing stimulation, and a minimal diastolic interval before conduction block. This allows the model to match not only the dynamics of other cardiac cell models, but also to reproduce experimental data [162].

The FK model is given by a set of three differential equations:

$$\begin{aligned} \partial_t V(\vec{x},t) =& \nabla \cdot (\tilde{D}\nabla V) - \frac{I_{fi}(V;v) + I_{so}(V) + I_{si}(V;w)}{C_m} \\ \partial_t v(t) =& \frac{(1-p)(1-v)}{\tau_v^-(V)} - \frac{pv}{\tau_v^+} \\ \partial_t w(t) =& \frac{(1-p)(1-w)}{\tau_w^-(V)} - \frac{pw}{\tau_w^+} \end{aligned} \tag{52}$$

Where

$$\begin{aligned} I_{fi}(V;v) =& -\frac{v\Theta(V-V_c)(V-V_c)(V_m-V)}{\tau_d} \\ I_{so}(V) =& (V-V_o)\frac{1-\Theta(V-V_c)}{\tau_o}+\frac{\Theta(V-V_c)}{\tau_r} \\ I_{si}(V;w) =& -w\frac{1+\tanh\left(k(V-V_c^{si})\right)}{2\tau_{si}} \end{aligned} \tag{53}$$

In this model, I_{fi}, I_{so} and I_{si} represent the fast inward Na^+ current, the slow inward Ca^{2+} current, and the slow outward K^+ current respectively. The V, v and w variables represent the membrane voltage, fast sodium gate and slow calcium gate variables respectively. All other parameters are described in the original publication[148].

One key complex dynamical instability that appears in cardiac tissue in most animal species is a period doubling bifurcation that develops at fast pacing periods of stimulation known as alternans. This bifurcation was first described via a cobweb map [47] of the action potential restitution curve by Nolasco and Dhalen and then by linear stability analysis by Leon *et al.* [48]. This bifurcation is important as it has been linked clinically to what is called T-wave alternans (TWA) [49], a prognostic for arrhythmias. People who are diagnosed with TWA have been shown to have a very short survival life span (80% death within 2 years) [167], and it is also used by the U.S. Food and Drug Administration as a marker for drugs that can lead to arrhythmias. Thus, over the years, there have been a lot of efforts towards the study of this bifurcation in time and space [46, 49, 167–169]. One example of alternans can be observed in rings when pulses change wavelength due to this bifurcation [46]. When the ring is small enough for the period of rotation to fall below the period doubling bifurcation, discordant alternans develops [21, 130]. This is shown in Figure 51 for the LEDs and a Java applet where successive pulses alternate between long and short periods as they propagate [170], in contrast with the constant wavelength shown

by the FHN. The LED ring representation gives a clear visualization of this shrinking and lengthening of pulses and the Figure (a-c) $t_1 - t_4$ show one pulse which grows in time as it propagates until it reaches the back of the same wave. Furthermore, at very high levels of alternans, sometimes wave backs have to collapse [170] resulting in a single wave front and three wave backs [Figure 51 (a) $t_5 - t_6$, (b) $t_5 - t_6$, and (c) $t_5 - t_6$]. This has recently been shown in canine experiments [171]. For the size of ring here, the wave collapses.

In the FK model, these alternans can be observed for a set of parameters [172] and as the size of the ring is decreased (by changing, for example, the diffusion coefficient or the tissue discretization while keeping the integration resolved) [130] as shown in Figure 51.

5.5 The Kuramoto Model

The Kuramoto model [173] is a widely explored model used to describe the dynamics of oscillators with weak coupling which will synchronize when the coupling strength is larger than a critical value [174]. It was originally motivated to describe biological and chemical oscillators [173, 175], but can also describe the behavior of physical oscillator systems like coupled pendula and a coupled array of Josephson junctions [176]. This system can be studied with various topologies or complex networks [177–179] as well as with noise or time delay [180] depending on the system of interest. Here, the Arduino is implementated for three cases: the completely connected (case 1), the spatially extended two dimensional topology with nearest neighbor coupling (case 2), and the ring topology with non-local coupling (case 3) which exhibits a complex dynamics called chimeras.

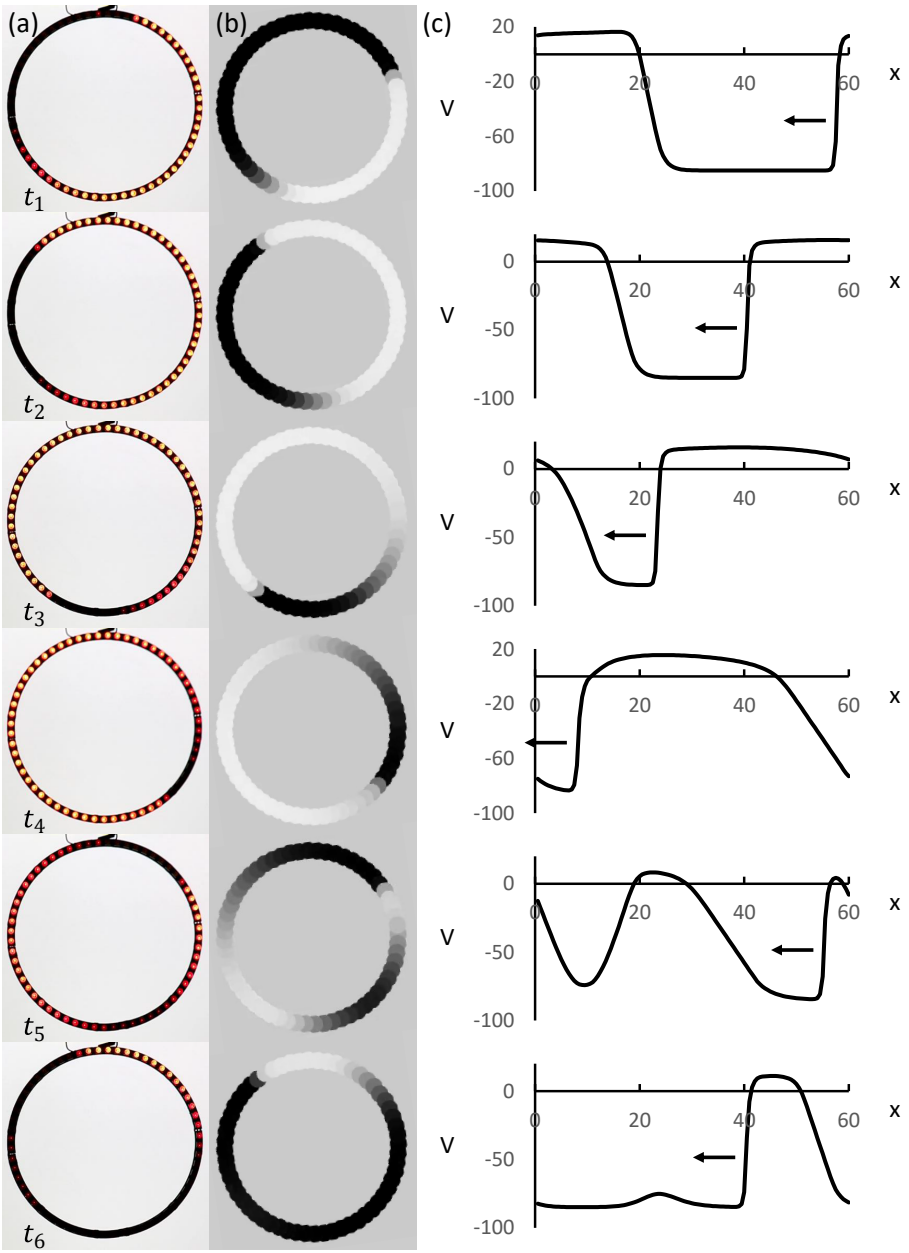

Figure 51: (a) A column of six still images taken at 48 seconds apart of the 60 LED ring simulating the FK model. The red LEDs are the cells that are activated. The wavefront travels counterclockwise. (b) A column of six computer simulations of the FK model on a ring with images taken at 48 time-step intervals. The white sections of the ring are the parts that are activated. (c) The voltage-position plots of the FK simulations. The wave propagates counterclockwise and the wavelength oscillates in time. The 5th set of images shows "alternans" where the wave breaks and two waves begin traveling. The 6th set shows one wave die out and one wave continues to travel counterclockwise.

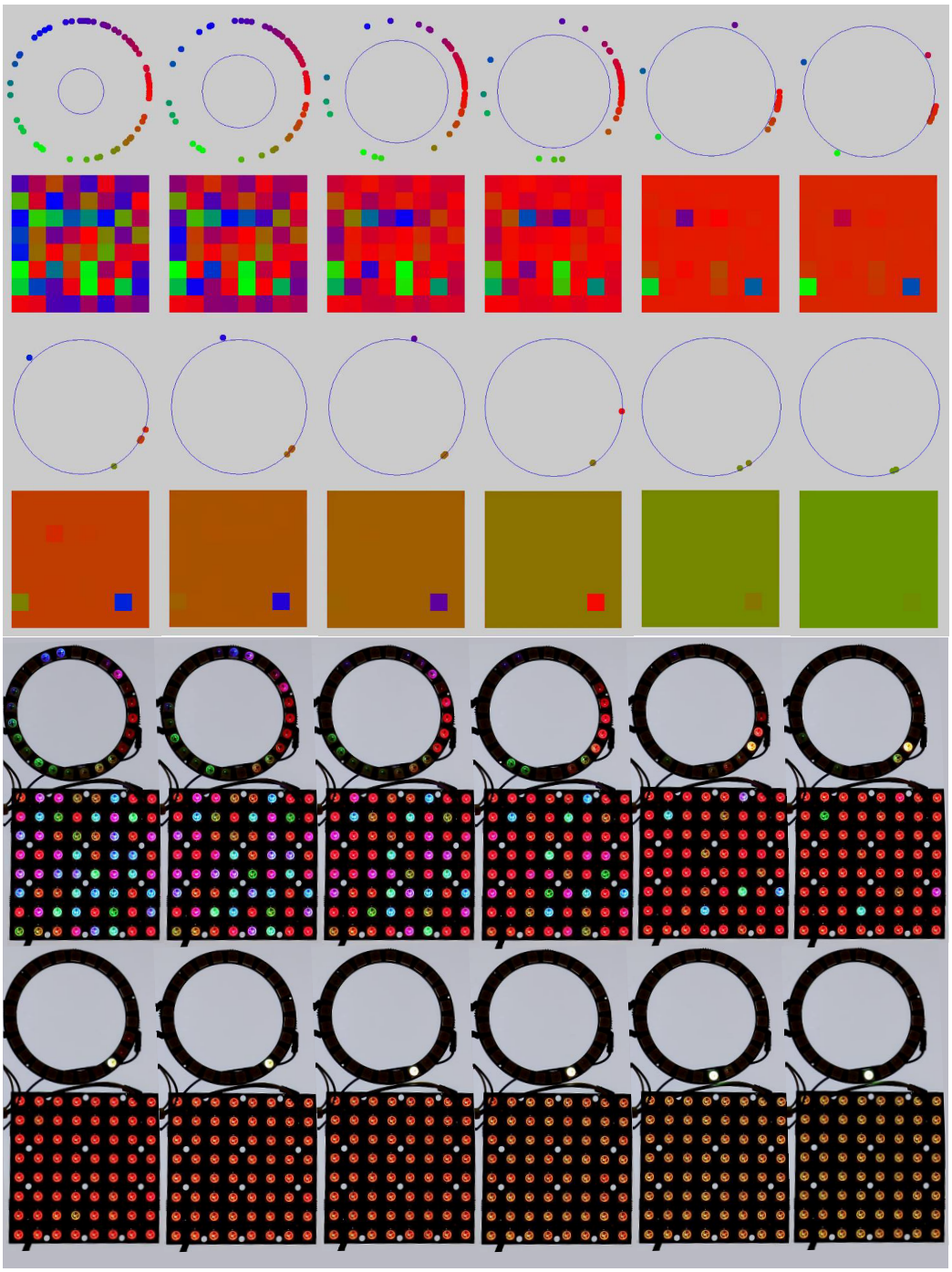

Figure 52: Top. Java applet of the Kuramoto model on an 8×8 LED grid with order parameter shown by the ring. The individual oscillators traverse 0 to 2π ring, from red to green to blue back to red. Bottom. Same set-up on the Arduino 8×8 LED array and 24 LED ring. Both are using all-to-all coupling. The Arduino images are taken every 4 frames from a 59 frame/sec video.

5.5.1 Case 1: Completely Connected Topology

Each Kuramoto oscillator obeys the following differential equation for their phase:

$$\frac{d\theta_i}{dt} = \omega_i + \sigma \sum_{j=0}^{N-1} \sin\left(\theta_j - \theta_i\right) \tag{54}$$

This model describes the change of phase θ_i of oscillators with natural frequency ω_i, and coupling strength σ. The regime of interest is characterized by coupling that is small compared to the natural frequency. We use ω_i sampled from a Gaussian distribution centered at 3π with a standard deviation of $\pi/2$ and σ in the range $[0, 1]$. Each oscillator is coupled to every other oscillator.

The critical coupling, σ_c, is the coupling after which the steady state dynamics change. For coupling larger than the critical coupling $\sigma > \sigma_c > 0$, the system will always phase synchronize in the completely connected model. Below this critical coupling, $\sigma_c > \sigma > 0$, the oscillators will remain decoherent.

In this system, phase coherence can be studied through an order parameter [174, 181] which can be defined as:

$$re^{i\phi} = \frac{1}{N} \sum_{j=0}^{n-1} e^{i\theta_j} \tag{55}$$

This visualizes the oscillators as traveling from $[0, 2\pi)$ with an average phase of ϕ with r describing the coherence of the oscillators with $r = 0$ when the phases are completely spread out and $r = 1$ when the phases are all the same.

For this set up, the an 8×8 LED grid and the 24 LED ring are used. Each LED on the grid represents a single Kuramoto oscillator with intensity, scaled from $[0, 255]$, indicating its phase $[0 - \frac{2}{\pi})$. In the ring, each LED indicates a phase range of $\frac{\pi}{12}$ radians, where the top LED corresponds to the range $[0 - \frac{\pi}{12})$ moving clockwise

and the intensity of the LED light is proportional to the number of oscillators in that particular phase range. For coding that, the following is calculated:

```
double ang = (theta[i][j]*180/pi)/15;
int phase=(int) ang;
for (int j=0;j<24;j++){
  if (phase==j){
    phi[j]++;
  }
}
```

This divides the circle into 24 sections, one for each LED in the ring, and if an oscillator happens to be in a certain section, we increase the count of that section by one. This bins the oscillators to be represented when it has a certain phase by a particular LED. The more oscillators in that bin will then make the LED brighter so that it will be clear when oscillators become phase synchronized. To determine the colors of the LEDs, the following code is implemented:

```
for (int i=0;i<24;i++){
    int red=0;
    int blue=0;
    int green=0;

    if(i<8){
      red=(255-(i*32-1))*phi[i]/64;
      green=(i*32-1)*phi[i]/64;
      blue=0;
    }else if(i<16){
      green=(255-((i-8)*32-1))*phi[i]/64;
      blue=((i-8)*32-1)*phi[i]/64;
      red=0;
    }else {
      blue=phi[i]*(255-(i-16)*32-1)/64;
      red=((i-16)*32-1)*phi[i]/64;
      green=0;
    }
    strip.setPixelColor(i,red,green,blue);
    if(phi[i]==0){
```

```
      strip.setPixelColor(i,0,0,0);
    }
```

For setting the pixel color of LEDs in the matrix depending on the phase of the oscillator, the following lines of code are included:

```
for(int i=0; i<L;i++){
    for(int j=0;j<L;j++){
      int red=0;
      int blue=0;
      int green=0;
      if(theta[i][j]<=2*pi/3){
         green=theta[i][j]*255/(2*pi);
         red=255-theta[i][j]*255/(2*pi/3);
         blue=0;
      }else if(theta[i][j]<=4*pi/3){
         green=255-(theta[i][j]-2*pi/3)*255/(2*pi/3);
         blue=(theta[i][j]-2*pi/3)*255/(2*pi/3);
         red=0;
      }
     else{
         blue=255-(theta[i][j]-4*pi/3)*255/(2*pi/3);
         red=(theta[i][j]-4*pi/3)*255/(2*pi/3);
         green=0;
      }
     matrix.setPixelColor(i+j*L, red, green, blue);
    }
  }
```

This ensures that the oscillator phase is mapped from $[0, 2\pi]$ to $[0, 225]$.

When running the simulation on the Arduino and LED ring, a stopwatch can be used to time how quickly a range of different coupling constants will reach phase coherence. This time to steady state behavior is denoted t_∞. These values are plotted as $ln(\sigma)$ vs $ln(t_\infty)$ in the black circles in Figure 54 and show a linear log-log relationship.

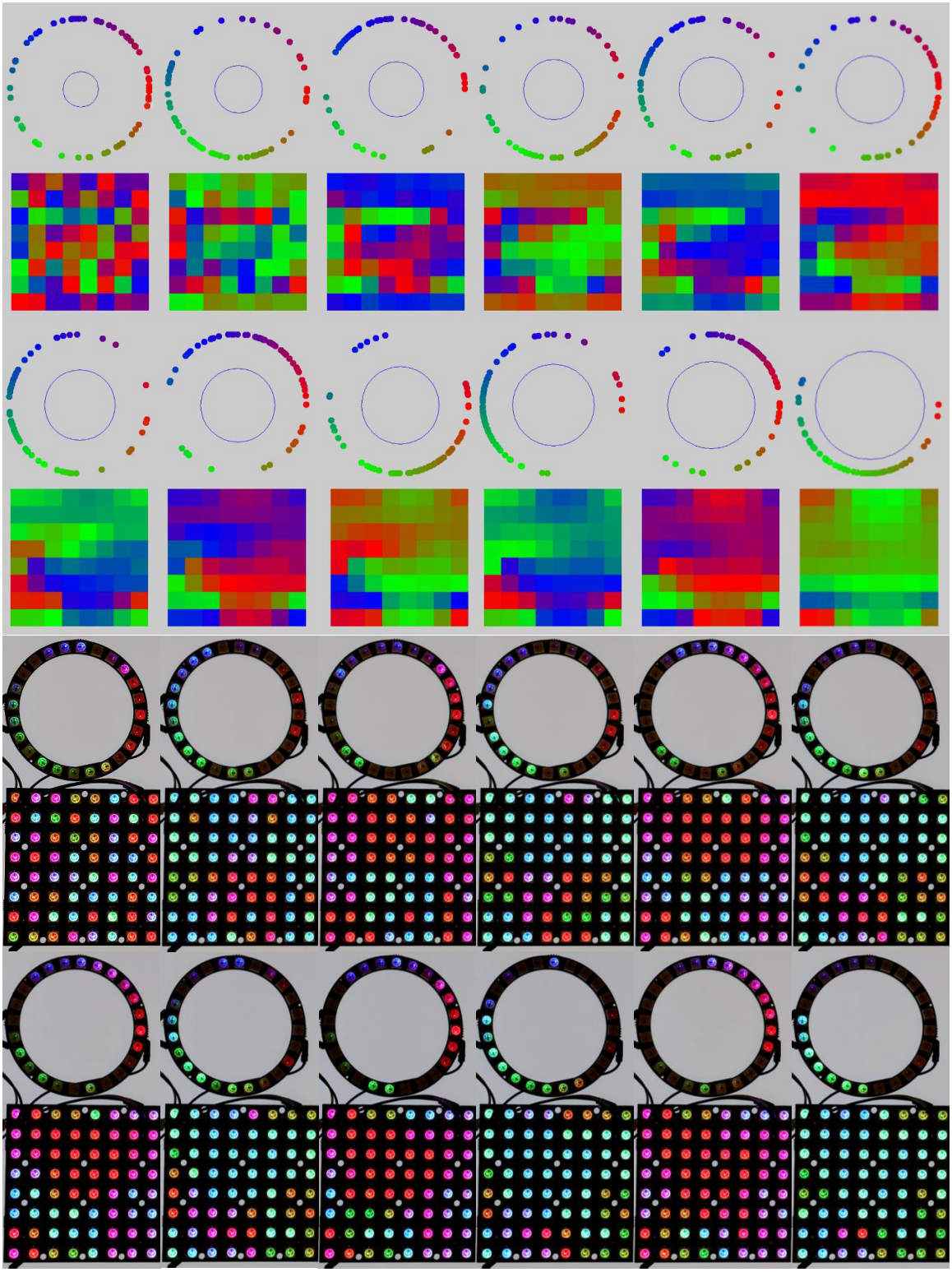

Figure 53: Java applet of the Kuramoto model on an 8×8 LED grid with order parameter shown by the ring. The individual oscillators traverse 0 to 2π ring, from red to green to blue back to red. Bottom. Same set-up on the Arduino 8×8 LED array and 24 LED ring. The simulations are run with nearest neighbor coupling.

5.5.2 Case 2: Nearest Neighbors Topology

Each Kuramoto oscillator obeys the following differential equation for their phase:

$$\begin{aligned}\frac{d\theta_{i,j}}{dt} =&\omega_{i,j} + \sigma\big[\sin(\theta_{i,j+1} - \theta_{i,j}) + \sin(\theta_{i,j-1} - \theta_{i,j}) \\ &+ \sin(\theta_{i+1,j} - \theta_{i,j}) + \sin(\theta_{i-1,j} - \theta_{i,j})\big]\end{aligned} \tag{56}$$

For this case, the network can be imagined as as a two dimensional grid of oscillators with phases $\theta_{i,j}$, where $i, j = 0, 1, ..7$, i describes the row, j describes the column, $i, j = -1 = 7$ and $i, j = 8 = 0$.

Oscillators have natural frequency $\omega_{i,j}$ and coupling strength $\sigma_{i,j}$ with the same ranges as in case 1. In this system, we can express the order parameter to take into account the position:

$$re^{i\phi} = \frac{1}{N}\sum_{j,k=0}^{n-1} e^{i\theta_{j,k}}$$

The difference between these two cases lies in the value of the critical coupling constant σ_{c1} and σ_{c2} which is smaller for case 1 than case 2.

With the Adafruit 8×8 LED matrix and 24 LED ring, synchronization of the oscillators can be observed. Figure 53 shows Java simulations and the LEDs that are controlled by the Arduino for the nearest neighboring coupling case. This simulation takes many periods of the oscillators until the system reaches synchronization. During these intermediate steps, sections of oscillators will begin phase synchronizing with their neighbors which is possible to see in the patches of LEDs of the same color.

Measuring the time to steady state behavior, in this case phase coherence, t_∞ in both the completely connected and the nearest-neighbor coupling case are shown in Figure 54. The completely connected topology reaches coherence faster than the nearest coupling. Also, $ln(\sigma) \propto -ln(t_\infty)$. The time to synchronization in the nearest neighbor coupling case is longer for each value of the coupling parameter σ because each oscillator has fewer connections (4 vs 63 in the completely connected case)

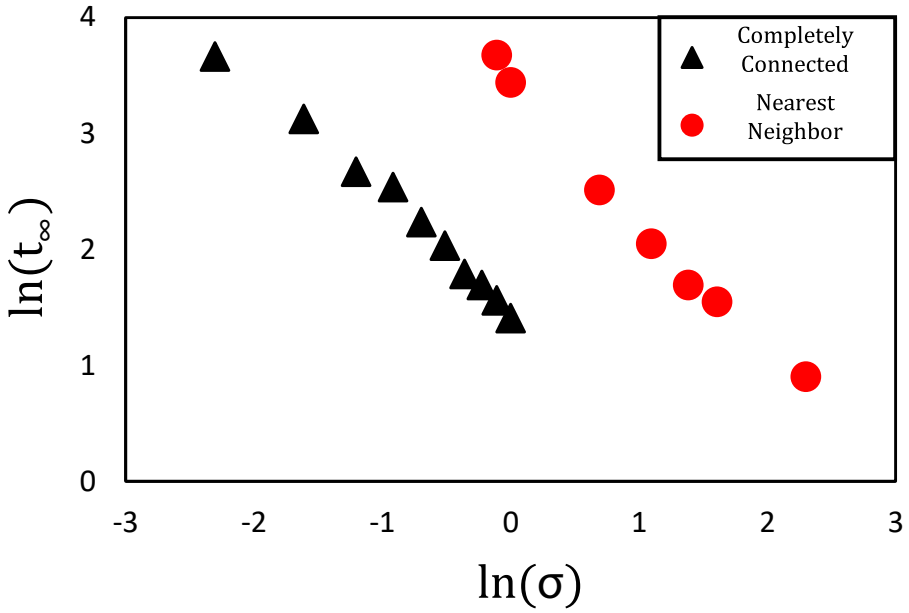

Figure 54: Data of time to synchronization of the LEDs for different coupling strengths for two coupling topologies. There is a shift in time to synchronization from the completely connected case and the nearest neighbors case.

meaning that smaller sections become synchronized enroute to complete phase synchronization. In Figure 52, there remains some spread in the oscillator phase. In some cases, splay states [182] may even emerge where the spread larger and ultimately is spread out more uniformly in the system causing a periodic wave to travel through the oscillators. More information about splay states is Appendix C.

5.5.3 Chimeras from non-local coupling

Chimeras are states of systems that are all composed by identical oscillators with same dynamics but when coupled in space they can develop regions with different dynamics [30]. Typically, systems that exhibit chimera states use non-global coupling [30, 183].

For these simulations, the initial conditions and coupling parameters are taken from Abrams and Strogatz [30] which also includes a feedback parameter α.

$$\frac{d\theta}{dt} = \omega - \int_{-\pi}^{\pi} G(x - x') \sin[\theta(x, t') - \theta(x, t) + \alpha] dx' \tag{57}$$

The coupling kernal is given by

$$G(x) = \frac{1}{2\pi}(1 + A\cos x) \tag{58}$$

where x is the oscillator number and $0 \leq A \leq 1$. This makes oscillators near by more strongly coupled than those farther away. Initial conditions are found by a random distribution of:

$$\theta(x) = 6re^{-0.76x^2} \tag{59}$$

where r is a uniform variable on $[-\frac{1}{2}, \frac{1}{2}]$. This distribution yields oscillators which have small fluctuations at the oscillators near the boundaries making them closer to synchronizing while the other oscillators are random.

Here, even though the oscillators are identical, the dynamics of each oscillator is not. In particular, there are two overall dynamics occurring simultaneously: coherence and decoherence, a type of Chimera state. The 60 LED ring is used to show these dynamics in Figure 55. In this image, the 60 LED ring represents the physical space of the oscillators. In the left hand side of the ring in Fig 55, the oscillators are coherent and the time series show these oscillators are in synch and oscillate at a fixed frequency. This frequency can be measured with a stopwatch or by printing out the values in the serial port. The right hand side shows oscillators that are decoherent and remain so while oscillating at a certain frequency. The images in Fig 55 show the oscillators at 1.7 second intervals. The phase coherent oscillators will remain phase coherent and the decoherent oscillators will remain decoherent for long integration time.

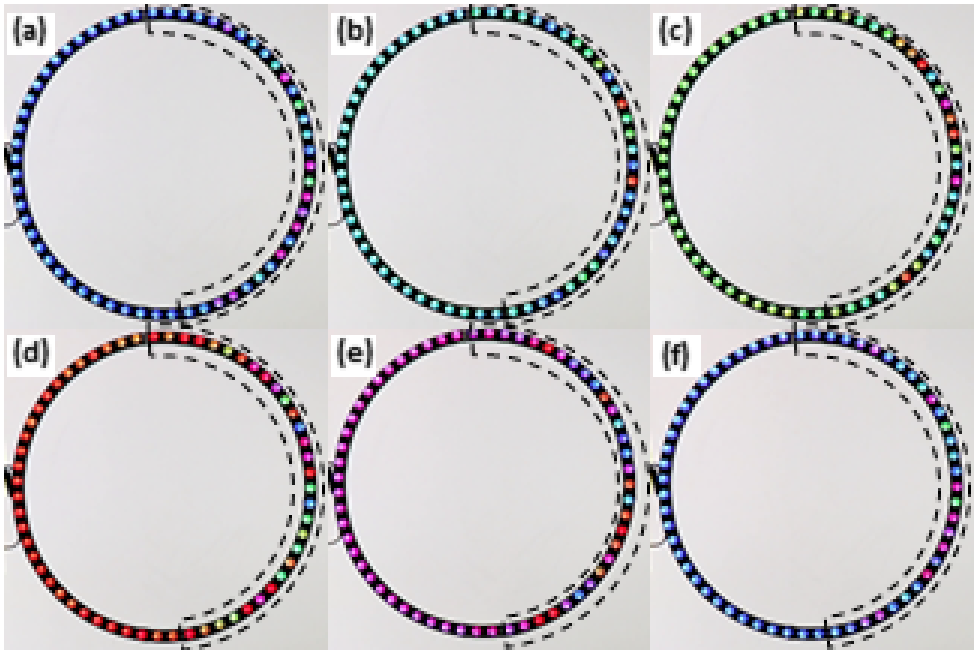

Figure 55: The 60 LED ring running a simulation for chimera dynamics. The color of each LED represents a phase. The LEDs that are in the dashed semi-arcs are represent Kuramoto oscillators that remain decoherent for long period periods of time but are still oscillating in time. The LEDs outside of that arc are Kuramoto oscillators which are phase synchronized. (a-f) show one full period of the coherent state, every 1.7 seconds.

5.6 Discussion

We have presented here a way to implement and study complex systems, including reaction diffusion in one and two dimensions using easy and inexpensive microcontrollers connected with LEDs, touchscreens and web-browser. These open the door to alternative, more interactive ways to study and teach complex systems. It especially allows for activities with a large number of students, each one with their own system or a few working on the same system as we have done in several national and international workshops or with undergraduate summer research students. With the codes presented here, students can easily investigate traveling waves, spiral waves, and how synchronization occurs in coupled oscillator systems. These codes can be used in a laboratory setting having students change parameters such as the coupling strength in order to study how they affect the synchronization for a 2D array of oscillators with nearest neighbor coupling in both physical and phase space through the Adafruit Matrix, ring and LCD displays. In addition, other more complex models can easily be implemented using more advanced microcontrollers.

Students can expand on this set up and are also able to change how the oscillators are coupled in the Arduino sketches for the different models implemented as well as mix the examples up such that the FK or KM include interactions via light or touch, which we did not include here. Furthermore, using other sorts of LED setups, students can create their own networks of oscillators using the same code to simulate the KM, even making unilateral coupling or coupling with different strengths. Also, the 2D KM can also be written to work with the touchscreen if desired and the screens can be set up to better display other sorts of topologies.

Some open projects not presented here include the use of an LED light to be measured by a photoresistor and have coupling to neighboring LED oscillators depend on the value measured by the photoresistor, rather than coupling determined from a set diffusion value as to allow external real random noise be part of the dynamics.

Chapter VI

CONCLUSIONS

This dissertation discussed three different physics research projects which involved the study of dynamics of individual elements coupled together which can create a collective dynamics which is much richer.

The first project proposes an extension to a well studied model. the FitzHugh Nagumo model, which not only makes more different types of dynamics yielding chimeras, but it also is the first model of it's kind to not need non-local coupling or a time delay in order for chimeras to emerge. There are more questions that can be studied that have not been covered within this project including finding a physical system this model can describe. Also of interest is how the change of linear nullcline to intersect with the quintic nullcline will affect the dynamics, which we know is the case for the standard FHN3. Decreasing the slope of this nullcline will introduce more possible stable and unstable fixed points which will affect the collective motion in ways we did not see in the current study.

The second project involved the study of the collective motion of people given certain rules, creating a living cellular automation. Patterns such as spiral waves can appear in this system, however, they can break up due to human randomness such as apprehension, delay, trolling, or misunderstanding the rules. An interesting result of this is that individuals were affected by non-local dynamics despite the rules that were given. This fact can possibily be used in studying other systems of collectitions of people.

The third project, pattern formation of brine shrimp aggregation, is of interest in the active matter community. One positive of this project is the simplicity in

setting up experiment. The patterns that the shrimp form are due to an instability that occurs at high concentration. The concentration also affects wavelength of the pattern. The effects of the temperature on the individual dynamics was also studied, and we showed how temperature affects swim speed and diffusion. At the moment, the effects of temperature on the pattern selection is unknown. There are many open questions that can be studied in the future including the relationship of the extended area and the depth on the patterns that form.

Finally, discussed is one project in setting up and using an Arduino micro-controller to visualize some of the collective dynamics which have been previously studied. While this project did not comprise of new physics, it is work that can be useful for simple interaction with some well known collective dynamics models for the purpose of teaching. The codes that are used in this chapter are included in Appendix D and are ready to be used.

Appendix A

STABILITY ANALYSIS FOR FHN5 COMMENTS

A figure of the eigenvalues for the stability analysis for the FHN can be seen in 56. The decay of the $\mathrm{Im}(\sigma)$ is clear and disappears between $r_b = 0.48$ and $r_b = 0.54$ meaning that there are no more oscillations and perturbations are uniformly stable. As diffusion increase, all eigenvalues also decay with wavenumber, but for the range we investigate, oscillation remain for perturbations decay.

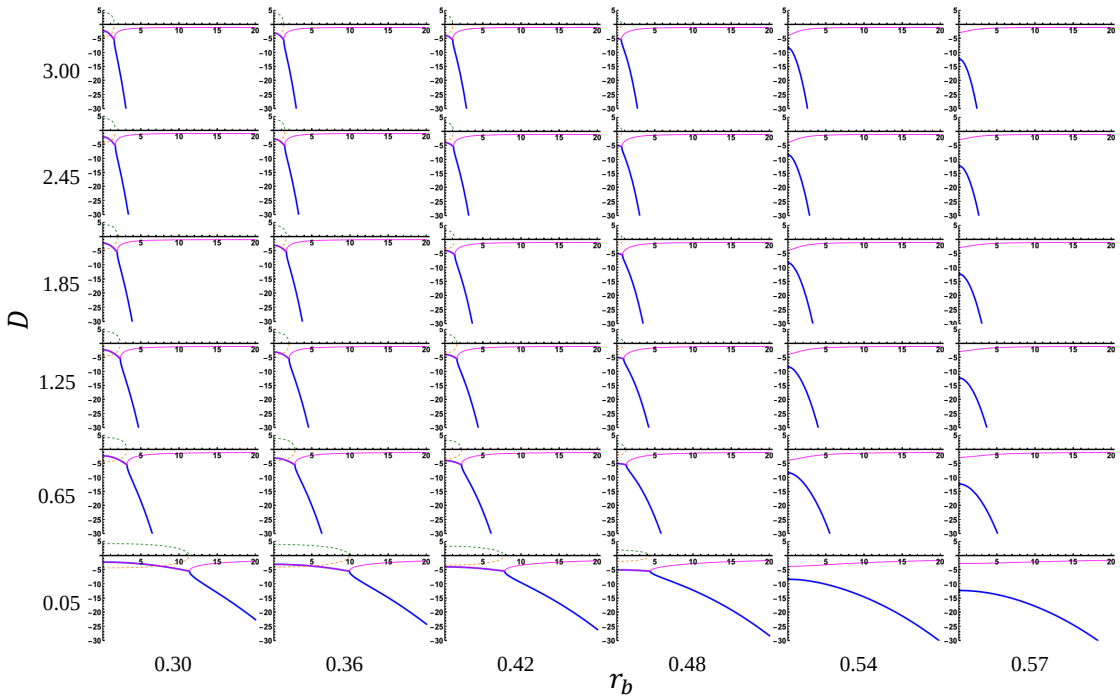

Figure 56: Eigenvalues for the stability analysis for a variety of diffusion and relative basin sizes. The solid lines are the real part of $\mathrm{Re}(\sigma)$ and the dashed lines are $\mathrm{Im}(\sigma)$.

Appendix B

FIT OF THE MEAN SQUARED DISPLACEMENT DATA

This appendix describes the fitting process after tracking multiple shrimp trajectories and calculating the mean squared displacement (MSD) various data sets discussed in 4.

The $\log\langle r^2(t)\rangle$ vs $\log t$ of each data set is plotted and a linear regression is used to fit the data in different sections is the form of $\log\langle r^2(t)\rangle = B\log t + C$. This is determined by picking a cut off point $i \in [0, N]$ in the data set of N points and calculating the coefficient of determination, R^2, for the linear fit before the cutoff and the linear fit after the cutoff. The cutoff which maximizes both R^2 determines B and C for both lines. B is then the power of t in the $\langle r^2(t)\rangle$ vs t fit and C is used as the coefficient where $A = 10^{-C}$.

The experimental data of the MSD and the appropriate linear power law fits for a range of temperatures are shown in Figure 43. The corresponding coefficients and powers are shown in 4.

The powers for the first region are calculated close to 2 as expected for a short term ballistic dynamics. For the second region, the powers are near 1 as expected for long term diffusive dynamics.

Also of note is fitting parameters for the tail end of the MSD. This was use to find a time scale for when shrimp reach the boundary of the container of radius a. However, the MSD data does not approach a constant of a^2 as the shrimp do not remain there. While they do tend to stay there for a long period of time once they reach the boundary, they can also turn back towards the center of the sample. Calculations were cutoff shortly after the MSD fit is no longer ≈ 1.

Table 4: Linear fit values for the $\log\langle r^2(t)\rangle$ vs $\log t$ for different temperatures 6.0, 21.5, 24.5, 27.0, and 45.7°C.

Temperature (°C)	B_1	C_1	B_2	C_2	B_3	C_3
6.0 ± 0.1	1.9269	1.8816	1.2155	1.8975	0.34	0.7795
21.5 ± 0.1	1.7182	1.5648	0.767	1.5391	0.322	0.5794
24.5 ± 0.1	1.7796	1.5059	1.1541	1.6725	0.2836	0.944
27.0 ± 0.1	1.9642	1.1664	1.3412	1.3454	0.4658	0.6364
45.7 ± 0.1	2.1866	0.6328	1.3413	1.0626	0.577	0.7888

Appendix C

COHERENCE OF KURAMOTO OSCILLATORS

This appendix goes into a bit more detail about splay states, which is seen for non-global coupling. First, we discuss the dynamics of the completely connected model and then the nearest neighbor coupling case.

C.1 The Completely Connected Kuramoto Model

The Kuramoto model is a model with motivations in chemical and biological systems such as the behaviors of a network of pacemaker cells in the heart or congregations of flashing fireflies, as well as many others. This model describes the phase dynamics of a system of coupled oscillators with specified natural frequency and in a certain topology[184]. The general form for a sinusoidal coupling relation is as follows:

$$\dot{\theta}_i = \omega_i + \sum_{j=1}^{N} a_{ij} \sin(\theta_j - \theta_i)$$

where $\theta_i \in [0, 2\pi)$ is the phase of oscillator i, ω_i is the natural frequency of oscillator i, σ is a coupling constant, and a_{ij} is an element of the adjacency matrix which gives us whether and how oscillators i and j are connected.

A few assumptions are often made with this model. The first is that the coupling is weak relative to the natural frequency of the oscillators. The second is that the oscillators are near identical–there is not much variation in the natural frequencies. For the purpose of our studies, we will assume the oscillators are all identical.

Winfree proposed that this sort of system can be described using a mean-field approximation where each oscillator is coupled to the collective system. The complex

order parameter, which reimagines the oscillators each traveling around the unit circle in the complex plan can be calculated by:

$$re^{i\phi} = \frac{1}{N}\sum_{j=1}^{N} e^{i\theta_j}$$

where r is a coherence factor yielding 1 when the system is completely phase coherent and 0 when the phases of the system are completely equally distributed from $[0, 2\pi)$ with an average phase of ϕ. This can be used to rewrite the completely connected case so that analytical solutions can be derived[185].

Using this complex order parameter to rewrite the completely connected our equation prominently shows the mean-field characteristic of the model:

$$\theta_i = \omega_i + \sigma r \sin(\phi - \theta_i) \tag{60}$$

Here, it is shown that the strength of the coupling is proportional to the coherence factor r meaning that there is a positive feedback loop among the coherence of the oscillators.

Numerical simulations suggest that the steady state coherence factor r_∞ only

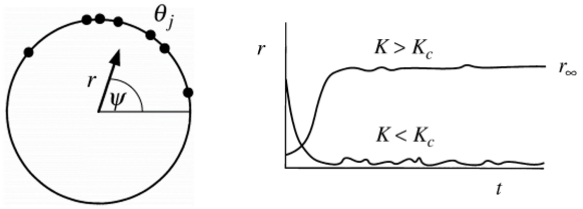

Figure 57: Both taken from [185]. The first shows complex order parameter reimagines the oscillators traveling around a circle. When the systems is phase coherent, the oscillators are clumped at the same phase. r gives the coherence amplitude of the system which is 1 when the oscillators are completely in phase and 0 when they are completely out of phase. The second shows the effect of coupling on the coherence factor in time. For higher than the critical coupling K_c we see a phase transition for spontaneous synchronization

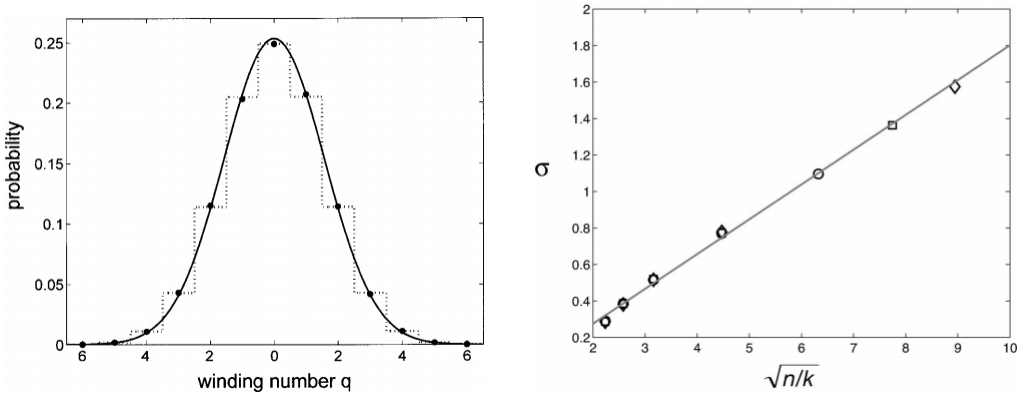

Figure 58: Statistical results for size of basin of attraction for n oscillators in a 1D ring topology taken from [182]. The first plot shows the probability of a certain winding number dominating the steady state for $n = 80$ and $k = 1$ nearest neighbor on each side. The second shows how the relationship between number of oscillators and number of nearest neighbors effect the spread of the Gaussian. The slope of the line is 0.191 ± 0.007 and does not have a known meaning currently.

depends on the coupling K and not the initial conditions. This means that there is a globally attracting state for each value of σ. However, once the topology gets complex inital conditions do have an effect on the attractor and other states are observed such as traveling waves, spiral waves, and chimera states.

C.1.1 Nearest Neighbor Coupling in 1D

Work has been done with the Kuramoto model to find the size of the sync basin for N identical oscillators in a 1D ring topology with k nearest neighbor coupling for a coupling constant greater than the critical coupling. The results show that the distribution of steady state dynamics form a Gaussian centered about a winding number of 0, representing phase coherence in the system. The relationship $\sqrt{N//k}$ effects the spread σ in a linear relationship. Wiley, Strogatz and Girvan offer a minimal explanation for these relationships but leave the question open[182].

Winding numbers are used to re-imagine the ring of coupled oscillators as a chain around a torus, where the oscillators are traveling at a fix angle around the cross-section of the torus. When the system has a winding number of 0, the chain of

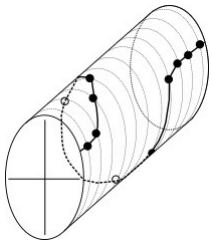

Figure 59: A schematic re-imagining the oscillators traveling around an open torus showing a winding number (the darker line) of 1.

oscillators do not wrap around the cross-section at all. A winding number of q means that the the chain of oscillators wrap through the cross-section q times. There is a handedness to this winding number so that a negative just changes the direction of the wind. Another name for these states where the oscillators act as traveling waves are q-twisted states.

While this gives us information for the relatively basin sizes for systems in 1D, boundaries for basins can be very difficult to find and we still do not have information about where the basins are themselves. Also, we do not have information about these basin sizes in 2D.

C.2 Splay States in 2D

As the complex order parameter will be exactly zero for systems that exhibit waves, we began looking at both 1 and 2D systems using the amplitudes of the discrete Fourier modes to take a look at the dynamics of our system. Similar to the complex order parameter in time plot (Fig 57), we see the same sort of phase transition when the system spontaneously synchronizes to the traveling wave dynamics. Exploring simulations in such a way can give us a quick way of pulling out the initial conditions which lead to these dynamics.

We also repeated the studies of Wiley et al. finding the distribution for q-twisted states for systems of different sizes. Each size simulation was run for 10000 trials, each trial had phases randomly chosen uniformly from $[0 - 2\pi)$.

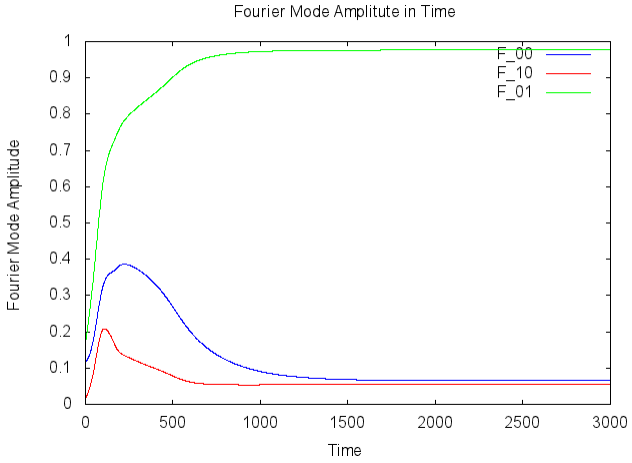

Figure 60: Plots of the Fourier amplitudes in time a 64 2D oscillator systems. The $|F_{00}|$ mode which corresponds to the contribution of flatness of the system, and the $|F_{10}|$ and $|F_{01}|$ modes which corresponds perpendicular traveling waves. The $|F_{01}|$ contribution dominates the steady state dynamics of the system.

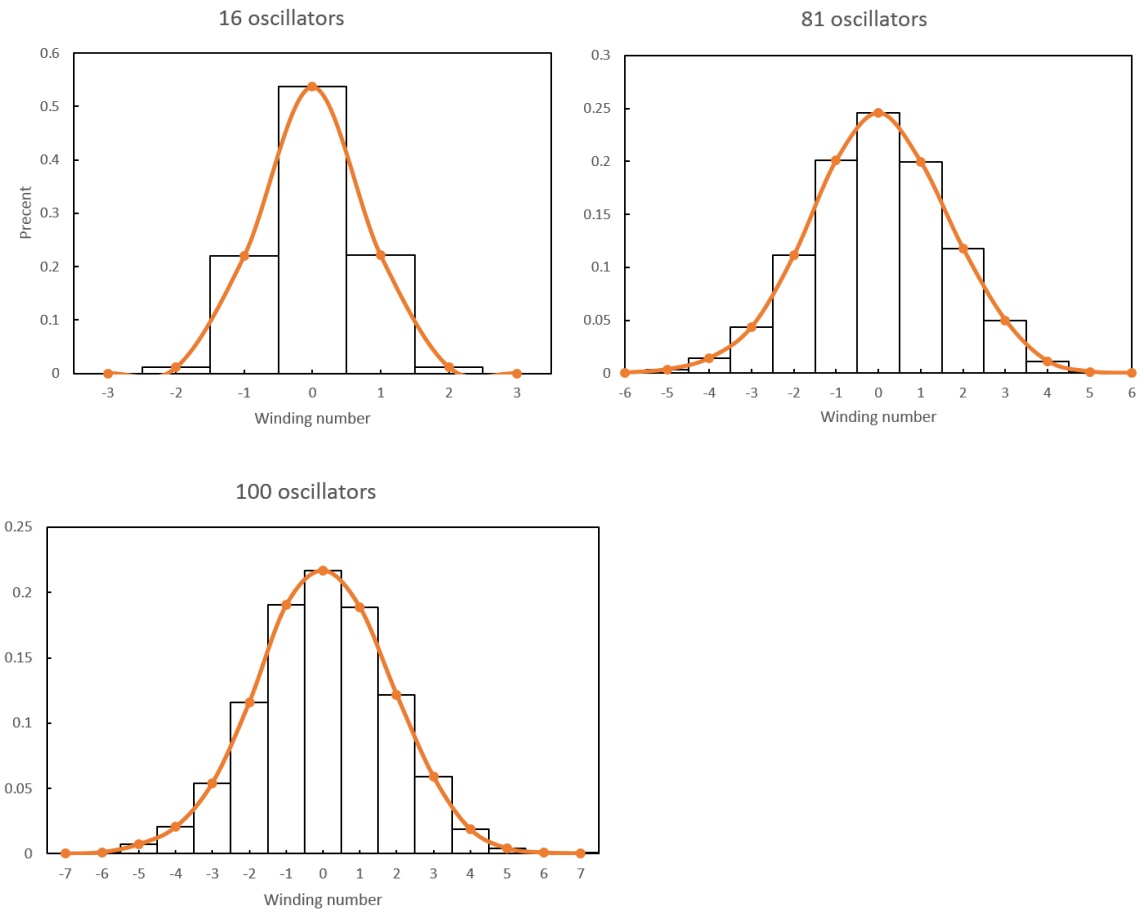

For these q-twisted states, we observed that $r_\infty = 0$ after the critical coupling. We found the same relationship between number of oscillators and the spread of the Gaussian distribution as well. We also began simulation studies on the effect of the coupling constant on the spread of this distribution. Early results show us that the spread does not change. However, there appears to be sets of initial phases which will exhibit different steady state dynamics depending on the coupling. This means that these conditions lie on the edge of two basins of attraction. Future studies will look more closely as these simulations and use perturbation methods to further explore these boundaries. Attempts to do this for 2D systems yielded a much more peaked distribution. For sizes a bit larger ($\sim 16 \times 16$) the appearance of spiral waves and other solutions appear. We will continue to investigate these with more simulations; however they can be computationally intensive for larger systems and these results are very preliminary. There have been studies relating the Kuramoto Model to the XY model, a lattice model. While we have not explored this yet, this looks promising during more extensive studies of the 2D case.

Appendix D

ARDUINO SKETCHES

Here we include the Arduino sketches used for the simulations in Chapter 5.

D.1 Amplitude of a FitzHugh-Nagumo Oscillator

```
//****************************************//
//   This code was written by A.J. Welsh   //
//   and is included in the Supplementary  //
//   Material for Chaos "Simulating Waves, //
//   Chaos and Synchronization with a      //
//   Microcontroller." It was last updated //
//   May 31, 2019.                         //
//   Contact: Andrea.Jayne.Welsh@gmail.com //
//****************************************//



/**************From graphicstest **************/

// IMPORTANT: Adafruit_TFTLCD LIBRARY MUST BE SPECIFICALLY
// CONFIGURED FOR EITHER THE TFT SHIELD OR THE BREAKOUT BOARD.
// SEE RELEVANT COMMENTS IN Adafruit_TFTLCD.h FOR SETUP.

#include <Adafruit_GFX.h>    // Core graphics library
#include <SPI.h>
#include "Adafruit_HX8357.h" //include for touchscreen?
#include <Adafruit_TFTLCD.h> // Hardware-specific library
#include "TouchScreen.h"

// The control pins for the LCD can be assigned to any digital or
// analog pins...but we'll use the analog pins as this allows us to
// double up the pins with the touch screen (see the TFT paint example).
#define LCD_CS A3 // Chip Select goes to Analog 3
#define LCD_CD A2 // Command/Data goes to Analog 2
#define LCD_WR A1 // LCD Write goes to Analog 1
```

```
#define LCD_RD A0 // LCD Read goes to Analog 0

#define LCD_RESET A4 // Can alternately just connect to Arduino's reset pin
/****************************************/



/**************From tftpaint **************/
// These are the four touchscreen analog pins
#define YP A2  // must be an analog pin, use "An" notation!
#define XM A3  // must be an analog pin, use "An" notation!
#define YM 7   // can be a digital pin
#define XP 8   // can be a digital pin

// When using the BREAKOUT BOARD only, use these 8 data lines to the LCD:
// For the Arduino Uno, Duemilanove, Diecimila, etc.:
//   D0 connects to digital pin 8  (Notice these are
//   D1 connects to digital pin 9   NOT in order!)
//   D2 connects to digital pin 2
//   D3 connects to digital pin 3
//   D4 connects to digital pin 4
//   D5 connects to digital pin 5
//   D6 connects to digital pin 6
//   D7 connects to digital pin 7
// For the Arduino Mega, use digital pins 22 through 29
// (on the 2-row header at the end of the board).

// For the Arduino Due, use digital pins 33 through 40
// (on the 2-row header at the end of the board).
//   D0 connects to digital pin 33
//   D1 connects to digital pin 34
//   D2 connects to digital pin 35
//   D3 connects to digital pin 36
//   D4 connects to digital pin 37
//   D5 connects to digital pin 38
//   D6 connects to digital pin 39
//   D7 connects to digital pin 40

// These are the four touchscreen analog pins
#define YP A2  // must be an analog pin, use "An" notation!
#define XM A3  // must be an analog pin, use "An" notation!
#define YM 7   // can be a digital pin
```

```
#define XP 8   // can be a digital pin



#define TS_MINX 110
#define TS_MINY 80
#define TS_MAXX 900
#define TS_MAXY 940

// For better pressure precision, we need to know the resistance
// between X+ and X- Use any multimeter to read it
// For the one we're using, its 300 ohms across the X plate
//TouchScreen ts = TouchScreen(XP, YP, XM, YM, 300);



// The display uses hardware SPI, plus #9 & #10
#define TFT_RST -1  // dont use a reset pin, tie to arduino RST if you like
#define TFT_DC 9
#define TFT_CS 10

Adafruit_HX8357 tft = Adafruit_HX8357(TFT_CS, TFT_DC, TFT_RST);
TouchScreen ts = TouchScreen(XP, YP, XM, YM, 300);



// Assign human-readable names to some common 16-bit color values:
#define  BLACK   0x0000
#define BLUE    0x001F
#define RED     0xF800
#define GREEN   0x07E0
#define CYAN    0x07FF
#define MAGENTA 0xF81F
#define YELLOW  0xFFE0
#define WHITE   0xFFFF



/***************************************/



float w;
float vt;
float v;
```

```
float actionPotential[480];

float a = 2.5;
float b = -1*a;
float c=0;
float I=0;
float epsilon =1;
float dt = 0.05;
int t=0;



void setup(void) {
  Serial.begin(9600);
  Serial.println(F("TFT LCD test"));
  tft.begin(HX8357D);
  tft.fillScreen(HX8357_BLACK);
  //intial conditions of the oscillator
  v = 6;
  w = 5;

  #ifdef USE_ADAFRUIT_SHIELD_PINOUT
    Serial.println(F("Using Adafruit 2.8\" TFT Arduino Shield Pinout"));
  #else
    Serial.println(F("Using Adafruit 2.8\" TFT Breakout Board Pinout"));
  #endif
    Serial.print("TFT size is ");
    Serial.print(tft.width());
    Serial.print("x");
    Serial.println(tft.height());
}



void loop(){

    calc(); //calls the method that makes the calculations
    drawAP(255);//to draw the pulse
    drawAP(0);//to clear the pulse
    copy();//copies it over to the next location so we can see the history of the phases of the oscillator

/**************From Breakouttouchpaint **************/
  // Retrieve a point
```

```
  TSPoint p = ts.getPoint();

  // we have some minimum pressure we consider 'valid'
  // pressure of 0 means no pressing!
  if (p.z < MINPRESSURE || p.z > MAXPRESSURE) {
     return;
  }
  Serial.print("\tPressure = ");
  Serial.println(p.z);
  v+=p.z/130;//touch will add a at most 10 at min 0 to the voltage
/*****************************************************/
}



void drawAP(int color2) {
  //Draws the pulse to the screen
  uint16_t color=tft.color565(color2,color2,color2);
  for(int i=0;i<480;i++){
    double y1=(actionPotential[i]+6)*20+50;
    double y2=(actionPotential[i+1]+6)*20+50;
    tft.drawLine(y2, i*2+2,y1, i*2, color);
 }
}



double calc(){
    //calculates the current value of the oscillator
    vt = v + dt * (-1*v*(v-a)*(v-b)-w);
    w = w + dt * epsilon*(v-c*w);
    actionPotential[0]=vt;
}

double copy(){
  for(int i=479;i>0;i--){
      actionPotential[i]=actionPotential[i-1];
  }
  v = vt;
}
```

D.2 A Ring of Coupled FitzHugh-Nagumo Oscillators with and without Photocell

```
//**************************************//
//   This code was written by A.J. Welsh   //
//   and is included in the Supplementary  //
//   Material for Chaos "Simulating Waves, //
//   Chaos and Synchronization with a      //
//   Microcontroller." It was last updated //
//   May 31, 2019.                         //
//   Contact: Andrea.Jayne.Welsh@gmail.com //
//**************************************//

#include <Adafruit_NeoPixel.h>
#include <Adafruit_GFX.h>

#ifndef PSTR
 #define PSTR
#endif

#define PIN 6

int photocellPin = 0;     // the cell and 10K pulldown are connected to a0
int photocellReading;     // the analog reading from the sensor divider

float a = 0.1;
float b = 0.5;
float epsilon = 0.0095;
float delta = 0;
float dt = 0.4;
float dx2 = 1;
double impulse=0;
double min=100;
boolean photocell=false; //set true if using a photocell



float w[60];
float vt[60];
float v[60];
float vr[60];
```

```
int i = 0;


Adafruit_NeoPixel strip = Adafruit_NeoPixel(60, 6, NEO_GRB + NEO_KHZ800);



void setup(){
  strip.begin();
  //Initial conditions for a wave propagating in one direction
  do{
    vt[i] = 0;
    w[i] = 0;
    v[i] = 0;
    vr[i] = 0;
    i = i +1;
  } while(i < 60);
  i = 8;
  do{
    v[i] = 0.5;
    i = i + 1;
  }while(i < 13);


  i = 3;
  do{
    w[i]= 0.6;
    i = i + 1;
  }while(i < 5);
  Serial.begin(9600);
  Serial.println(dx2);
}



void loop(){
  if(photocell){
  //Reading in the photocell to find the min value it is recording
  photocellReading = analogRead(photocellPin);
  if(photocellReading<min){
    min=photocellReading;
  }

  //Printing current photocell value and min value to serial
  Serial.print("Analog reading = ");
```

```
Serial.println(photocellReading);
Serial.println(min);
i = 0 ;
//start reading the photocell after the simulation has begun
if(t>20){
  //scale the photocell reading so that it is within model range to act as an impulse
  impulse =-(photocellReading-1023)/130.;
  Serial.print("impulse = ");
  Serial.println(impulse);
  Serial.println(t);
}
}
//integration of the FHN model
//the impulse will affect the integration of oscillator zero
vt[i] = v[i] + dt * (v[i]*(a-v[i])*(v[i]-1)-w[i]) + dt *(v[i+1]+v[59]-2 * v[i])/dx2+impulse;
w[i] = w[i] + dt * epsilon*(b*v[i]-w[i]-delta);
Serial.println(vt[0]);
i = 59 ;
vt[i] = v[i] + dt * (v[i]*(a-v[i])*(v[i]-1)-w[i]) + dt *(v[0]+v[i-1]-2 * v[i])/dx2;
w[i] = w[i] + dt * epsilon*(b*v[i]-w[i]-delta);
i = 1;
do {
  vt[i] = v[i] + dt * (v[i]*(a-v[i])*(v[i]-1)-w[i]) + dt *(v[i+1]+v[i-1]-2 * v[i])/dx2;
  w[i] = w[i] + dt * epsilon*(b*v[i]-w[i]-delta);
  i = i+1;
}while (i < 59);
i = 0;
do {
  v[i] = vt[i];
  i = i+1;
} while ( i < 60);

//determine color of each LED dependant on v of each oscillator
i = 0;
do {
  vr[i] = floor(100 * v[i]);
  i = i+1;
} while ( i < 60);

i = 0;
do {
```

```
    strip.setPixelColor(i, vr[i],0,0);
    i = i+1;
  } while ( i < 60);
  //display LEDs
  strip.setBrightness(30);
  strip.show();
}
```

D.3 A 2D Array of Coupled FitzHugh-Nagumo Oscillators

```
//****************************************//
//   This code was written by A.J. Welsh   //
//   and is included in the Supplementary  //
//   Material for Chaos "Simulating Waves, //
//   Chaos and Synchronization with a      //
//   Microcontroller." It was last updated //
//   May 31, 2019.                         //
//   Contact: Andrea.Jayne.Welsh@gmail.com //
//****************************************//



/**************From graphicstest **************/

// IMPORTANT: Adafruit_TFTLCD LIBRARY MUST BE SPECIFICALLY
// CONFIGURED FOR EITHER THE TFT SHIELD OR THE BREAKOUT BOARD.
// SEE RELEVANT COMMENTS IN Adafruit_TFTLCD.h FOR SETUP.

#include <Adafruit_GFX.h>    // Core graphics library
#include <SPI.h>
#include "Adafruit_HX8357.h"
#include <Adafruit_TFTLCD.h> // Hardware-specific library
#include <TouchScreen.h>

// The control pins for the LCD can be assigned to any digital or
// analog pins...but we'll use the analog pins as this allows us to
// double up the pins with the touch screen (see the TFT paint example).
#define LCD_CS A3 // Chip Select goes to Analog 3
#define LCD_CD A2 // Command/Data goes to Analog 2
#define LCD_WR A1 // LCD Write goes to Analog 1
```

```
#define LCD_RD A0 // LCD Read goes to Analog 0

#define LCD_RESET A4 // Can alternately just connect to Arduino's reset pin
/****************************************/



/**************From tftpaint **************/
// These are the four touchscreen analog pins
#define YP A2  // must be an analog pin, use "An" notation!
#define XM A3  // must be an analog pin, use "An" notation!
#define YM 7   // can be a digital pin
#define XP 8   // can be a digital pin

// When using the BREAKOUT BOARD only, use these 8 data lines to the LCD:
// For the Arduino Uno, Duemilanove, Diecimila, etc.:
//   D0 connects to digital pin 8  (Notice these are
//   D1 connects to digital pin 9   NOT in order!)
//   D2 connects to digital pin 2
//   D3 connects to digital pin 3
//   D4 connects to digital pin 4
//   D5 connects to digital pin 5
//   D6 connects to digital pin 6
//   D7 connects to digital pin 7
// For the Arduino Mega, use digital pins 22 through 29
// (on the 2-row header at the end of the board).

// For the Arduino Due, use digital pins 33 through 40
// (on the 2-row header at the end of the board).
//   D0 connects to digital pin 33
//   D1 connects to digital pin 34
//   D2 connects to digital pin 35
//   D3 connects to digital pin 36
//   D4 connects to digital pin 37
//   D5 connects to digital pin 38
//   D6 connects to digital pin 39
//   D7 connects to digital pin 40

// These are the four touchscreen analog pins
#define YP A2  // must be an analog pin, use "An" notation!
#define XM A3  // must be an analog pin, use "An" notation!
#define YM 7   // can be a digital pin
```

```
#define XP 8   // can be a digital pin



#define TS_MINX 110
#define TS_MINY 80
#define TS_MAXX 900
#define TS_MAXY 940

// For better pressure precision, we need to know the resistance
// between X+ and X- Use any multimeter to read it
// For the one we're using, its 300 ohms across the X plate
//TouchScreen ts = TouchScreen(XP, YP, XM, YM, 300);



// The display uses hardware SPI, plus #9 & #10
#define TFT_RST -1  // dont use a reset pin, tie to arduino RST if you like
#define TFT_DC 9
#define TFT_CS 10

Adafruit_HX8357 tft = Adafruit_HX8357(TFT_CS, TFT_DC, TFT_RST);
TouchScreen ts = TouchScreen(XP, YP, XM, YM, 300);



// Assign human-readable names to some common 16-bit color values:
#define  BLACK   0x0000
#define BLUE    0x001F
#define RED     0xF800
#define GREEN   0x07E0
#define CYAN    0x07FF
#define MAGENTA 0xF81F
#define YELLOW  0xFFE0
#define WHITE   0xFFFF

/***************************************/

//Determines how big each interaction with the touchscreen is
#define BOXSIZE 40
#define PENRADIUS 15

int Nx=64;
int Ny=96;
```

```
int cellSize=5;
float w[64][96];
float vt[64][96];
float v[64][96];

float a = 2.2;
float b = 1;
float d=0.05;
float epsilon = 1;
float delta = 0;
float dt = 0.06;
float dx2 = 1.2;

double max=0;
double min=0;



void setup(void) {
  Serial.begin(9600);
  Serial.println(F("TFT LCD test"));

  //Initial conditions to get a spiral wave
  for (int i=30;i<35;i++){
    for (int j=0;j<37;j++){
      v[i][j] = 6;
      w[i][j] = 0;
    }
  }
  for( int i=36;i<38;i++){
    for (int j=0;j<30;j++){
     w[i][j] = 5;
    }
  }

  /**************From graphicstest **************/
  #ifdef USE_ADAFRUIT_SHIELD_PINOUT
    Serial.println(F("Using Adafruit 2.8\" TFT Arduino Shield Pinout"));
  #else
    Serial.println(F("Using Adafruit 2.8\" TFT Breakout Board Pinout"));
  #endif
```

```
    Serial.print("TFT size is ");
    Serial.print(tft.width());
    Serial.print("x");
    Serial.println(tft.height());
    tft.begin(HX8357D);
    Serial.begin(9600);
    Serial.println(dx2);
    tft.fillScreen(HX8357_BLACK);
    /***************************************/
}

//define the pressure that the touchscreen will measure
#define MINPRESSURE 1
#define MAXPRESSURE 1000

void loop(){
  int t=0;
  do{
    testFilledRects();

    //look here for how to add touch
    digitalWrite(13, HIGH);
    TSPoint p = ts.getPoint();
    digitalWrite(13, LOW);

    // if sharing pins, you'll need to fix the directions of the touchscreen pins
    //pinMode(XP, OUTPUT);
    pinMode(XM, OUTPUT);
    pinMode(YP, OUTPUT);
    //pinMode(YM, OUTPUT);

    // we have some minimum pressure we consider 'valid'
    // pressure of 0 means no pressing!
    if (p.z > MINPRESSURE && p.z < MAXPRESSURE) {
      // scale from 0->1023 to tft.width
      p.x = map(p.x, TS_MINX, TS_MAXX, tft.width(), 0);
      p.y = map(p.y, TS_MINY, TS_MAXY, tft.height(), 0);

      //Bins the pixels on the screen into different boxes to determine which cells
      //of the similation you are touching and will be activated
      int xt=p.x/cellSize;
```

```
      int yt=p.y/cellSize;
      vt[xt][yt]=3;
      v[xt][yt]=3;

      for(int i=0;i<PENRADIUS;i++){
        for(int j=0;j<20;j++){
          xt=(i*cos(j*PI/10)+p.x)/cellSize;
          yt=(j*sin(j*PI/10)+p.y)/cellSize;
          vt[xt][yt]=3;
          v[xt][yt]=3;
        }
      }

    Serial.println(vt[xt][yt]);
    Serial.println(v[xt][yt]);

    }
    t++;
  }while(true);
}



void testFilledRects() {
  for (int i=0;i<Nx;i++) {
    for(int j=0;j<Ny;j++){
        //calculate the value of each oscillator i,j
        double x=calc(i,j);
        if (x>max){
          max=x;
            Serial.println(max);
          }
        if(x<min){
          min=x;
            Serial.println(min);
        }

        //determine colors from the value of each oscillator.
        //We use a color scheme similar to the BZ reaction
        int green;
        int blue;
```

```
        green= (int)((x+6)*57/6+91);
        blue= (int)((x+6)*86/6+33);
        uint16_t color3=tft.color565(205,green,blue);
        tft.fillRect(i*cellSize,j*cellSize,cellSize,cellSize, color3);
      }
  }
  for(int i=0;i<Nx;i++){
    for(int j=0;j<Ny;j++){
      copy(i,j);
    }
  }
}

//Integration of an oscillator with periodic boundary conditions and four nearest neighbor coupling
double calc(int p, int q){
  if(p==0&&q>0&&q<Ny-1){
    vt[p][q] = v[p][q] + dt * (-1*v[p][q]*(v[p][q]-a)*(v[p][q]+a)-w[p][q])
    + dt/dx2 *(2*v[1][q]+v[p][q-1]+v[p][q+1]-4 * v[p][q]);
    w[p][q] = w[p][q] + dt * epsilon*(b*v[p][q]-d*w[p][q]-delta);
  }
  else if(q==0&&p>0&&p<Nx-1){
    vt[p][q] = v[p][q] + dt * (-1*v[p][q]*(v[p][q]-a)*(v[p][q]+a)-w[p][q])
    + dt/dx2 *(v[p+1][q]+v[p-1][q]+2*v[p][1]-4 * v[p][q]);
    w[p][q] = w[p][q] + dt * epsilon*(b*v[p][q]-d*w[p][q]-delta);
  }
  else if(p==Nx-1&&q>0&&q<Ny-1){
    vt[p][q] = v[p][q] + dt * (-1*v[p][q]*(v[p][q]-a)*(v[p][q]+a)-w[p][q])
    + dt/dx2 *(2*v[Nx-2][q]+v[p][q-1]+v[p][q+1]-4 * v[p][q]);
    w[p][q] = w[p][q] + dt * epsilon*(b*v[p][q]-d*w[p][q]-delta);
  }else if(q==Ny-1&&p>0&&p<Nx-1){
    vt[p][q] = v[p][q] + dt * (-1*v[p][q]*(v[p][q]-a)*(v[p][q]+a)-w[p][q])
    + dt/dx2 *(v[p+1][q]+v[p-1][q]+2*v[p][Ny-2]-4 * v[p][q]);
    w[p][q] = w[p][q] + dt * epsilon*(b*v[p][q]-d*w[p][q]-delta);

  }
  //BC for four corners
  else if(p==0&&q==0){
    vt[p][q] = v[p][q] + dt * (-1*v[p][q]*(v[p][q]-a)*(v[p][q]+a)-w[p][q])
    + dt/dx2 *(2*v[0][1]+2*v[1][0]-4 * v[p][q]);
    w[p][q] = w[p][q] + dt * epsilon*(b*v[p][q]-d*w[p][q]-delta);
  }
```

```
  else if(p==0&&q==Ny-1){
    vt[p][q] = v[p][q] + dt * (-1*v[p][q]*(v[p][q]-a)*(v[p][q]+a)-w[p][q])
    + dt/dx2 *(2*v[0][Ny-2]+2*v[1][Ny-1]-4 * v[p][q]);
    w[p][q] = w[p][q] + dt * epsilon*(b*v[p][q]-d*w[p][q]-delta);
  }
  else if(p==Nx-1&&q==0){
    vt[p][q] = v[p][q] + dt * (-1*v[p][q]*(v[p][q]-a)*(v[p][q]+a)-w[p][q])
    + dt/dx2 *(2*v[Nx-2][0]+2*v[Nx-1][1]-4 * v[p][q]);
    w[p][q] = w[p][q] + dt * epsilon*(b*v[p][q]-d*w[p][q]-delta);
  }
  else if(p==Nx-1&&q==Ny-1){
    vt[p][q] = v[p][q] + dt * (-1*v[p][q]*(v[p][q]-a)*(v[p][q]+a)-w[p][q])
    + dt/dx2 *(2*v[Nx-1][Ny-2]+2*v[Nx-2][Ny-1]-4 * v[p][q]);
    w[p][q] = w[p][q] + dt * epsilon*(b*v[p][q]-d*w[p][q]-delta);
  }
  else{
    vt[p][q] = v[p][q] + dt * (-1*v[p][q]*(v[p][q]-a)*(v[p][q]+a)-w[p][q])
    + dt /dx2*(v[p+1][q]+v[p-1][q]+v[p][q+1]+v[p][q-1]-4 * v[p][q]);
    w[p][q] = w[p][q] + dt * epsilon*(b*v[p][q]-d*w[p][q]-delta);
  }
  return vt[p][q];
}



double copy(int p, int q){
  v[p][q] = vt[p][q];
}
```

D.4 A Ring of Coupled Fenton-Karma Oscillators

```
//****************************************//
//   This code was written by A.J. Welsh   //
//   and is included in the Supplementary  //
//   Material for Chaos "Simulating Waves, //
//   Chaos and Synchronization with a      //
//   Microcontroller." It was last updated //
//   May 31, 2019.                         //
//   Contact: Andrea.Jayne.Welsh@gmail.com //
//****************************************//
```

```
#include <Adafruit_NeoPixel.h>
#include <Adafruit_GFX.h>

#ifndef PSTR
 #define PSTR
#endif

#define PIN 6

float a = 0.1;
float b = 0.5;
float epsilon = 0.0095;
//float gamma = 1;
float delta = 0;
float dt = 0.2;
float dx2 = 2.5;

int j;

float u[120];
float ut[120];
float ur[120];
float vt[120];
float v[120];
float vr[120];
float f[120];
int i = 0;
int nx=120;
float ifi,iso,isi,xpp,xqq;
Adafruit_NeoPixel strip = Adafruit_NeoPixel(60, 6, NEO_GRB + NEO_KHZ800);



void setup(){
  strip.begin();
  //Initial conditions for alternans
  do{
    vt[i] = 0;
    u[i] = -85.0;
    ut[i] = 0;
    ur[i] = 0;
```

```
    v[i] = 1;
    vr[i] = 0;
    f[i]=1;
    i = i +1;
  }while(i < 120);
  i = 30;
  do{
    u[i] = 0.;
    v[i+20]=0;
    i = i + 1;
  }while(i < 50);
  Serial.begin(9600);
  Serial.println(dx2);

}



void loop(){
  while(true){
    i = 1 ;
    u[nx]=u[1];
    u[0]=u[nx-1];
    do {
      xpp=0;
      xqq=0;
      if(u[i] > -72.0) {
        xpp = 1;
      }if(u[i] > -79.5) {
        xqq = 1;
      }

      //integration of variables and calculation of currents
      v[i] = v[i] + dt*((1.0-xpp)*(1-v[i])/(1000.0*xqq+19.2*(1-xqq))-0.3*xpp*v[i]);
      f[i]  = f[i] + dt*((1.0-xpp)*(1.0-f[i])/11.0-xpp*f[i]/667.0);
      ifi   = -0.04*v[i]*(15-u[i])*(u[i]+72)*xpp;
      iso   = (u[i]+85.0)*(1.0-xpp)/8.3+2.0*xpp;
      isi   = -(1.0+((exp(u[i]*0.1)-exp(-u[i]*0.1))/(exp(u[i]*0.1)+exp(-u[i]*0.1))))*f[i]/0.897;
      ut[i] = u[i]+(u[i+1]+u[i-1]-2*u[i])*dt/dx2-dt*(ifi+iso+isi);
      i=i+1;
    } while (i < nx);
    Serial.println(ut[i]);
```

```
    i = 0;
    //determining color of pixel by the u variable
    do {
      u[i]=ut[i];
      ur[i] = floor(2.4 * (ut[i]+85));
      i = i+1;
    } while ( i < 120);
    i = 0;
    j = 0;
    do {
      strip.setPixelColor(i, ur[j],0,0);
      i = i+1;
      j = j + 2;
    } while ( i < 61);
    strip.show();
  }
}
```

D.5 A 2D Array of Coupled Kuramoto Oscillators

```
//****************************************//
//   This code was written by A.J. Welsh   //
//   and is included in the Supplementary  //
//   Material for Chaos "Simulating Waves, //
//   Chaos and Synchronization with a      //
//   Microcontroller." It was last updated //
//   May 31, 2019.                         //
//   Contact: Andrea.Jayne.Welsh@gmail.com //
//****************************************//


#include <Adafruit_NeoPixel.h>
#include <Adafruit_GFX.h>
#include <Adafruit_NeoMatrix.h>
#include <Adafruit_NeoPixel.h>
#include <Gaussian.h>
#ifndef PSTR
 #define PSTR
#endif
```

```
#define PIN 6

Adafruit_NeoPixel strip = Adafruit_NeoPixel(24, 6, NEO_GRB + NEO_KHZ800);
Adafruit_NeoMatrix matrix = Adafruit_NeoMatrix(8, 8, 0,
  NEO_MATRIX_TOP     + NEO_MATRIX_RIGHT +
  NEO_MATRIX_COLUMNS + NEO_MATRIX_PROGRESSIVE,
  NEO_GRB            + NEO_KHZ800);

const int L=8;
const float pi=4*atan(1.);
double adj[L][L][L][L];
double theta[L][L];
double theta_old[L][L];
double sum[L][L];
double w[L][L];
int phi[24];
int M;
int t=0;

//can change the coupling here to different values
double g=1;
//If using nearest neighbor coupling, pick true
//If using all-to-all coupling, pick false.
boolean NN= true;

const uint16_t colors[] = {
  matrix.Color(255, 0, 0), matrix.Color(0, 255, 0), matrix.Color(0, 0, 255) };

void setup() {
  Gaussian myGaussian(3*pi/2,pi/2);
  for(int i =0; i<L; i++){
    for(int j=0;j<L;j++){
      int random2 = random(0,6280);
      //Initial phases are picked randomly between 0 and 6.280
      theta[i][j]=(double)random2/1000;
      //We pick natural frequency from a Gaussian distribution between pi/2 and 3pi/2
      w[i][j]=myGaussian.random();
   }
 }
 for (int i=0; i<24;i++){
   phi[i]=0;
```

```
 }
 strip.begin();
 strip.show();
 strip.setBrightness(100);
 matrix.begin();
 matrix.setBrightness(20);
 matrix.setTextColor(colors[0]);
}
void loop(){
 for(int i=0;i<24;i++){
   phi[i]=0;
  }

  for (int i=0;i<L;i++){
    for (int j=0;j<L;j++){
     theta_old[i][j]=theta[i][j];
    }
  }
  for (int i=0; i<L;i++){
    for (int j=0;j<L;j++){
     sum[i][j]=0;
       if(NN){
         //nearest neighbors for each oscillator
         if(i==0&&j>0&&j<7){
           sum[i][j]=sin(theta_old[0][j+1]-theta_old[i][j])+sin(theta_old[0][j-1]-theta_old[i][j])
           +sin(theta_old[7][j]-theta_old[i][j])+sin(theta_old[1][j]-theta_old[i][j]);
         } else if(j==0&&i>0&&i<7){
           sum[i][j]=sin(theta_old[i+1][0]-theta_old[i][j])+sin(theta_old[i-1][0]-theta_old[i][j])
           +sin(theta_old[i][7]-theta_old[i][j])+sin(theta_old[i][1]-theta_old[i][j]);
         } else if(i==7&&j>0&&j<7){
           sum[i][j]=sin(theta_old[7][j+1]-theta_old[i][j])+sin(theta_old[7][j-1]-theta_old[i][j])
           +sin(theta_old[0][j]-theta_old[i][j])+sin(theta_old[6][j]-theta_old[i][j]);
         } else if(j==7&&i>0&&i<7){
           sum[i][j]=sin(theta_old[i+1][7]-theta_old[i][j])+sin(theta_old[i-1][7]-theta_old[i][j])
           +sin(theta_old[i][0]-theta_old[i][j])+sin(theta_old[i][6]-theta_old[i][j]);
         }
        //BC for four corners
          else if(i==0&&j==0){
            sum[i][j]=sin(theta_old[0][1]-theta_old[i][j])+sin(theta_old[1][0]-theta_old[i][j])
            +sin(theta_old[7][0]-theta_old[i][j])+sin(theta_old[0][7]-theta_old[i][j]);
         }else if(i==0&&j==7){
```

```
        sum[i][j]=sin(theta_old[0][0]-theta_old[i][j])+sin(theta_old[7][7]-theta_old[i][j])
        +sin(theta_old[0][6]-theta_old[i][j])+sin(theta_old[1][7]-theta_old[i][j]);
    } else if(i==7&&j==0){
        sum[i][j]=sin(theta_old[0][0]-theta_old[i][j])+sin(theta_old[7][7]-theta_old[i][j])
        +sin(theta_old[6][0]-theta_old[i][j])+sin(theta_old[7][1]-theta_old[i][j]);
     }else if(i==7&&i==7){
        sum[i][j]=sin(theta_old[6][7]-theta_old[i][j])+sin(theta_old[7][6]-theta_old[i][j])
        +sin(theta_old[7][0]-theta_old[i][j])+sin(theta_old[0][7]-theta_old[i][j]);
     }else{
      sum[i][j]=sin(theta_old[i+1][j]-theta_old[i][j])+sin(theta_old[i-1][j]-theta_old[i][j])
      +sin(theta_old[i][j+1]-theta_old[i][j])+sin(theta_old[i][(j-1)]-theta_old[i][j]);
     }
  }else{
       //Completely connected model
       for(int q=0;q<L;q++){
         for(int p=0;p<L;p++){
           sum[i][j]+=sin(theta_old[q][p]-theta_old[i][j]);
         }
       }
  }

 //integration of the Kuramoto model for each oscillator
theta[i][j]=theta[i][j]+.005*(w[i][j]+g*sum[i][j]);

 //we make sure the phases stay in range
while(theta[i][j]>2*pi){
  theta[i][j]=theta[i][j]-2*pi;
}while(theta[i][j]<0){
  theta[i][j]=theta[i][j]+2*pi;
}

//we bin the phases of each oscillator into a particular sector which will be represented by an
//LED in the ring
double ang = (theta[i][j]*180/pi)/15;
int phase=(int) ang;
for (int j=0;j<24;j++){
  if (phase==j){
    //We count how many oscillators are in each sector
    phi[j]++;
  }
}
```

```
 }
}


for(int i=0; i<L;i++){
  for(int j=0;j<L;j++){
    int red=0;
    int blue=0;
    int green=0;
    //we determine each LED color depending on it's phase at this time step. The phases go from
    //red to green to blue.
    if(theta[i][j]<=2*pi/3){
       green=theta[i][j]*255/(2*pi);
       red=255-theta[i][j]*255/(2*pi/3);
       blue=0;
    }else if(theta[i][j]<=4*pi/3){
       green=255-(theta[i][j]-2*pi/3)*255/(2*pi/3);
       blue=(theta[i][j]-2*pi/3)*255/(2*pi/3);
       red=0;
    }   //.5pi-1.5pi
   else{
       blue=255-(theta[i][j]-4*pi/3)*255/(2*pi/3);
       red=(theta[i][j]-4*pi/3)*255/(2*pi/3);
       green=0;
    }
   matrix.setPixelColor(i+j*L, red, green, blue);
  }
}


for (int i=0;i<24;i++){
  int red=0;
  int blue=0;
  int green=0;

  //we determine how bright each LED is in the ring depending on how many oscillators are in that sector.
  //The color comes from the color determined in the matrix
  if(i<8){
    red=(255-(i*32-1))*phi[i]/64;
    green=(i*32-1)*phi[i]/64;
    blue=0;
  }else if(i<16){
    green=(255-((i-8)*32-1))*phi[i]/64;
```

```
      blue=((i-8)*32-1)*phi[i]/64;
      red=0;
    }else {
      blue=phi[i]*(255-(i-16)*32-1)/64;
      red=((i-16)*32-1)*phi[i]/64;
      green=0;
    }
    strip.setPixelColor(i,red,green,blue);
    if(phi[i]==0){
      strip.setPixelColor(i,0,0,0);
    }
  }
 //we display the LEDs at each time step.
  matrix.show();
  strip.show();
}
```

D.6 Chimeras in a Ring of Coupled Kuramoto Oscillators

```
//****************************************//
//   This code was written by A.J. Welsh   //
//   and is included in the Supplementary  //
//   Material for Chaos "Simulating Waves, //
//   Chaos and Synchronization with a      //
//   Microcontroller." It was last updated //
//   May 31, 2019.                         //
//   Contact: Andrea.Jayne.Welsh@gmail.com //
//****************************************//
#include <Adafruit_NeoPixel.h>
#include <Adafruit_GFX.h>

#ifndef PSTR
 #define PSTR
#endif

#define PIN 6

int N=60;
float alpha = 0.18;
```

```
double pi= 4.*atan(1.);
float dt = 0.25;
float dx2 = 1;
float beta=0;
//double gamma=0.005;
float A=0.3;

float w[60];
float theta_o[60];
float theta[60];
float sum[60];
int i = 0;
int red, blue, green;
float avefreq=.1;

Adafruit_NeoPixel strip = Adafruit_NeoPixel(60, 6, NEO_GRB + NEO_KHZ800);



void setup(){
  strip.begin();
  //Determines initial conditions of each oscillator
  //in order to have Chimeras
  //adapted from D. M. Abrams and S. H. Strogatz, Phys Rev Lett93, 174102 (2004)

  for(int i=0;i<N;i++){
      double ki=((double)i/(double)N-.5)*2*pi;
      theta_o[i]=6*((double)random(0,100)/100-.5)*exp(-.76*ki*ki);
      w[i]=avefreq;
  }
  Serial.begin(9600);
  Serial.println(dx2);
}



void loop(){
  for(int i=0;i<N; i++){
     for(int j=0;j<N;j++){
       //Determines non-local coupling for each oscillator
       double ki=((double)i/(double)N-.5)*2*pi;
       double kj=((double)j/(double)N-.5)*2*pi;
       if(i!=j){
```

```
        sum[i]+=1/(2*pi)*(1+A*cos(ki-kj))*sin(theta_o[j]-theta_o[i]+alpha);
      }
    }
    //Integration of the Kuramoto oscillators
    theta[i]=theta_o[i]+dt*(w[i]-beta*sum[i]);
    sum[i]=0;
    //Keeps phases in range
    while(theta[i]>2*pi){
      theta[i]-=2*pi;
    }while(theta[i]<0){
      theta[i]+=2*pi;
    }
  }

   for(int i=0;i<N;i++){
       theta_o[i]=theta[i];
       //Determines Color of Each Oscillator
       if(theta[i]<=2*pi/3){
         green=(int)floor(theta[i]*255/(2*pi/3));
         red=255-(int)floor(theta[i]*255/(2*pi/3));
         blue=0;
       }else if (theta[i]<=4*pi/3){
         blue=(int)floor((theta[i]-2*pi/3)*255/(2*pi/3));
         green=255-(int)floor((theta[i]-2*pi/3)*255/(2*pi/3));
         red=0;
       }else{
         red=(int)floor((theta[i]-4*pi/3)*255/(2*pi/3));
         blue=255-(int)floor((theta[i]-4*pi/3)*255/(2*pi/3));
         green=0;
       }
       strip.setPixelColor(i, red,blue,green);

   }

  //Displays the LEDs
  strip.setBrightness(10);
  strip.show();

}
```

References

[1] C. Gray. "Synchronous oscillations in neuronal systems: Mechanisms and functions". In: *Journal of Computational Neuroscience* 1.1-2 (1994), pp. 11–38 (cit. on p. 1).

[2] L. Glass. "Synchronization and rhythmic processes in physiology". In: *Nature* 410.6825 (2001), pp. 277–284 (cit. on p. 1).

[3] M. A. Watanabe, F. H. Fenton, S. J. Evans, H. M. Hastings, and A. Karma. "Mechanisms for Discordant Alternans". In: *Journal of Cardiovascular Electrophysiology* 12.2 (2003), pp. 196–206 (cit. on p. 1).

[4] K. Y. Tsang, R. E. Mirollo, S. H. Strogatz, and K. Wiesenfeld. "Dynamics of a globally coupled oscillator array". In: *Physica D: Nonlinear Phenomena* 48.1 (1991), pp. 102 –112 (cit. on p. 1).

[5] S. H. Strogatz. *The Mathematical Structure of the Human Sleep-wake Cycle*. New York, NY, USA: Springer-Verlag New York, Inc., 1986. ISBN: 0-387-17176-2 (cit. on p. 1).

[6] S. H. Strogatz. "Human sleep and circadian rhythms: a simple model based on two coupled oscillators". In: *Journal of Mathematical Biology* 25.3 (1987), pp. 327–347 (cit. on p. 1).

[7] J Buck and E Buck. "Synchronous Fireflies". In: *Sci Am* 234 (5 1976), pp. 74–9, 82–5 (cit. on p. 1).

[8] S. H. Strogatz, D. M. Abrams, A McRobie, B Eckhardt, and E. Ott. "Theoretical mechcanics: crowd synchrony on the Millennium Bridge". In: *Nature* (2005), pp. 43–4 (cit. on p. 1).

[9] Z. Néda, E. Ravasz, T. Vicsek, Y. Brechet, and A. Barabsi. "Physics of the rhythmic applause". In: *Physical Review E - Statistical Physics, Plasmas, Fluids, and Related Interdisciplinary Topics* 61.6 B (2000), pp. 6987–6992 (cit. on p. 1).

[10] H. E. Scharfman. In: *Curr Neurol Neurosci Rep* 7 (4 2007), 348354 (cit. on p. 1).

[11] K. Sanderson. "Millennium Bridge wobble explained". In: *Nature News* (2008) (cit. on pp. 1, 96).

[12] S. Landy. “Mapping the Universe”. In: *Scientific American* 280 (6 1999), pp. 38–45 (cit. on p. 2).

[13] R. Bagnold. *The Physics of Blown Sand and Desert Dunes*. London: Methuen, 1941 (cit. on p. 2).

[14] K. Libbrecht. *The art of the snowflake: A photographic album*. New York: Voyageur Press, 2007 (cit. on p. 2).

[15] M. Cross and H. Greenside. *Pattern Formation and Dynamics in Nonequilibrium Systems*. Cambridge University Press, 2009 (cit. on pp. 2, 5).

[16] A. M. Turing. “The chemical basis of morphogenesis”. In: *Phil. Trans. R. Soc. London* 237 (1952) (cit. on p. 2).

[17] R FitzHugh. “Impulses and physiological states in theoretical models of nerve membrane”. In: *Biophys J* 1 (1961), 445466 (cit. on pp. 3, 94, 96, 104).

[18] J. Nagumo, S. Arimoto, and S. Yoshizawa. “An active pulse transmission line simulating nerve axon”. In: *PIRE* 50.10 (1962), pp. 2061–2070 (cit. on pp. 3, 4, 94, 96).

[19] E. Meron. *Nonlinear Physics of Ecosystems*. CRC Press, 2015 (cit. on pp. 3, 5).

[20] B. van der Pol Jun. D.Sc. “LXXXVIII. On “relaxation-oscillations””. In: *The London, Edinburgh, and Dublin Philosophical Magazine and Journal of Science* 2.11 (1926), pp. 978–992 (cit. on p. 4).

[21] G. R. Mines. “On dynamic equilibrium in the heart”. In: *J Physiol* 46.4-5 (1913), pp. 349–383 (cit. on pp. 4, 105, 114).

[22] T Gedeon and L Glass. “Continuity of resetting curves for FitzHugh-Nagumo equations on the circle”. In: *Fields Inst. Commun.* (1999), pp. 225–236 (cit. on p. 4).

[23] K. Hall and L. Glass. “How to Tell a Target from a Spiral: The Two Probe Problem”. In: *Phys. Rev. Lett.* 82 (25 1999), pp. 5164–5167 (cit. on p. 4).

[24] T. Quail, A. Shrier, and L. Glass. “Spatial Symmetry Breaking Determines Spiral Wave Chirality”. In: *Phys. Rev. Lett.* 113 (15 2014), p. 158101 (cit. on p. 4).

[25] J. M. Davidenko, A. V. Pertsov, R. Salomonsz, W. Baxter, and J. Jalife. "Stationary and drifting spiral waves of excitation in isolated cardiac muscle". In: *Nature* 355.6358 (1992), p. 349 (cit. on pp. 4, 27, 110).

[26] S. Takagi, A. Pumir, D. Pazó, I. Efimov, V. Nikolski, and V. Krinsky. "Unpinning and Removal of a Rotating Wave in Cardiac Muscle". In: *Phys. Rev. Lett.* 93 (5 2004), p. 058101 (cit. on p. 4).

[27] J. M. Rogers and A. D. McCulloch. "A collocation-Galerkin finite element model of cardiac action potential propagation". In: *IEEE Trans. Biomed. Eng.* 41 (8 1994) (cit. on p. 4).

[28] S. P. Hastings. "On the Existence of Homoclinic and Periodic Orbits for the Fitzhugh-Nagumo Equations". In: *Q J Math* 27.1 (1976), pp. 123–134 (cit. on pp. 6, 104).

[29] Y. Kuramoto and D. Battogtokh. "Coexistence of Coherence and Incoherence in Nonlocally Coupled Phase Oscillators: A Soluble Case". In: *J. Nonlin. Phenom. Complex Syst.* 5 (2002) (cit. on pp. 9, 11, 12).

[30] D. M. Abrams and S. H. Strogatz. "Chimera States for Coupled Oscillators". In: *Phys Rev Lett* 93 (17 2004), p. 174102 (cit. on pp. 9, 11, 12, 123).

[31] Homer. *Illiad* (cit. on p. 9).

[32] D. M. Abrams and S. H. Strogatz. "Chimera States in a Ring of Nonlocally Coupled Oscillators". In: *International Journal of Bifurcation and Chaos* 16.01 (2006), pp. 21–37. eprint: `https://doi.org/10.1142/S0218127406014551` (cit. on p. 11).

[33] G. C. Sethia, A. Sen, and F. M. Atay. "Clustered Chimera States in Delay-Coupled Oscillator Systems". In: *Phys. Rev. Lett.* 100 (14 2008), p. 144102 (cit. on p. 11).

[34] O. E. Omel'chenko, Y. L. Maistrenko, and P. A. Tass. "Chimera States: The Natural Link Between Coherence and Incoherence". In: *Phys. Rev. Lett.* 100 (4 2008), p. 044105 (cit. on p. 11).

[35] C. R. Laing. "Chimera states in heterogeneous networks". In: *Chaos: An Interdisciplinary Journal of Nonlinear Science* 19.1 (2009), p. 013113. eprint: `https://doi.org/10.1063/1.3068353` (cit. on p. 11).

[36] S. Shima and Y. Kuramoto. "Rotating spiral waves with phase-randomized core in nonlocally coupled oscillators". In: *Phys. Rev. E* 69 (3 2004), p. 036213 (cit. on p. 11).

[37] M. Panaggio and D. Abrams. "Chimera states on a flat torus". In: *Phys. Rev. Lett.* 110.9 (2013) (cit. on p. 11).

[38] P. M.J. and D. Abrams. "Chimera states on the surface of a sphere". In: *Phys. Rev. E* 91 (2 2015) (cit. on p. 11).

[39] T.-W. Ko and G. B. Ermentrout. "Partially locked states in coupled oscillators due to inhomogeneous coupling". In: *Phys. Rev. E* 78 (1 2008), p. 016203 (cit. on p. 11).

[40] D. M. Abrams, R. Mirollo, S. H. Strogatz, and D. A. Wiley. "Solvable Model for Chimera States of Coupled Oscillators". In: *Phys. Rev. Lett.* 101 (8 2008), p. 084103 (cit. on p. 11).

[41] Y. Zhu, Z. Zheng, and Y. Yang Junzhong. "Chimera states on complex networks". In: *Phys. Rev. E* 89 (2 2014) (cit. on p. 11).

[42] In: *Front. Phys.* 13 (2018) (cit. on p. 12).

[43] "When Nonlocal Coupling between Oscillators Becomes Stronger: Patched Synchrony or Multichimera States". In: *Phys. Rev. Lett.* 110 (2013) (cit. on pp. 12, 20).

[44] S. Guo, Q. Dai, H. Cheng, H. Li, F. Xie, and J. Yang. "Spiral wave chimera in two-dimensional nonlocally coupled Fitzhugh-Nagumo systems". In: *Chaos, Solitons & Fractals* (2018) (cit. on p. 13).

[45] Y. C. Ji and F. H. Fenton. "Numerical solutions of reaction-diffusion equations: Application to neural and cardiac models". In: *Am J Phys* 84.8 (2016), pp. 626–638 (cit. on pp. 18, 105, 106).

[46] M. A. Watanabe, F. H. Fenton, S. J. Evans, H. M. Hastings, and A. Karma. "Mechanisms for discordant alternans". In: *J Cardiovasc Electrophysiol* 12.2 (2001), pp. 196–206 (cit. on pp. 20, 96, 114).

[47] J. Nolasco and R. W. Dahlen. "A graphic method for the study of alternation in cardiac action potentials." In: *J Appl Physiol* 25.2 (1968), pp. 191–196 (cit. on pp. 20, 96, 114).

[48] M. Guevara, G Ward, A Shrier, and L Glass. "Electrical alternans and period doubling bifurcations". In: *IEEE Comp Cardiol* 562 (1984), pp. 167–170 (cit. on pp. 20, 96, 114).

[49] J. M. Pastore, S. D. Girouard, K. R. Laurita, F. G. Akar, and D. S. Rosenbaum. "Mechanism linking T-wave alternans to the genesis of cardiac fibrillation". In: *Circulation* 99.10 (1999), pp. 1385–1394 (cit. on pp. 20, 96, 114).

[50] I. Uzelac, Y. C. Ji, D. Hornung, J. Schröder-Scheteling, S. Luther, R. A. Gray, E. M. Cherry, and F. H. Fenton. "Simultaneous quantification of spatially discordant alternans in voltage and intracellular calcium in langendorff-perfused rabbit hearts and inconsistencies with models of cardiac action potentials and Ca transients". In: *Front Physiol* 8 (2017), p. 819 (cit. on pp. 20, 96).

[51] E. Cytrynbaum and J. P. Keener. "Stability conditions for the traveling pulse: Modifying the restitution hypothesis". In: *Chaos* 12.3 (2002), pp. 788–799 (cit. on p. 21).

[52] A. M. Zhabotinsky. "Periodical oxidation of malonic acid in solution (a study of the Belousov reaction kinetics)". In: *Biofizika* 9 (1964), pp. 306–311 (cit. on pp. 27, 112).

[53] N. Gorelova and J Bureš. "Spiral waves of spreading depression in the isolated chicken retina". In: *J Neurobiol* 14.5 (1983), pp. 353–363 (cit. on pp. 27, 110).

[54] A. Okubo. "Dynamical aspects of animal grouping: Swarms, schools, flocks, and herds". In: *Advances in Biophysics* 22 (1986), pp. 1 –94 (cit. on pp. 33, 66).

[55] B. Zhou, X. Wang, and X. Tang. "Understanding Collective Crowd Behaviors: Learning a Mixture Model of Dynamic Pedestrian-Agents". In: (2012) (cit. on p. 33).

[56] C. Arita and A. Schadschneider. "The Dynamics of Waiting: The Exclusive Queueing Process". In: *Transportation Research Procedia* 2 (2014), pp. 87–95 (cit. on p. 33).

[57] J. L. Silverberg, M. Bierbaum, J. P. Sethna, and I. Cohen. "Collective Motion of Moshers at Heavy Metal Concerts". In: *Phys. Rev. Lett.* 110 (22 2013), p. 228701 (cit. on p. 33).

[58] I. Farkas, D. Helbing, and T. Vicsek. "Social behaviour: Mexican waves in an excitable medium". In: *Nature* 419.6903 (2002), 131–132 (cit. on pp. 33, 34, 39).

[59] K. Moe, C. Werner, J. Abildson, and N. Utica. "A computer model of atrial fibrillation". In: *Am Heart J* 67 (1964), pp. 200–220 (cit. on p. 34).

[60] S. Wolfram. “Statistical mechanics of cellular automata”. In: *Rev. Mod. Phys.* 55 (106 1983) (cit. on pp. 34, 37).

[61] S. Wolfram. *A New Kind of Science*. Champaign, IL: Wolfram Media, 2002 (cit. on pp. 34, 37).

[62] M. Gardner. “Mathematical Games The fantastic combinations of John Conway’s new solitaire game ”life””. In: *Scientific American* 223 (4 1970), 120123 (cit. on pp. 34, 35).

[63] W. J.E. P. Lammers, H. Mirghani, B. Stephen, S. Dhanasekaran, A. Wahab, M. A. H. Al Sultan, and F. Abazer. “Patterns of electrical propagation in the intact pregnant guinea pig uterus”. In: *American Journal of Physiology - Regulatory, Integrative and Comparative Physiology* 294.3 (2008), R919–R928. eprint: `http://ajpregu.physiology.org/content/294/3/R919.full.pdf` (cit. on p. 38).

[64] A. A. P. Leao. “Spreading Depression of Activity in the Cerebral Cortex”. In: *Journal of Neurophysiology* 7 (1944), pp. 359–390 (cit. on p. 38).

[65] D. B. Nandini, S. B. Bhavana, B. S. Deepak, and R. Ashwini. “Paediatric Geographic Tongue: A Case Report, Review and Recent Updates”. In: *Journal of Clinical and Diagnostic Research* (2 2016) (cit. on p. 38).

[66] T Sano and T. Sawanobori. “Mechanism Initiating Ventricular Fibrillation Demonstrated in Cultured Ventricular Muscle Tissue”. In: *Circulation Research* 26.2 (1970), pp. 201–210. eprint: `http://circres.ahajournals.org/content/26/2/201.full.pdf` (cit. on p. 38).

[67] E. M. Cherry and F. H Fenton. “Visualization of spiral and scroll waves in simulated and experimental cardiac tissue”. In: *New Journal of Physics* 10 (2008) (cit. on p. 38).

[68] L. Stefan, F. H. Fenton, B. G. Kornreich, A. Squires, P. Bittihn, D. Hornung, M. Zabel, J. Flanders, A. Gladuli, L. Campoy, E. Cherry, G. Luther, G. Hasenfuss, V. I. Krinsky, A Pumir, R. F. Gilmour Jr, and E. Bodenschatz. “Low-energy control of electrical turbulence in the heart”. In: *Nature* 475 (2011), 235–239 (cit. on p. 38).

[69] T. Nomura and L. Glass. “Entrainment and termination of reentrant wave propagation in a periodically stimulated ring of excitable media”. In: *Phys. Rev. E* 53 (6 1996), pp. 6353–6360 (cit. on p. 38).

[70] C. for Disease Control and N. C.f.H. S. Prevention. *Multiple Cause of Death 1999-2017 on CDC WONDER Online Database, released December, 2018.* accessed Jul 10, 2019 (cit. on p. 38).

[71] G. Kastberger, E. Schmelzer, and I. Kranner. "Social Waves in Giant Honeybees Repel Hornets". In: *PLoS ONE* 3.9 (2008) (cit. on p. 39).

[72] N. Wiener and A. Rosenblueth. "The mathematical formulation of the problem of conduction of impulses in a network of connected excitable elements, specifically in cardiac muscle". In: *Arch. Inst. Cardio. México* 16 (1946), pp. 205–265 (cit. on p. 40).

[73] J. M. Davidenko, A. V. Pertsov, R. Salomonsz, W. Baxter, and J. Jalife. *Stationary and drifting spiral waves of excitation in isolated cardiac muscle.* 1992 (cit. on p. 40).

[74] M. Heron. "Deaths: Leading causes for 2014". In: *National Vital Statistics Reports* 65.5 (2016) (cit. on p. 40).

[75] T. L. Hedrick. "Software techniques for two- and three-dimensional kinematic measurements of biological and biomimetic systems". In: *Bioinspir Biomim* 3.3 (2008) (cit. on pp. 44, 49, 85).

[76] J. Tyson and J. Keener. "Singular perturbation theory of travelling waves in excitable media". In: *Physica D* (1988) (cit. on p. 47).

[77] A. Cavagna and I. Giardina. "Bird Flocks as Condensed Matter". In: *Annual Review of Condensed Matter Physics* 5.1 (2014), pp. 183–207 (cit. on pp. 66, 75).

[78] P. Reimann. "Brownian motors: noisy transport far from equilibrium". In: *Physics Reports* 361 (2002) (cit. on p. 66).

[79] B. M. Friedrich and F. Julicher. "Chemotaxis of sperm cells". In: *Proceedings of the National Academy of Sciences* 104 (33 2007) (cit. on p. 66).

[80] P. M. Kareiva and N. Shigesada. "Analyzing insect movement as a correlated random walk". In: *Oecologia* 56 (2-3 1983), 234238 (cit. on p. 66).

[81] P. Romanczuk, M. Bar, W. Ebeling, B. Lindner, and S.-G. Lutz. "Active Brownian Particles. From Individual to Collective Stochastic Dynamics". In: *Eur Phys J Special-Topics* (2012) (cit. on p. 66).

[82] Y. Hatwalne, S. Ramaswamy, M. Rao, and R. A. Simha. "Rheology of Active-Particle Suspensions". In: *Phys. Rev. Lett.* 92 (11 2004), p. 118101 (cit. on p. 66).

[83] E. Fodor and M. C. Marchetti. "The statistical physics of active matter: From self-catalytic colloids to living cells". In: *Physica A: Statistical Mechanics and its Applications* 504 (2018). Lecture Notes of the 14th International Summer School on Fundamental Problems in Statistical Physics, pp. 106 –120 (cit. on pp. 66, 69).

[84] V. Schaller, C. Weber, C. Semmrich, E. Frey, and A. R. Bausch. "Polar patterns of driven filaments". In: 467 (2010), 7377 (cit. on p. 66).

[85] Y. Sumino, K. H. Nagai, Y. Shitaka, D. Tanaka, K. Yoshikawa, H. Chaté, and K. Oiwa. "Large-scale vortex lattice emerging from collectively moving microtubules". In: *Nature* 483 (2012), pp. 448–452 (cit. on p. 66).

[86] J. Krause and G. D. Ruxton. *Living in Groups*. Oxford University Press, USA, 2002 (cit. on p. 66).

[87] J. Perrin. "Lagitation moleculaire et le mouvement brownien". In: *J. Phys. Theor. Appl.* 9 (1 1910) (cit. on p. 67).

[88] M. G. Raizen and T. Li. "The measurement Einstein deemed impossible". In: *Physics Today* 68 (1 2015) (cit. on p. 67).

[89] G. Redner, M. Hagan, and A. Baskaran. "Structure and dynamics of a phase-separating active colloid fluid". In: *Phys. Rev. Lett.* 110 (2013) (cit. on pp. 67, 70).

[90] M. Schnitzer. In: *Phys. Rev. E* (1993), pp. 2553–68 (cit. on p. 69).

[91] H. Berg. *E. coli in Motion*. Springer, 2003 (cit. on p. 69).

[92] M. E. Cates and J. Tailleur. "Motility-Induced Phase Separation". In: *Annu. Rev. Condens. Matter Phys.* 6 (2015), pp. 219–244 (cit. on pp. 69, 70).

[93] Y. Fily and M. Marchetti. "Athermal phase separation of self-propelled particles with no alignment". In: *Phys. Rev. Lett.* 108 (2012) (cit. on p. 70).

[94] M. Cates and J. Tailleur. "When are active Brownian particles and run-and-tumble particles equivalent? Consequences for motility-induced phase separation". In: *Europhys. Lett.* 101 (2013) (cit. on p. 70).

[95] H. Wager. "On the effect of gravity upon movements and aggregation of *Eugena virdis*, Ehrb., and other mirc-organisms". In: *Phil. Trans. R. Soc. Lond.* 201 (1911), pp. 333–390 (cit. on p. 70).

[96] T. Pedley and J. Kessler. "Bioconvection". In: *Sci. Prog.* 76 (1992), pp. 105–123 (cit. on p. 71).

[97] M. Bees and N. Hill. In: *J. Exp. Bio.* 200 (1997), pp. 1515–1526 (cit. on pp. 71, 74).

[98] N. Hill and T. Pedley. "Bioconvection". In: *Fluid Dyn. Res.* 37 (2005), pp. 1–20 (cit. on p. 71).

[99] U. Kils. "Formation of Micropatches by Zooplankton-Driven Microturbulences". In: *Bull. Mar. Sci.* 53.1 (1993), pp. 160–169 (cit. on p. 71).

[100] W. Press, S. Teukolsky, W. Vetterling, and B. Flannery. *Numerical Recipes in FORTRAN. The Arti of Scientific Computing*. Cambridge: Cambridge University Press, 1992 (cit. on p. 74).

[101] T. Vicsek and A. Zafeiris. "Collective Motion". In: *Physics Reports* 517.3 (2012), pp. 71 –140 (cit. on p. 74).

[102] C. Reynolds. "Flocks, herds and schools: A distributed behavioral model". In: *SIGGRAPH Comput. Graph.* 21.4 (1987), pp. 25–34 (cit. on p. 75).

[103] S. R.S. J. Neill and J. M. Cullen. "Experiments on whether schooling by their prey affects the hunting behaviour of cephalopods and fish predators". In: *J. Zool.* 172 (1974), pp. 549–569 (cit. on p. 75).

[104] M. Milinski and E. Curio. "Untersuchungen zur Selektion durch Rauber gegen Verinzelung der Beute". In: *Z. Tierpsychol* 37 (1975), pp. 400–402 (cit. on p. 75).

[105] M. Milinski. "Experiments on the selection of predators against spatial oddity of their prey". In: *Z. Tierpsychol* 43 (3 1977), pp. 311–325 (cit. on p. 75).

[106] W. L. Morgan and D. A. Ritz. "Effect of prey density and hunger state on capture of krill, Nyctiphanes australis Sars, by Australian salmon, Arripis trutta (Bloch & Schneider)". In: *Fish. Biol.* 24 (1984), pp. 51–58 (cit. on p. 75).

[107] O. Ohguchi. "Experiments on the selection against colour oddity of water fleas by three-spined sticklebacks". In: *Z. Tierpsychol* 47 (1978), pp. 254–267 (cit. on p. 75).

[108] C. Drewes. *Artemia Franciscana*. http://www.zool.iastate.edu/c-drewes/. Accessed: 2016-04-03 (cit. on pp. 75, 76, 80).

[109] G. S. L. Center. *Brine Shrimp Life Cycle*. Retrieved July 12, 2019. 2014 (cit. on p. 75).

[110] J. Gulbrandsen. "Artemia Swarming Mechanisms and Suggested Reasonings". In: *J. Plankton Res.* 23 (7 2001), pp. 659–669 (cit. on pp. 76–78, 80, 83).

[111] J. Gulbrandsen. "Effects of the spatial distributions of light on prey ingestions on Atlantic halibut larvae (Hippolossus hippoglossus L.)" In: *J. Fish Biol.* 48 (1996), pp. 478–483 (cit. on pp. 76, 77, 80).

[112] M. Hiroki and Y Koshida. "Nauplian eye and its role in the phototactic behavior or Artemia salina". In: *Zool. Mag.* 85 (1976), pp. 78–83 (cit. on p. 76).

[113] A. A. Ali, L. Fortuna, M. Frasca, M. Rashid, and M. Xibilia. "Complexity in a population of Artemia". In: *Chaos, Solitons & Fractals* 44 (4 2011), pp. 306–316 (cit. on p. 78).

[114] M. Rashid, M. Frasca, A. Ali, R. Ali, L. Fortuna, and M. Xibilia. "Artemia swarm dynamics and path tracking". In: *Nonlinear Dynamics* 69 (4 2012), pp. 2237–2243 (cit. on pp. 78, 79).

[115] G. Van Stappen. "Introduction, biology and ecology of Artemia". In: *Manual on the production and use of live food for aquaculture*. Ed. by P. Lavens and P. Sorgeloos. Vol. 361. FAO Fisheries Technical Paper. FAO, 1996, pp. 79–106. ISBN: 9789251039342 (cit. on p. 80).

[116] A. Koch and H. Meinhardt. "Biological pattern formation: from basic mechanisms to complex structures". In: *Rev Mod Phys* 66.4 (1994), p. 1481 (cit. on p. 94).

[117] S. Kondo and T. Miura. "Reaction-diffusion model as a framework for understanding biological pattern formation". In: *Science* 329.5999 (2010), pp. 1616–1620 (cit. on p. 94).

[118] A. Deutsch and S. Dormann. *Mathematical Modeling of Biological Pattern Formation*. Springer, 2005 (cit. on p. 94).

[119] V. S. Zykov and A. T. Winfree. *Simulation of wave processes in excitable media*. John Wiley & Sons, Inc., 1992 (cit. on p. 94).

[120] J. M. Greenberg and S. Hastings. “Spatial patterns for discrete models of diffusion in excitable media”. In: *SIAM J Appl Math* 34.3 (1978), pp. 515–523 (cit. on p. 94).

[121] A. V. Holden, M. Markus, and H. G. Othmer. *Nonlinear wave processes in excitable media*. Vol. 244. Springer, 2013 (cit. on p. 94).

[122] A. L. Hodgkin and A. F. Huxley. “A quantitative description of membrane current and its application to conduction and excitation in nerve”. In: *J Physiol* 117.4 (1952), pp. 500–544 (cit. on p. 94).

[123] S. N. Flaim, W. R. Giles, and A. D. McCulloch. “Contributions of sustained I Na and I Kv43 to transmural heterogeneity of early repolarization and arrhythmogenesis in canine left ventricular myocytes”. In: *Am J Physiol-Heart C* 291.6 (2006), H2617–H2629 (cit. on p. 94).

[124] Y. Sekerci and S. Petrovskii. “Pattern Formation in a Model Oxygen-Plankton System”. In: *Computation* 6.4 (2018), p. 59 (cit. on p. 94).

[125] M. Courtemanche and A. T. Winfree. “Re-entrant rotating waves in a Beeler–Reuter based model of two-dimensional cardiac electrical activity”. In: *Int J Bifurcat Chaos* 1.02 (1991), pp. 431–444 (cit. on p. 94).

[126] D. F. Richards, J. N. Glosli, E. W. Draeger, A. A. Mirin, B. Chan, J.-l. Fattebert, W. D. Krauss, T. Oppelstrup, C. J. Butler, J. A. Gunnels, et al. “Towards real-time simulation of cardiac electrophysiology in a human heart at high resolution”. In: *Comput Method Biomec* 16.7 (2013), pp. 802–805 (cit. on p. 94).

[127] M. Hoffman, N. LaVigne, S. Scorse, F. Fenton, and E. Cherry. “Reconstructing three-dimensional reentrant cardiac electrical wave dynamics using data assimilation”. In: *Chaos* 26.1 (2016), p. 013107 (cit. on p. 94).

[128] G. E. Moore. “Cramming More Components Onto Integrated Circuits”. In: *PIEEE* 86.1 (1998), pp. 82–85 (cit. on p. 94).

[129] M. Dowle, R. Martin Mantel, and D. Barkley. “Fast simulations of waves in three-dimensional excitable media”. In: *Int J Bifurcat Chaos* 7.11 (1997), pp. 2529–2545 (cit. on p. 94).

[130] F. H. Fenton, E. M. Cherry, H. M. Hastings, and S. J. Evans. “Real-time computer simulations of excitable media: JAVA as a scientific language and as a wrapper for C and FORTRAN programs”. In: *Biosystems* 64.1-3 (2002), pp. 73–96 (cit. on pp. 94, 114, 115).

[131] E. Bartocci, R. Singh, F. B. von Stein, A. Amedome, A. J. J. Caceres, J. Castillo, E. Closser, G. Deards, A. Goltsev, R. S. Ines, et al. "Teaching cardiac electrophysiology modeling to undergraduate students: laboratory exercises and GPU programming for the study of arrhythmias and spiral wave dynamics". In: *Adv Physiol Educ* 35.4 (2011), pp. 427–437 (cit. on p. 94).

[132] A. Kaboudian, E. Cherry, and F. Fenton. "Real-time interactive simulations of large-scale systems on personal computers and cell phones: Toward patient-specific heart modeling and other applications". In: *Science Advances* (revision-submitted) (cit. on p. 94).

[133] R. S. Oliveira, B. M. Rocha, R. M. Amorim, F. O. Campos, W. Meira, E. M. Toledo, and R. W. dos Santos. "Comparing CUDA, OpenCL and OpenGL implementations of the cardiac monodomain equations". In: *International Conference on Parallel Processing and Applied Mathematics*. Springer. 2011, pp. 111–120 (cit. on p. 94).

[134] S. Augarten. *State of the Art*. 1981. Chap. The Most Widely Used Computer on a Chip: The TMS 1000. ISBN: 0-89919-195-9 (cit. on p. 94).

[135] D. K. Fisher and P. J. Gould. "Open-source hardware is a low-cost alternative for scientific instrumentation and research". In: *Modern Instrumentation* 1.02 (2012), p. 8 (cit. on p. 95).

[136] E. Koutroulis, K. Kalaitzakis, and N. C. Voulgaris. "Development of a microcontroller-based, photovoltaic maximum power point tracking control system". In: *IEEE Transactions on Power Electronics* 16.1 (2001), pp. 46–54 (cit. on p. 95).

[137] J. D. Serna and A. Joshi. "Visualizing the logistic map with a microcontroller". In: *Physics Education* 47.6 (2012), p. 736 (cit. on p. 95).

[138] F. Mahmud, N. Shiozawa, M. Makikawa, and T. Nomura. "Reentrant excitation in an analog-digital hybrid circuit model of cardiac tissue". In: *Chaos* 21.2 (2011), p. 023121 (cit. on p. 95).

[139] C.-h. Luo and Y. Rudy. "A model of the ventricular cardiac action potential. Depolarization, repolarization, and their interaction." In: *Circ Res* 68.6 (1991), pp. 1501–1526 (cit. on p. 95).

[140] Y. Isler, M. Kuntalp, and G. Gonel. "Microcontroller based Hodgkin-Huxley model neuron simulation". In: *2009 14th National Biomedical Engineering Meeting*. 2009, pp. 1–4 (cit. on p. 95).

[141] S. Yaghini Bonabi, H. Asgharian, S. Safari, and M. Nili Ahmadabadi. "FPGA implementation of a biological neural network based on the Hodgkin-Huxley neuron model". In: *Frontiers in neuroscience* 8 (2014), p. 379 (cit. on p. 95).

[142] M. Lu, J.-L. Wang, J. Wen, and X.-W. Dong. "Implementation of Hodgkin-Huxley neuron model in FPGAs". In: *2016 Asia-Pacific International Symposium on Electromagnetic Compatibility (APEMC)*. Vol. 1. IEEE. 2016, pp. 1115–1117 (cit. on p. 95).

[143] Š. Kubínová and J. Šlégr. "Physics demonstrations with the Arduino board". In: *Physics Education* 50.4 (2015), p. 472 (cit. on p. 95).

[144] C. Galeriu, S. Edwards, and G. Esper. "An Arduino investigation of simple harmonic motion". In: *The Physics Teacher* 52.3 (2014), pp. 157–159 (cit. on p. 95).

[145] W.-H. Kuan, C.-H. Tseng, S. Chen, and C.-C. Wong. "Development of a computer-assisted instrumentation curriculum for physics students: Using LabVIEW and Arduino platform". In: *Journal of Science Education and Technology* 25.3 (2016), pp. 427–438 (cit. on p. 95).

[146] A. Soriano, L. Marn, M. Valls, A. Valera, and P. Albertos. "Low Cost Platform for Automatic Control Education Based on Open Hardware." In: *IFAC Proceedings Volumes* 47.3 (2014). 19th IFAC World Congress, pp. 9044 –9050 (cit. on p. 95).

[147] B. Land. *ECE5760: Advanced Microcontroller Design and System-on-Chip*. 2019 (cit. on p. 95).

[148] F. Fenton and A. Karma. "Vortex dynamics in three-dimensional continuous myocardium with fiber rotation: Filament instability and fibrillation". In: *Chaos* 8.1 (1998), pp. 20–47 (cit. on pp. 96, 113, 114).

[149] A. Pikovsky, M. Rosenblum, J. Kurths, and J. Kurths. *Synchronization: a universal concept in nonlinear sciences*. Vol. 12. Cambridge university press, 2003 (cit. on p. 96).

[150] Y. C. Ji, I. Uzelac, N. Otani, S. Luther, R. F. Gilmour Jr, E. M. Cherry, and F. H. Fenton. "Synchronization as a mechanism for low-energy anti-fibrillation pacing". In: *Heart Rhythm* 14.8 (2017), pp. 1254–1262 (cit. on p. 96).

[151] R. E. Mirollo and S. H. Strogatz. "Synchronization of pulse-coupled biological oscillators". In: *SIAM J Appl Math* 50.6 (1990), pp. 1645–1662 (cit. on p. 96).

[152] H. Araki, J. Ehlers, K. Hepp, H. A. Weidenmller, and W. Beiglbck, eds. *International Symposium on Mathematical Problems in Theoretical Physics*. Vol. 39. Lecture Notes in Physics. Berlin, Heidelberg: Springer Berlin Heidelberg, 1975. ISBN: 978-3-540-07174-7 978-3-540-37509-8 (cit. on p. 96).

[153] L. G. Dominguez, R. A. Wennberg, W. Gaetz, D. Cheyne, O. C. Snead, and J. L. P. Velazquez. "Enhanced synchrony in epileptiform activity? Local versus distant phase synchronization in generalized seizures". In: *J Neurosci* 25.35 (2005), pp. 8077–8084 (cit. on p. 96).

[154] S. Heath. *Embedded Systems Design*. Newnes, 2003, pp. 11–12 (cit. on p. 96).

[155] ladyada. *Adafruit 3.5" 320x480 Color TFT Touchscreen Breakout Overview*. `https://learn.adafruit.com/adafruit-3-5-color-320x480-tft-touchscreen-breakout/`. 2019-01-15. 2014 (cit. on p. 99).

[156] A. L. Lin, A. Hagberg, E. Meron, and H. L. Swinney. "Resonance tongues and patterns in periodically forced reaction-diffusion systems". In: *Phys Rev E* 69.6 (2004), p. 066217 (cit. on p. 101).

[157] K. Aihara, T Takabe, and M Toyoda. "Chaotic neural networks". In: *Phys Lett A* 144.6-7 (1990), pp. 333–340 (cit. on p. 101).

[158] B. Y. Kogan, W. J. Karplus, B. S. Billett, A. T. Pang, H. S. Karagueuzian, and S. S. Khan. "The simplified FitzHugh-Nagumo model with action potential duration restitution: effects on 2D wave propagation". In: *Physica D* 50.3 (1991), pp. 327–340 (cit. on p. 101).

[159] G. Klaasen and W. Troy. "The Stability of Traveling Wave Front Solutions of a Reaction-Diffusion System". In: *SIAM J Appl Math* 41.1 (1981), pp. 145–167 (cit. on p. 104).

[160] C. K.R. T. Jones. "Stability of the travelling wave solution of the FitzHugh-Nagumo system". In: *T Am Math Soc* 286.2 (1984), pp. 431–469 (cit. on p. 104).

[161] J. G. Alford and G. Auchmuty. "Rotating wave solutions of the FitzHugh-Nagumo equations". In: *J Math Bio* 53.5 (2006), pp. 797–819 (cit. on p. 104).

[162] E. M. Cherry and F. H. Fenton. "Visualization of spiral and scroll waves in simulated and experimental cardiac tissue". In: *New J Phys* 10.12 (2008), p. 125016 (cit. on pp. 105, 113).

[163] E. N. Cytrynbaum and T. J. Lewis. “A global bifurcation and the appearance of a one-dimensional spiral wave in excitable media”. In: *SIAM J Appl Dyn Syst* 8.1 (2009), pp. 348–370 (cit. on p. 105).

[164] ladyada. *Photocells*. `https://learn.adafruit.com/photocells/overview`. 2019-01-15. 2012 (cit. on p. 106).

[165] A. J. Welsh, E. F. Greco, and F. H. Fenton. “Dynamics of a human spiral wave”. In: *Phys Today* 70.2 (2017), p. 78 (cit. on pp. 109, 110).

[166] I. R. Epstein and J. A. Pojman. *An introduction to nonlinear chemical dynamics: oscillations, waves, patterns, and chaos*. Oxford University Press, 1998 (cit. on p. 112).

[167] D. S. Rosenbaum, L. E. Jackson, J. M. Smith, H. Garan, J. N. Ruskin, and R. J. Cohen. “Electrical alternans and vulnerability to ventricular arrhythmias”. In: *New Engl J Med* 330.4 (1994), pp. 235–241 (cit. on p. 114).

[168] A. Gizzi, E. Cherry, R. F. Gilmour Jr, S. Luther, S. Filippi, and F. H. Fenton. “Effects of pacing site and stimulation history on alternans dynamics and the development of complex spatiotemporal patterns in cardiac tissue”. In: *Front Physiol* 4 (2013), p. 71 (cit. on p. 114).

[169] M. Minkkinen, M. Kähönen, J. Viik, K. Nikus, T. Lehtimäki, R. Lehtinen, T. Kööbi, V. Turjanmaa, W. Kaiser, R. L. Verrier, et al. “Enhanced predictive power of quantitative TWA during routine exercise testing in the Finnish Cardiovascular Study”. In: *J Cardiovasc Electr* 20.4 (2009), pp. 408–415 (cit. on p. 114).

[170] F. H. Fenton, E. M. Cherry, and L. Glass. “Cardiac arrhythmia”. In: *Scholarpedia* 3.7 (2008), p. 1665 (cit. on pp. 114, 115).

[171] S. Filippi, A. Gizzi, C. Cherubini, S. Luther, and F. H. Fenton. “Mechanistic insights into hypothermic ventricular fibrillation: the role of temperature and tissue size”. In: *Europace* 16.3 (2014), pp. 424–434 (cit. on p. 115).

[172] F. H. Fenton, E. M. Cherry, H. M. Hastings, and S. J. Evans. “Multiple mechanisms of spiral wave breakup in a model of cardiac electrical activity”. In: *Chaos* 12.3 (2002), pp. 852–892 (cit. on p. 115).

[173] Y. Kuramoto. “Self-entrainment of a population of coupled non-linear oscillators”. In: *International symposium on mathematical problems in theoretical physics*. Springer. 1975, pp. 420–422 (cit. on p. 115).

[174] J. A. Acebrón, L. L. Bonilla, C. J. Pérez Vicente, F. Ritort, and R. Spigler. "The Kuramoto model: A simple paradigm for synchronization phenomena". In: *Rev Mod Phys* 77 (2005), pp. 137–185 (cit. on pp. 115, 118).

[175] Y. Kuromoto. *Chemical Oscillations, Waves, and Turbulence*. Springer, 1984 (cit. on p. 115).

[176] K. Wiesenfeld, P. Colet, and S. H. Strogatz. "Frequency locking in Josephson arrays: Connection with the Kuramoto model". In: *Phys Rev E* 57.2 (1998), pp. 1563–1569 (cit. on p. 115).

[177] S. N. Dorogovtsev, A. V. Goltsev, and J. F. F. Mendes. "Critical phenomena in complex networks". In: *Rev Mod Phys* 80 (4 2008), pp. 1275–1335 (cit. on p. 115).

[178] A. Arenas, A. Daz-Guilera, J. Kurths, Y. Moreno, and C. Zhou. "Synchronization in complex networks". In: *Phys Reports* 469.3 (2008), pp. 93 –153 (cit. on p. 115).

[179] F. Drfler and F. Bullo. "Synchronization in complex networks of phase oscillators: A survey". In: *Automatica* 50.6 (2014), pp. 1539 –1564 (cit. on p. 115).

[180] S. Ameli, F. Shahbazi, M. Karimian, and T. Malakoutikhah. "The effects of noise and time delay on the synchronization of the Kuramoto model in small-world networks". In: *arXiv e-prints*, arXiv:1705.07875 (2017), arXiv:1705.07875. arXiv: `1705.07875 [cond-mat.dis-nn]` (cit. on p. 115).

[181] S. H. Strogatz. "From Kuramoto to Crawford: exploring the onset of synchronization in populations of coupled oscillators". In: *Physica D* 143.1 (2000), pp. 1 –20 (cit. on p. 118).

[182] D. A. Wiley, S. H. Strogatz, and M. Girvan. "The size of the sync basin". In: *Chaos* 16.1 (2006), p. 015103 (cit. on pp. 123, 135).

[183] T. Kotwal, X. Jiang, and D. M. Abrams. "Connecting the Kuramoto Model and the Chimera State". In: *Phys Rev Lett* 119 (26 2017), p. 264101 (cit. on p. 123).

[184] Y. Kuramoto. *Chemical Oscillators, Waves, and Turbulence*. 1984 (cit. on p. 133).

[185] S. H. Strogatz. "From Kuramoto to Crawford: exploring the onset of synchronization in populations of coupled oscillators". In: *Physica D Nonlinear Phenomena* 143 (2000), pp. 1–20 (cit. on p. 134).